A THERMO-ELASTO-HYDRODYNAMIC (TEHD) COMPUTATIONAL ANALYSIS FOR THE FORCE PERFORMANCE OF SELF-EQUALIZING TILTING PAD THRUST BEARINGS

A Dissertation

by

RASOOL KOOSHA

Submitted to the Office of Graduate and Professional Studies of
Texas A&M University
in partial fulfillment of the requirements for the degree of

DOCTOR OF PHILOSOPHY

Chair of Committee,	Luis San Andrés
Committee Members,	Adolfo Delgado-Marquez
	Hadi Nasrabadi
	Michael B. Pate
Head of Department,	Andreas A. Polycarpou

December 2020

Major Subject: Mechanical Engineering

ABSTRACT

A self-equalizing tilting pad thrust bearing (TPTB) improves operation reliability by adjusting its pads to accommodate thrust collar tilt, and hence removing a source of frequent wearing. Although recent literature states the need, predictive models for self-equalizing TPTBs are not available due to the complexity of their geometry. To date published analyses limit to a few highly simplified analytical models. The dissertation builds a thermo-elasto-hydrodynamic (TEHD) analysis tool and couples with a model for the pads leveling mechanism to deliver load performance predictions for self-equalizing TPTBs.

The dissertation presents predictions for an example self-equalizing TPTB with 124 mm in outer diameter (OD) operating with thrust collar static misalignment. Compared to a regular (non-equalizing) TPTB, a self-equalizing TPTB operates with up to 50% larger minimum film thickness and a roughly 1/2 of peak elastic deformation. Friction forces acting at the contact points of the leveling plates show a significant effect on the performance of the pad leveling system as they reduce the film clearance and increase a pad peak pressure. Predictions show a significantly large peak pressure at the contact points of the leveling plates ($>$0.9 GPa) when the bearings operate under a 3 MPa/pad specific load. The present work thus shows the importance of performing a comprehensive multiple-pad analysis to accurately evaluate the performance of self-equalizing TPTBs hence assuring their safe operation.

This dissertation further implements a flow starvation model into the TEHD compu-

tational analysis tool to deliver load performance predictions for TPTB operating with reduced flow rate. The work builds a model for the groove flow thermal mixing that determines the temperature of the lubricant entering a thrust pad for bearings operating with either reduced or over-flooded flow conditions. Under a starved flow condition, the analysis iteratively reduces the pad effective arc length until matching the available flow.

For an example TPTB with OD= 267 mm, a supply flow rate above the nominal rate increases the bearing drag torque but has little effect on the pad peak temperature rise or the pad minimum film thickness. A reduced flow, below the nominal rate, produces areas denuded of oil at both the pad leading edge and trailing edge, and thus the pad minimum film thickness substantially decreases while the film peak pressure largely increases. At 4 krpm and under a heavy load of 3 MPa/pad, the pad subsurface temperature rise almost doubles with a 30% nominal flow and exceeds the Babbitt critical temperature = 130°C. Also, compared to a flooded flow bearing, a starved flow bearing shows a larger axial stiffness coefficient but a much lesser axial damping coefficient.

In sum, the dissertation advances the state-of-the-art by pioneering a computational analysis model for self-equalizing TPTBs and starved flow TPTBs and produces unique knowledge on their load performance characteristics.

(Note: this dissertation is organized based on the author's previous publications and annual reports for Turbomachinery Research Consortium (TRC) during his PhD study; and the format follows American Society of Mechanical Engineers (ASME) journal publications format).

DEDICATION

To my parents,

Morteza Koosha and Ashraf Mirzaian

ACKNOWLEDGMENTS

I wholeheartedly express my gratitude to Dr. Luis San Andrés for giving me the opportunity to work at the Turbomachinery Laboratory. His extensive knowledge and meticulous attention to details along with his supervision, guidance, and teaching have been invaluable during my time as his student and research assistant. A lesson among many was "working hard does not cut it, one works smart" and upon which I will rely throughout my career.

Further, I would like to thank Dr. Brian Murphy, for his guidance and support throughout the preparation and release of XL_ThrustBearing® software tool.

Thanks to my committee members, Dr. Adolfo Delgado, Dr. Hadi Nasrabadi, and Dr. Michael B. Pate, for their guidance and support throughout the course of this research.

Thanks also go to my friends and colleagues and the department faculty and staff for making my time at Texas A&M University a great experience. Particularly, my lab mates at the Turbomachinery Laboratory, Xueliang Lu, Jing Yang, Bonjing Koo, Behzad Abdollahi, Wonbae Jung, Tingcheng Wu, Bryan Rodriguez, Scott Tran, Jonathan Toner, Rachel Bolen, and many more.

Special thanks to Turbomachinery Laboratory (TL) and Turbomachinery Research Consortium (TRC) for their interest and financial support throughout the years.

Last but most importantly, I would like to express my deepest gratitude to the love of my life, Aban, for her unrelenting support.

CONTRIBUTORS AND FUNDING SOURCES

Contributors

This work was supported by a dissertation committee consisting of Dr. Luis San Andrés, Dr. Adolfo Delgad, and Dr. Michael Pate of the Department of Mechanical Engineering and Dr. Hadi Nasrabadi of the Department of Petroleum Engineering.

All work conducted for the dissertation was completed by the student independently.

Funding Sources

Funding from Texas A&M University Turbomachinery Laboratory and Texas A&M University Turbomachinery Research Consortium (TRC) supported the graduate student to conduct the research presented in this dissertation.

TABLE OF CONTENTS

LIST OF FIGURES

FIGURE Page

LIST OF TABLES

1 INTRODUCTION[1]

Rotating machinery using tilting pad thrust bearings (TPTBs) to limit rotor axial displacement benefit from low drag power loss, a simple installation, and low-cost maintenance. Figure 1 depicts a schematic view of a TPTB (the fluid film thickness and pad tilts are exaggerated for clarity), consisting of a bearing housing, a thrust collar attached to the rotating shaft, and a series of pads supported on pivots. The ports in the bearing housing supply cold lubricant into the bearing pads, meanwhile hot lubricant leaves the bearing through its sides. In the grooves between pads, the cold supply of lubricant mixes with the upstream pad hot flow and enters the leading edge of the downstream pad at a temperature above the supply condition. As the thrust collar rotates, it draws fluid into the wedge (between a pad and the thrust collar) to generate a hydrodynamic pressure field supporting the applied load. The sheared fluid film produces a mechanical power loss that converts to thermal energy and raises the lubricant temperature. The load capacity of a hydrodynamic fluid film bearing largely depends on the lubricant viscosity, a function of its temperature [4].

Theoretical and experimental studies [5, 6] on thrust bearings (TBs) report a substantial increase in both peak pressure and temperature rise due to thrust collar misalignment. Published failure analyses [7, 8] further recognize misalignment as a primary cause of collapse in TBs. A self-equalizing TPTB is an improved bearing design that self-adjusts

[1]Reprinted with permission from material published by the author and advisor in Refs.[2, 3]

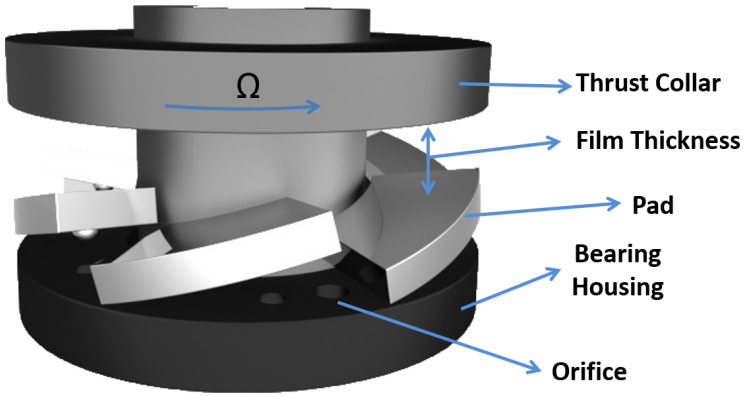

Fig. 1: Schematic view of a tilting pad thrust bearing (film thickness and pad tilts exaggerated). Reprinted with permission from [2].

the pads' position to follow thrust collar misalignment, hence evenly distribute the load among the pads [2]. Figure 1 shows (a) a photograph of a self-equalizing bearing and (b) a partial schematic view of a pad leveling mechanism including a series of levers called leveling plates. Bearing pads are supported on the upper plates which themselves are carried on the shoulders of two lower plates, free to tilt and to displace axially, as the lower plates placed on the bearing housing freely tilt. Compared to regular TPTBs, self-equalizing TPTBs offer a higher load capacity and are less costly to install as they reduce alignment constraints [9]. Due to such advantages, self-equalizing bearings are a preferred choice in many heavy-duty rotating machinery applications. In particular, the American Petroleum Institute (API) requires the use of self-equalizing TPTBs in turbines (gas and steam) and centrifugal pumps, as stated in Ref. [9].

However, several experimental works including Refs. [10, 11] report uneven load distribution in STPTBs. The friction forces acting at the contact points of the leveling

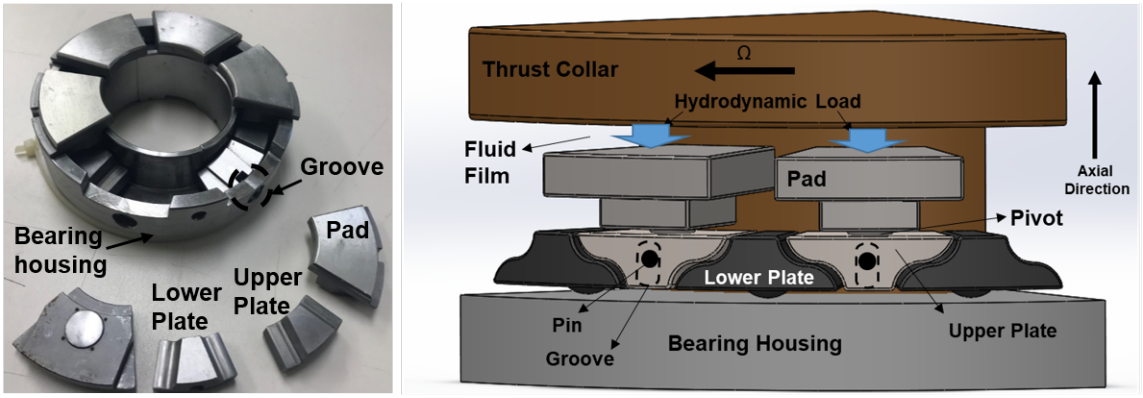

Fig. 2: (a) Photograph of a self-equalizing TPTB, and (b) a partial schematic view of a pad leveling system. Reprinted with permission from [3].

plates further limit the equalizing system and cause an unbalance loading. In addition, the tilting of leveling plates relocates the contact point between the upper plates and the lower plates and leads to a balance of moment in a lower plate with unequal loads on its sides. This is despite the fact that almost all predictive models assume equally distributed load in self-equalizing TPTBs and only conduct analysis for one pad [12–14]. Hence, a comprehensive multiple-pad TEHD analysis tool for self-equalizing TPTBs is due to deliver accurate predictions by accounting for friction forces acting between the leveling plates.

Furthermore, lubricant circulation is a major cost during the operation life and maintenance of fluid film bearings. An ancillary oil supply system (sump, pumps, filters and piping) must provide adequate flow and pressure into a bearing, whereas an oil evacuation system returns the hot oil for deaeration, cooling and storage in a sump. Industrial practice

often reduces the required flow to fully wet the bearing film lands in a planned effort to reduce drag power losses and operation costs, and to extend the life of the lubricant while reducing oil churning losses. The practice, if not properly assessed, can lead to excessive temperature rises of the lubricant and pad surfaces, overly thin film thickness, and the risk of lubricant varnishing and coking with failure of the Babbitted pad surfaces (San Andrés et al. [15] and Gregory [16]).

The major question is how low a supplied lubricant flow can be to warrant safe and reliable operation while ensuring the integrity of the mechanical components and demonstrating a sizable reduction in drag power loss. In an effort to extend the current analysis to account for the supply flow rate as an input variable, a model for operation under either a flow starvation or an over-flooded conditions helps better evaluate a TPTB performance toward reducing both the drag power loss and the oil flow consumption.

2 REVIEW OF PAST WORK[2]

2.1 BACKGROUND

In 1907, Anthony Michell (as Ref.[17] states) built the first tilting pad thrust bearing (TPTB) installed in a centrifugal pump on the Murray River in Australia. The TPTB carried a load of 13 kN at 200 rpm. Five years later, a power company in Pennsylvania (USA), concerned with the recurrent problems in their original roller bearings, signed a contract with Albert Kingsbury to build the first hydrodynamic thrust bearing in USA [18]. Kingsbury built a fixed geometry thrust bearing for a hydroelectric power-station on the Susquehanna River to hold a load of 250 kN at 94 rpm. The still-operating Kingsbury thrust bearing proved very effective at the time and drew significant attention. Soon after, by the beginning of World War I in 1914, thrust bearings became exceedingly popular in the navy, mainly to position vessels drive-train shaft.

In the 1930s, a marine vessel successfully traveled a long journey from England, around the tip of Africa, to Egypt where an offset thrust bearing on its drive-train was found installed in a wrong (reverse) direction; an event that the classical lubrication theory predicts improbable [19]. This, added to other shortcomings[3] of the classical theory of lubrication, created a demand for further theoretical and experimental investigations. Since then, the analysis of fluid film bearings has expanded significantly to account for thermal

[2]Reprinted with permission from material published by the author in Refs.[2, 3]

[3]e.g. in 1946 Fogg's [20] observed that parallel surface thrust bearings could support a load. This phenomena, known as "Fogg's Paradox", cannot be explained by classical theory of lubrication.

effects, elastic deformations of bearing elements, turbulent flow effects, oil cavitation, etc.

The following review scrutinizes the literature on (a) the load performance analysis of TPTBs, (b) self-equalizing TPTBs, and (c) flow starvation in TPTBs. This section reviews the literature published in the last four decades (1986-2020).

2.2 Load Performance Analyses of Tilting Pad Thrust Bearing

In 1986, Jeng et al. [21–23] build a thermo-hydrodynamic (THD) computational analysis tool for TPTBs that considers a general Reynolds equation with cross-film viscosity variations and couples to a thermal energy transport equation for the fluid film. An adiabatic heat flow condition is set on the thrust collar surface, and a one dimensional (1D) heat conduction equation models the heat transfer across a pad thickness. The authors present predictions for a turbulent flow TPTB with a large outer diameter (OD) equal to 2.8 m, operating at a rotor speed of 3 krpm (maximum surface speed of ΩR_o[4]= 440 m/s), and with a film thickness 60 μm at the pad pivot location. The analysis also accounts for turbulent flow effects using Ng's linearized model of turbulent flow [24]. Jeng et al.[22] also assume pad surface spherical crowning and note that pad elastic deformations could cause fluid film cavitation near a pad trailing edge, hence substantially reducing the bearing load capacity.

In 1999, Almqvist et al. [25] develop a more comprehensive THD analysis for lami-

[4]The maximum surface speed of a thrust bearing = ΩR_o with Ω as the rotor speed [rad/s] and R_o as the outer radius [m].

nar flow TPTBs to include thermal analysis in pads and the thrust collar. They also adopt a conventional thermal mixing model for pad inlet flow. Solution of a thermal transport equation in the fluid film, coupled to a three-dimensional (3D) heat transfer equation in pads and an axisymmetric heat transfer equation in thrust collar, delivers a 3D temperature distribution and further leads to a cross-film viscosity variation. The authors compare predictions and measured data for a six-pad laminar flow TPTB with 228 mm in diameter, operating with a rotor speed between 1.2 krpm and 2.5 krpm ($\Omega R_o = 14 - 30$ m/s) and under a specific load[5] per pad ranging from 0.5 MPa to 2.0 MPa. Predictions differ from test data by up to 20% for pressure, up to 10% for thrust collar temperature, and up to 10% for power loss. Almqvist et al. [25] conclude that proper assessment of empirical parameters including hot oil carry-over fraction and heat transfer coefficients are prerequisites for accurate predictions.

Glavatskih et al. (2002) [26] use a thermal energy transport equation to determine the temperature of the flow entering a pad inlet for operations with flooded lubrication methods. Opposed to the conventional hot oil carry-over model [11], the proposed model does not rely on empirical parameters and has the advantage of accounting for the supply flow rate. The analysis assumes any extra supply flow, i.e., exceeding the one theoretically needed, displaces to the OD of the bearing to mix with the flow exiting the upstream pad at its OD, and eventually returns to the sump. A pad inlet flow temperature follows by balancing the heat (internal energy) going into a groove oil bath from the supply flow and

[5]Unit load or specific load = W_z/A_P, where W_z is the axial load on a pad [N] and A_P is its area [m^2].

the heat from the upstream pad, at both its trailing edge and ID. Heat leaves the groove as is carried by the side leakage flow into the bearing OD and by the flow entering the leading edge of the downstream pad. The authors compare characteristic load performance measurements against predictions for a six-pad TPTB with 228 m in OD operating at a rotor speed up to 3 krpm (ΩR_o = 36 m/s) and under up to 2 MPa specific load per pad. Predictions match measurements with a maximum difference of 6 °C in pad temperature, 1 kW ($\approx$ 20%) in drag power loss, and 8 μm ($\approx$ 10%) in fluid film thickness.

In 1996, Brockett et al. [27] develop a thermo-elasto-hydrodynamic (TEHD) model for laminar flow fixed geometry thrust bearings. A Finite Element (FE) model produces a three dimensional (3D) elastic deformation field of the bearing pads, both mechanically and thermally induced, and an axisymmetric deformation field in the thrust collar, only mechanically induced. Predictions follows for a six-pad TB with 0.305 m in OD, operating at a rotor speed of 2 krpm (ΩR_o=32 m/s), and under a specific load between 1.32 MPa/pad and 10.5 MPa/pad. Comparing predictions obtained with and without accounting for elastic deformations in a pad shows the pad mechanical deformation is small, approximately 8% of the minimum film thickness (h_{min}), and leads to a maximum temperature rise of 2°C. On the other hand, the pad thermal deformation is relatively large, 45% of h_{min}, and causes a maximum temperature rise up to 24°C. Power loss and flow rate are moderately affected (at most %8) by both deformation modes. Predictions of the TEHD analysis are not compared against experimental data.

Two years later, Glavatskih and Fillon [28] extend their earlier THD model, in Ref. [25], to account for both pressure and temperature induced elastic deformations of pads in a laminar flow TPTB. Predictions are compared against test data for a six-pad TPTB with 228 mm in OD operating at rotor speeds up to 3 krpm (ΩR_o=36 m/s), and under a specific load up to 2.0 MPa. TEHD predicted pad temperatures better match test results, up to 15% closer than those delivered by a THD analysis.

Glavatskih and Filon [12] (2004) further account for the effects of pad face coating as a liner on the static load analysis of TPTBs. They adopt a simple formula from Ref.[29] for mechanically induced axial deformations of a liner layer and present predictions for the static load performance of a soft-polymer liner TPTB with 228 mm in OD operating at a rotor speed up to 3 krpm (ΩR_o=36 m/s) and under a specific load up to 2.0 MPa/pad. The thickness and thermal isolation properties of a liner material strongly affect the bearing performance. As the liner thickness increases, the pad temperature remarkably lessens, the film temperature slightly drops at the pad leading edge but significantly raises at the pad trailing edge, and the fluid film thickness decreases, in particular at the pad leading edge. Unlike a babbitted pad, the authors observe that the soft-polymer liner largely deforms around the pad center (peak pressure zone) and produces a caved in surface. Recall that a soft-polymer material is substantially more flexible than a babbitt up to 500 times. In another study, Ettles et al.[30] (2003) also report a caved in surface near the pad trailing edge of a soft-liner TPTB. A caved in pad top surface reshapes the hydrodynamic wedge

to cause a lower operating film thickness.

In 2008, Wasilczuk and Rotta [31] perform computational fluid dynamic (CFD) analysis to model the fluid mixing phenomena in the grooves between pads in laminar flow TBs. A 3D CFD model extends earlier analysis (2D model of Rotta 2004 [32]) to account for a radial component of velocity induced by centrifugal forces acting on the fluid in a groove. An adiabatic condition is imposed for metal-fluid interfaces (pad sides and thrust collar surface) and a constant temperature is imposed for the other sides (including the bottom of a groove). Analysis of a large eight-pad fixed-geometry TB with 1.78 m in OD, operating at 214 rpm (ΩR_o=20 m/s) and under 6 MN load (specific load =3.05 MPa/pad), is compared for two lubrication supply methods: traditional bath lubrication vs relatively new direct oil supply. A direct oil supply system leads to slight reductions in the film inlet temperature (3°C) and in the pad maximum temperature (5°C). With a flooded lubrication method, the analysis shows significant oil churning in the bearing grooves. However, induced by the centrifugal forces due to the thrust collar rotation, the radial component of the flow velocity is always outward in a groove, i.e. the oil only displaces from the ID toward the OD. The finding confirms the observation in prior work [33] that the oil pushed toward the bearing OD cannot reach into a downstream grooves or the next pad leading edge.

In 2010, Ahmed et al. [34] use a TEHD analysis tool to study the impact of the elastic deformations of pads and the thrust collar on the performance of a fixed-geometry TB. The

model accounts for pad deformations due to both pressure and temperature changes and pressure induced thrust collar deformations. Predictions for an eight-pad thrust bearing with 200 mm in OD, operating with a rotor speed of 2.6 krpm (ΩR_o=27.2 m/s) and under a specific load of 1.4 MPa/pad, shows that pad mechanical deformations do not exceed 5 μm and have a very limited influence on the fluid film thickness. On the other hand, the pressure induced deformations in the thrust collar increases to 45 μm and significantly influence the film thickness. Predictions delivered by the TEHD model largely differ from THD predictions as the applied load increases (>0.9 MPa). The maximum difference is 8% for pressure (0.4 MPa), 40% for film thickness (15 μm), and 20% for fluid film temperature rise (6°C).

2.3 Self-Equalizing Tilting Pad Thrust Bearings

Although self-equalizing TPTBs have been commercially available for over three decades, published experimental or theoretical work on their performance are limited. Glavatskih [10] in 2000 performs experiments to quantify the transient thermal response of self-equalizing TPTBs to a sudden change in the operation condition. The author measures pad subsurface temperatures, the pressure field and drag power loss on a six-pad bearing with 228 mm in OD undergoing a sudden change in either speed, applied load, or supply flow rate. The bearing operates under a specific load up to 2.0 MPa/pad and at a rotor speed up to 3 krpm (ΩR_o = 36 m/s). The recorded pad subsurface temperatures are more sensitive to changes in shaft speed and supply flow rate rather than to variations in load.

For example, the bearing drag power loss undergoes a sharp change immediately after a change in operating condition to then showing a gradual change as the bearing operating temperature varies. Most importantly, the measurements show a redistribution of the pressure field following a rapid change in the applied load to then produce uneven loading among the pads despite the use of a pad leveling system.

In 2006, Glavatskih and Fillon [35] build a TEHD computational analysis tool to account for both pressure and temperature induced elastic deformations of pads in a TPTB. The authors compare predictions obtained with and without accounting for pad elastic deformations against test data for a six-pad self-equalizing bearing with 228 mm in OD operating under a specific load up to 2.0 MPa, and at rotor speeds up to 3 krpm (maximum surface speed ΩR_o = 36 m/s). Predictions obtained accounting for pad elastic deformations better match experimental results, up to 15% closer than THD predictions. The authors also report a measured uneven load distribution across the bearing pads despite having a pad leveling system [36].

In 2014, Wodtke et al. [14] compare measured fluid film thickness, fluid film pressure, and pad temperature for a large size 5.2 m OD sixteen-pad self-equalizing TPTB against predictions obtained from two distinct predictive tools. The laminar flow bearing operates at a rotor speed of 92 rpm (ΩR_o = 24.5 m/s) and under an applied load of 27.7 MN, i.e. specific load = 2.6 MPa on a pad. The first predictive tool is a 3D TEHD analysis developed by Souchet [37] which imposes a thermal boundary condition at the pad free

surfaces using an empirical heat transfer coefficient. Using Souchet analysis, the entire fluid surrounding a pad has a uniform temperature. The second tool is a fluid-structure interface (FSI), adopting a thermo-elasto-hydrodynamic (TEHD) analysis developed by Pajkaczkowski [38] and coupling a finite element model (FEM) of the bearing elements with a computational fluid dynamics (CFD) model of the fluid (in the film and around the pads). Both predictive tools conduct a single pad analysis, i.e., an equal load acting on all pads.

Predictions from Souchet analysis [37] closely match the measured film thickness while predictions from fluid-structure interaction (FSI) analysis [38] show a substantial discrepancy. The predicted film pressure from the FSI analysis, however, better matches the experimental results, up to 10% closer than that delivered by Souchet's analysis. Nonetheless, predicted pad subsurface temperatures from both analysis tools differ substantially from the measurements. In particular, temperatures delivered by Souchet's analysis show up to a 70% difference with measured pad temperatures. Despite the use of an equalizing mechanism, based on the experimental results, the authors report an uneven load distribution acting on the bearing pads.

In 2017, Bavassono et al. [11] improve the load capacity of a self-equalizing TPTB used in a high power-density gas turbine application as detailed below. A preliminary experimental investigation reveals uneven loads across the bearing pads despite the use of an equalizing system. The measured mean pressure in some pads is roughly twice that

on other pads. The authors develop a simple analytical model for the maximum aligning capability of the equalizing system as a function of the number of pads in the bearing and the physical limit on the leveling plates' tilting. The analytical model predicts that reducing the number of pads from ten to eight improves the pad leveling system performance. Accordingly, Bavassono et al. [11] implement the following changes to improve bearing load performance. Both the radial length and the arc length of a pad increase to reduce the number of the pads and also to maximize the bearing surface area. The Babbitt (white metal) layer is replaced by an Aluminum-Tin (Al-Sn) based material to withhold a higher pressure and to ensure temperature durability. The pad backing portion made of Copper-Chromium (Cu-Cr) material, instead of the original steel material, to increase heat flow conduction through pads. The authors state that the new design load capacity is 1.45 times that of the original bearing.

Most recently in 2019, Gokaltun and Decamillo [1] assemble a finite element (FE) model of an example six-pad self-equalizing TPTB with 267 mm in OD and predict the load performance of the pad leveling system. The FE model extends over the thrust collar, pads and pivots, leveling plates and bearing housing. For simplicity, the analysis excludes the fluid film and instead the thrust collar directly pushes against the bearing pads with an equivalent pressure. Despite the use of the levels, peak pressures among the pads vary widely; and the balancing system loses its effectiveness as the applied load decreases.

2.4 Analyses for Flow Starvation

Bielec and Leopard (1969) [33] measure temperature rise below a pad surface in an eight-pad steel-Babbitted TPTB with 124 mm in OD, 68 mm in ID. The bearing operates under a specific load ranging from 1 MPa to 6 MPa per pad and at a rotor speed between 2 krpm and 12 krpm (ΩR_o = 13 m/s to 78 m/s). At 8 krpm and under 4.2 MPa/pad specific load, the measured pad peak subsurface temperature rise constantly increases from 70 °C to 90 °C as the supply flow rate decreases from over 100 liter per minute (LPM) to less than 10 LPM. The exit oil temperature rise also increases from 3 °C to 40 °C. The authors further evaluate a flooded lubrication system with the supply flow inlet at the bearing ID vs one with the inlet at the OD. With the supply flow inlet at the ID, the oil well distributes into the bearing grooves to fully lubricate the bearing pads. However, with the supply flow at the bearing OD, oil had to move against a centrifugal effect, induced by collar rotation, to reach the bearing pads. Therefore, the majority of the oil wetted the OD area until exiting the bearing while some inner ID areas on the pads remained denuded of oil. This finding also reveals that with a flooded lubrication method, the flow exiting a pad at the ID may enter the inlet of the downstream pads whereas the flow exiting a pad at the OD is thrown away and returns to the sump.

In 1974, Gregory [16] experimentally investigates the effect of supply flow rate on the static load performance of TPTBs. The author measures pad temperatures and drag power loss in a double-sided eight-pad bearing with 0.267 m in OD operating at a rotor speed of

4-11 krpm (ΩR_o = 55 - 154 m/s) and under a specific load up to 2.8 MPa per pad. The lubricating condition includes three supply flow rates: the manufacturer recommended flow rate, 50% above than the recommended flow rate, and 50% lesser than the recommended rate. A double-sided TPTB consists of bearings facing opposite sides of a thrust collar; one bearing acts against a primary axial load in the system (active side), while the other one takes occasional reverse-direction loads (inactive or slack-side). Gregory observes that, a supply flow reduction below the recommended rate lessens the power loss up to 20%, while an increase is supply flow rate produces an increase in drag power loss by 30%. Nonetheless, the TPTB operating under a reduced flow condition shows a higher pad temperature raise, up to 15 °C higher than that in the operation with recommended rate. On the other hand, a flow rate above the recommended rate shows only a 5 °C reduction in pad temperature rise. The author confirms the TPTB operates safely and remains pristine when operating with ½ the recommended flow condition. Note Gregory [16] uses a thermal balance method between the inlet and outlet flows to estimate the bearing drag power loss. San Andrés et al [39] (among many others) show such thermal balance method underestimates the bearing power loss when operating with a reduced flow rate.

Two years later (1976), Capitao at al. [40] measure pad subsurface temperature rise and drag power loss in a double-sided TPTB while operating under both laminar flow and turbulent flow conditions and with a supply flow rate ranging from 50% to 150% of the recommended magnitude. The authors test two six-pad steel-babbitted bearings, one with

OD=267 mm and the other with OD=304 mm, operating under a specific load per pad ranging from 0.7 MPa to 2.8 MPa, and with the rotor turning at speeds between 4 krpm and 14 krpm (ΩR_o = 55-192 m/s for the smaller bearing, and ΩR_o = 63-218 m/s for the larger one). The measured pad temperature rise shows up to 16 °C increase as the supply flow rate falls to 50% of the recommended magnitude. Yet, increasing the supply flow rate to 150% of recommended rate leads to a slight drop (maximum of 5 °C) in the pad temperature rise. The bearing drag power loss substantially increases with shaft speed but shows minimal variations with the load applied on the bearing. More importantly, the measured drag power loss noticeably drops as the supply flow rate decreases, in particular on the high end of rotor speed ($\Omega \rightarrow$14 krpm). Note the work here also uses a thermal balance method to measure power loss.

In 1987, Artiles and Heshmat [41] theoretically study the effect of flow starvation on the static load performance of fixed geometry thrust bearings. Flow starvation is modeled by a reduction in the fluid film circumferential length, i.e. the film begins at an offset angle from the pad leading edge where the side leakage flow equals the bearing supply flow. The authors perform analysis for a fixed-geometry TB with ID/OD = 1/3, 1/2, and 2/3, pad arc length = 27°, 42°, and 57°, and an 80% taper extent, while operating with a supply flow ranging from 100% to just 10% of the nominal rate. The authors define the nominal rate as the minimum flow rate nominal to fully fill the gap between the bearing pads and the thrust collar. Predictions show bearing drag torque reduces by 90% when the supply

flow decreases below 25% of the required rate. The predicted pad temperature rise shows a constant increase as the supply flow rate decreases. The increase in pad temperature is substantially larger as the supply flow rate decreases below 40% of the nominal rate. Further, a reduction in supply flow rate below 70% of the nominal produces a significant reduction in the minimum film thickness.

DeCamillo (2014) [42] investigates experimentally the onset and persistency of axial subsynchronous vibrations (SSV) in TPTBs while also evaluating the effectiveness of commonly used solutions in industry. The test bearings are a centrally pivoted and a 60% offset pivoted six-pad supplied with a conventional flooded lubrication system, a 60% offset six-pad TPTB configured with a leading-edge-groove (LEG) lubrication system, and a 65% offset eight-pad bearing with a LEG lubrication system. All bearings have 267 mm in OD and 133 mm in ID with 35.4 cm^2 in total pad area. The measured axial vibration shows a substantial dependency on the supply flow rate for both fully flooded flow and starved flow operations. DeCamillo recommends adjusting (increasing or decreasing) the supply flow rate to push the system axial natural frequency out of the range of operating conditions. Reducing the pivot offset also proved effective in reducing the bearing axial stiffness to lower the amplitude of vibration. Most importantly, the implementation of an "O-Ring" damper proved a reliable option toward eliminating axial vibration.

In 2018, San Andrés et al. [15] present a simple flow model for the load performance of tilting pad journal bearings (TPJBs) operating with flow starvation. The work aims to

evaluate the onset of subsynchronous vibration (SSV) hash motions for TPJBs operating under flow starvation to describe unexpected low frequency shaft vibration reported in literature [43]. The starved flow condition is treated in a similar manner as in prior literature [41, 44, 45], i.e. with a reduction in the pads effective arc length. Regardless of the flow condition, the supplied flow to a bearing is distributed among the pads based on a hydraulic network analogy. The authors assume the pad flow resistance remains unchanged regardless of supply flow condition. Hence, the fraction of supplied flow into each pad, as derived from the solution for the flooded condition, remains unchanged during operation under a flow starvation condition.

San Andrés et al. [15] detail load performance predictions for two journal bearing configurations. The first configuration is a load between pads (LBP) four-pad TPJB with 0.127 m in diameter operating at 5 krpm rotor speed (ΩR_s =33 m/s) and under a specific load of 0.689 MPa. The second one is a (load on pads, LOP) five-pad TPJB with 0.423 m in diameter operating at 3.6 krpm rotor speed (ΩR_s = 80 m/s) and under 1.07 MPa of specific load. For both configurations, flow starvation reduces the bearing damping coefficient and which produces a higher amplitudes of frequency response functions (FRFs). Further, the LOP configuration demonstrates a relatively small stiffness and damping resistance against shaft displacements in the direction orthogonal to the load.

In 2019, Abdollahi and San Andrés [46] introduce a novel thermal and flow mixing model for feed grooves in TPJBs and aiming to rectify some limitations of a conventional

hot oil carry-over coefficient model [47]. The model initially estimates a supply flow distribution among the bearing feed grooves based on each groove demand for supply flow. Then, a groove efficiency coefficient represents the ability of a groove to discharge the hot upstream flow and heat out of the groove and which is used to determine the side leakage flow temperature. Unlike the (empirical) hot oil carry-over coefficient, the groove efficiency coefficient is not a function of the bearing operating condition and remains constant. The fluid inlet flow and temperature at the leading edge of each bearing pad follow from balances of flow and heat in a volume enclosing the feed groove and the sides of the trailing edge of the upstream pad and the leading edge of the downstream pad. The model includes for bearing configurations with evacuated ends (no end seals) and fully flooded (with end seals). Pad subsurface temperature rise predictions from the new model and the conventional hot oil carry-over model are compared against test data for a large TPTB with 500 mm in diameter and slenderness ratio L/D = 1. The bearing operates at 3 krpm rotor speed and under 2.5 MPa of specific load. Predictions from the new model are up to 17 °C closer to the measurements.

2.5 LITERATURE REVIEW CLOSURE

The literature review elaborates on the importance of accounting for thermal changes as well as the pad elastic deformations in the analysis of TPTBs. Accounting for cross-film thermal variations in the solution of both thermal energy transport equation and Reynolds equation proves to essential for accurate predictions [19]. Among the different approaches

used for pad elastic deformations, the analytical solutions [48, 49] are simple and fast albeit offering lesser accuracy than that from a computational physical (FE) models [35]. In addition, the FE analysis can be used for pads of physical complex geometry.

The literature review further reveals that thrust collar misalignment significantly affects the load performance of thrust bearings and which emphasizes the importance of using self-equalizing TPTBs to assure reliable operation. Incidentally, Refs. [1, 10, 11, 14, 35, 36, 50] report an uneven load distribution in thrust bearings despite the implementation of a self-equalizing system. Note that yet unaccounted for friction forces acting at the contact points of the leveling plates reduce their aligning ability. Nonetheless, almost all predictive models assume an identical load acting on each bearing pad, and thus only conduct a single pad analysis [13, 25, 35, 37, 38].

Lastly, the literature review shows that supply flow rate substantially affects both static and dynamic load performance of thrust bearings. Most of the published computational analysis of starved flow fluid film bearings are specific to journal bearings [15, 46] and the few work on starved flow thrust bearings are limited to the static performance of fixed-geometry bearings [41, 51].

3 A THERMO-ELASTO-HYDRODYNAMIC PREDICTIVE MODEL FOR TILTING PAD THRUST BEARINGS[6]

3.1 DESCRIPTION OF TEHD MODEL

Figure 3 depicts a schematic view of a TPTB geometry and variables. A global cylindrical coordinate system (r, θ, z) has its origin at the center of the bearing housing surface (O_B) with the z-axis normal to its surface. At any point on a pad surface, the film thickness $h_{(r,\theta,t)}$ is a function of the thrust collar axial location $(e_{c(t)})$, the pivot axial location $(e_{p(t)})$, thrust collar misalignment angles (φ, ψ), elastic deformation of the pad top surface $d_{(r,\theta,t)}$, and the pad tilt angles $(\alpha_{(t)}, \beta_{(t)})$ around the (γ, ζ) axes, respectively. On pad k^{th} with a pivot located at (R_P^k, θ_P^k), the film thickness is,

$$\begin{aligned} h^i_{(r,\theta,t)} =& [e_c - (e^i_P + t_P)] + (\varphi\, r)\sin\theta - (\psi\, r)\cos\theta \\ &+ (\alpha^i\, r)\sin(\theta^i_P - \theta) + (\beta^i\, r)\cos(\theta^i_P - \theta) - (\beta^i\, R^i_P) \end{aligned} \qquad \theta^k_l < \theta < \theta^k_t \qquad (1)$$

where t_P is the pad thickness and (θ_l and θ_t) are the circumferential location of the pad leading edge and trailing edge, respectively. If the thrust collar is perfectly aligned, then all pads develop an identical fluid film geometry and reaction force.

[6]Reprinted with permission from material published by the author and advisor in Refs.[2, 52]

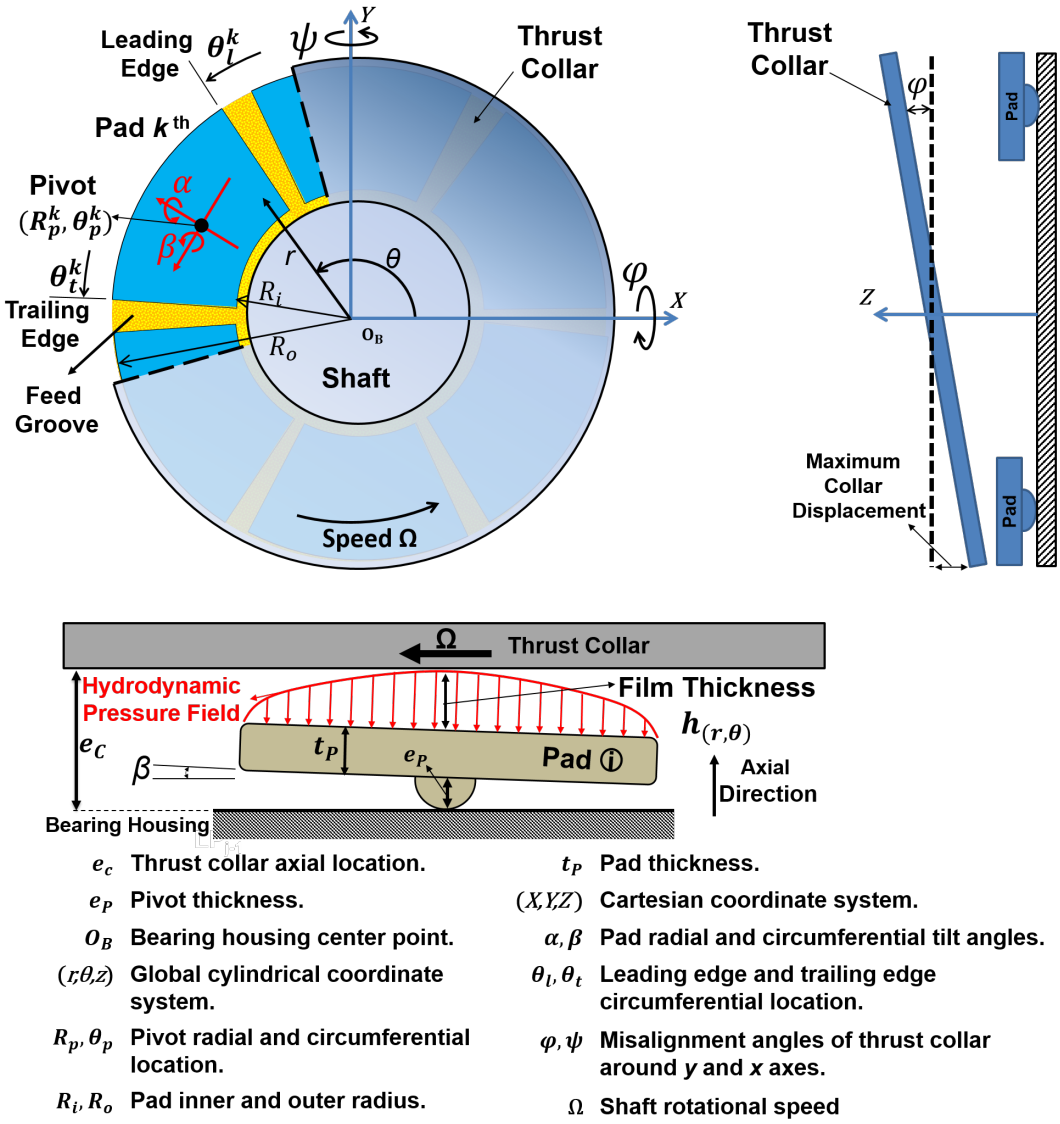

e_c	Thrust collar axial location.	t_P	Pad thickness.
e_P	Pivot thickness.	(X,Y,Z)	Cartesian coordinate system.
O_B	Bearing housing center point.	α, β	Pad radial and circumferential tilt angles.
(r,θ,z)	Global cylindrical coordinate system.	θ_l, θ_t	Leading edge and trailing edge circumferential location.
R_p, θ_p	Pivot radial and circumferential location.	φ, ψ	Misalignment angles of thrust collar around *y* and *x* axes.
R_i, R_o	Pad inner and outer radius.	Ω	Shaft rotational speed

Fig. 3: Geometry, coordinate systems, and definition of variable for a TPTB. Reprinted with permission from [2].

3.1.1 Reynolds Equation for a Thin Film

Jeng et al. [21] derive a Reynolds equation governing the generation of the hydrodynamic pressure field $P_{(r,\theta,t)}$ in a turbulent flow fluid film bearing. The fluid is Newtonian,

incompressible, and inertialess. This equation is [21]

$$\frac{1}{r}\frac{\partial}{\partial r}\left(rH_r\frac{\partial P}{\partial r}\right)+\frac{1}{r}\frac{\partial}{\partial \theta}\left(H_\theta\frac{1}{r}\frac{\partial P}{\partial \theta}\right)=\Omega\frac{\partial G}{\partial \theta}+\frac{\partial h}{\partial t} \tag{2}$$

where Ω is the rotor (thrust collar) speed, and (H_r, H_θ, and G) are turbulent flow functions. See Appendix A for a detailed description of the turbulent flow functions. In a laminar flow region and for a lubricant with a constant viscosity across the film, $H_r = H_\theta = \frac{h^3}{12\mu}$ and $G = \frac{h}{2}$, thus Eqn.(2) reduces to the familiar form,

$$\frac{1}{r}\frac{\partial}{\partial r}\left(r\frac{h^3}{12\mu}\frac{\partial P}{\partial r}\right)+\frac{1}{r}\frac{\partial}{\partial \theta}\left(\frac{h^3}{12\mu}\frac{1}{r}\frac{\partial P}{\partial \theta}\right)=\frac{\Omega}{2}\frac{\partial h}{\partial \theta}+\frac{\partial h}{\partial t} \tag{3}$$

3.1.2 Thermal Energy Transport Equation in a Fluid Film

The thermal energy transport equation balances the energy generated due to viscous shear dissipation in the fluid film and the energy advected by the fluid flow advection and heat conducted to the solids (pads and thrust collar). Figure 4 shows a schematic view of the energy transport mechanisms.

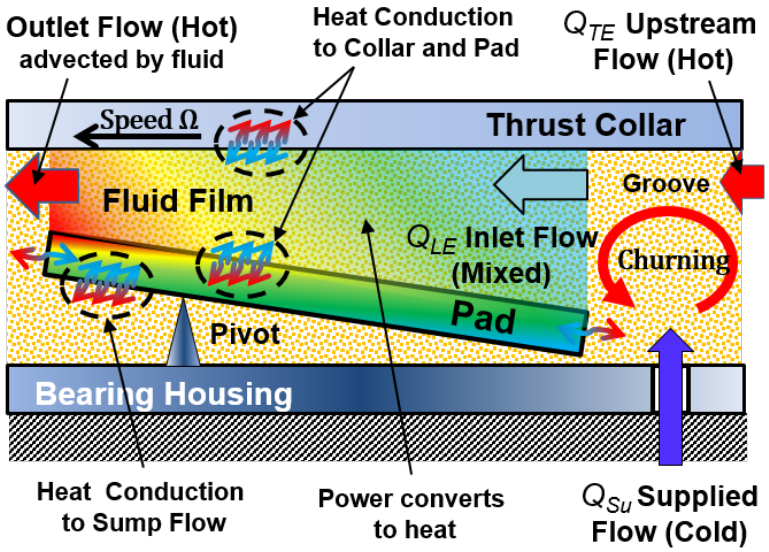

Fig. 4: Schematic view of flow thermal mixing in an oil feed groove region, heat advection by the fluid flow, and heat conduction to the bearing elements (pads and thrust collar). Reprinted with permission from [2].

At a steady state condition, Jeng et al. [21] state the thermal energy transport equation for an incompressible fluid at temperature $T_{(r,\theta,z)}$ is,

$$\left[V\frac{\partial T}{\partial r}+V\frac{\partial T}{r\partial\theta}+W\frac{\partial T}{\partial z}\right]=\kappa^{*}\left[\nabla^{2}T\right]+\Phi=$$
$$\kappa^{*}\left[\frac{1}{r}\frac{\partial}{\partial r}\left(r\frac{\partial T}{\partial r}\right)+\frac{1}{r^{2}}\frac{\partial T^{2}}{r\partial\theta^{2}}+\frac{\partial T^{2}}{\partial z^{2}}\right]+\mu^{*}\left[\left(\frac{\partial U}{\partial z}\right)^{2}+\left(\frac{\partial V}{\partial z}\right)^{2}\right] \quad (4)$$

where ρ and c_p are the lubricant density and specific heat, respectively. These parameters are assumed constant over the flow domain. U, V, and W are fluid velocity components along the radial, circumferential, and axial directions, respectively, induced by pressure

gradient and thrust collar rotation. Jeng et al. [21] state them as,

$$U_{(r,\theta,z)} = -\frac{\partial P}{\partial r}\left(\int_0^z \zeta_3(\bar{z})\, d\bar{z} - \frac{\int_0^h \zeta_3(z)\, dz}{\int_0^h \zeta_4(z)\, dz} \int_0^z \zeta_4(\bar{z})\, d\bar{z} \right) \tag{5a}$$

$$V_{(r,\theta,z)} = r\Omega\left(1 - \frac{\int_0^z \zeta_4(\bar{z})\, d\bar{z}}{\int_0^h \zeta_4(z)\, dz}\right) - \frac{\partial P}{r\partial\theta}\left(\int_0^z \zeta_1(\bar{z})\, d\bar{z} - \frac{\int_0^h \zeta_1(z)\, dz}{\int_0^h \zeta_2(z)\, dz} \int_0^z \zeta_2(\bar{z})\, d\bar{z} \right) \tag{5b}$$

$$W_{(r,\theta,z)} = -\int_0^z \frac{U}{r}\, d\bar{z} - \int_0^z \frac{\partial U}{\partial r}\, d\bar{z} - \int_0^z \frac{\partial V}{r\partial\theta}\, d\bar{z} \tag{5c}$$

Appendix A details the turbulent flow functions ζ_i , $i = 1 : 4$.

The analysis accounts for turbulent flow effects using Ng's linearized model of turbulent flow, not detailed here for brevity, see Refs.[21, 24]. The turbulent flow effective viscosity (μ^*) and the turbulent flow heat conductivity (κ^*) are [21],

$$\mu^*(r,\theta,z) = \mu\left(1 + \frac{\epsilon_m}{\upsilon}\right) \tag{6a}$$

$$\kappa^*(r,\theta,z) = \kappa\left(1 + Pr\frac{\epsilon_H}{\upsilon}\right) = \kappa\left(1 + \frac{Pr}{Pr^*}\frac{\epsilon_m}{\upsilon}\right) \tag{6b}$$

where ϵ_m and ϵ_H are the eddy viscosity for momentum transfer and the eddy viscosity for heat transfer, respectively. Pr is the Prandtl number, and $Pr^* = \frac{\epsilon_m}{\epsilon_H}$ is the turbulent flow Prandtl number with a typical value of 0.769 [19]. The lubricant material conductivity κ is constant over the flow domain, and the lubricant viscosity (μ) is a function of the local temperature (T),

$$\mu = \mu_{Su}\, e^{-\alpha_{VT}(T - T_{Su})} \tag{7}$$

where μ_{Su} and T_{Su} are the fluid viscosity and temperature at supply condition and α_{VT} is a fluid temperature-viscosity coefficient. Note for laminar flow, $\mu^* = \mu$ and $\kappa^* = \kappa$.

A characteristic circumferential Reynolds number, $Re = \frac{R_m \Omega \rho h_{min}}{\mu}$, determines either a laminar, superlaminar, or turbulent flow condition. Here R_m is the pad mean radius, h_{min} is the minimum fluid film thickness, Ω is the rotor speed, and ρ and μ are the fluid density and viscosity, both averaged across the flow domain, as per Refs.[53, 54]. The flow is laminar for operation at $Re < Re_L$=580, a lower critical Reynolds number, and transits to fully turbulent at $Re > Re_U$=800, an upper critical Reynolds number, as per Refs.[53, 54]. For $Re_L < Re < Re_U$, the flow, known as a superlaminar flow condition [40], is in a transition zone between laminar flow and turbulent flow.

At a feed groove, a simple thermal mixing flow model sets the inlet fluid temperature T^i_{LE} (at pad i^{th} leading edge), as a function of the demand for supply flow Q_{Su} at a cold temperature T^i_{Su}, and the upstream pad outlet flow rate Q^{i-1}_{TE} at temperature Q^{i-1}_{TE} (trailing edge). That is,

$$Q^i_{LE} = Q^i_{Su} + \lambda_{mix}\, Q^{i-1}_{TE} \tag{8a}$$

$$Q^i_{LE}\, T^i_{LE} = Q^i_{Su}\, T_{Su} + \lambda_{mix}\, Q^{i-1}_{TE}\, T^{i-1}_{TE} \tag{8b}$$

where λ_{mix} is a lubricant thermal mixing coefficient, an empirical parameter that depends on the lubrication feed method, and Q_{LE} is the pad leading edge flow rate. The fluid flow rates at the pad leading edge and trailing edge along with the flow side leakage at the pad

inner radius and outer radius are calculated by integrating the fluid film velocity field over those boundaries.

Through out this dissertation, the hot oil carry-over model is used to obtain predictions for operation with flooded flow conditions, i.e.Chapters 3 and 4. Later in Chapter 5, the analysis adopts a groove thermal model from Ref.[26] for operation with either a starved flow condition or an over-flooded flow condition.

3.1.3 The Heat Conduction Equation in a Pad

The steady-state heat conduction equation governing the flow of heat through a solid pad with isotropic conductivity is [25],

$$\nabla^2 T_P = \frac{1}{r}\frac{\partial}{\partial r}\left(r\frac{\partial T_P}{\partial r}\right) + \frac{1}{r^2}\frac{\partial T_P^2}{r\partial\theta^2} + \frac{\partial T_P^2}{\partial z^2} = 0 \tag{9}$$

where T_P is the temperature in a pad. At a pad top surface (facing the fluid film), the heat flow from the fluid film into the pad is modeled as,

$$q_{film\rightarrow pad} = -\kappa\frac{\partial T}{\partial z} = q_{into\ pad} = -\kappa_P\frac{\partial T_P}{\partial z} \tag{10}$$

where T and κ are the fluid film temperature and thermal conductivity coefficient, respectively, and κ_P is the conductivity coefficient of the pad top layer (liner). Accordingly, using a pad or liner with a low thermal conductivity (e.g. a polymer) reduces the heat conduction

into a pad; thus, the film temperature may increase and the lubricant viscosity would drop. At the back surface of a pad and on the side surfaces, the heat transfers into the lubricant surrounding the pad and is modeled using a heat transfer coefficient η [25],

$$q_{pad \rightarrow environment} = -\kappa_P \frac{\partial T_P}{\partial \vec{\mathbf{n}}} = -\eta (T_L - T_P) \tag{11}$$

where T_L is the surrounding temperature and $\vec{\mathbf{n}}$ is the surface normal vector.

3.1.4 Finite Element Model for Pad Elastic Deformations

As Figure 5 portrays, the hydrodynamic pressure acting on the pads top surface (obtained through the Reynolds Eqn.(2)) along with temperature gradient within the pad (obtained the Eqn.(9)) induce elastic deformations over the bearing pad that change the bearing operating fluid film geometry. The final shape of the deformed pad strongly depends on the pad support (pivot) type and geometry. Pivoted pads generally warp into a convex shape to open the fluid film at the pad edges [2]. Spring-supported pads, however, may deform into a concave shape to close the fluid film thickness at both the pad inner radius and outer radius.

The elastic deformation in a pad is governed by a force equilibrium equation, a strain-displacement equation, and the material constitutive law. Let $\boldsymbol{\sigma}$ represent the stress tensor in a cylindrical coordinates system; then a solid subject to body force $\mathbf{F}_B = \{F_r, F_\theta, F_z\}^T$ is

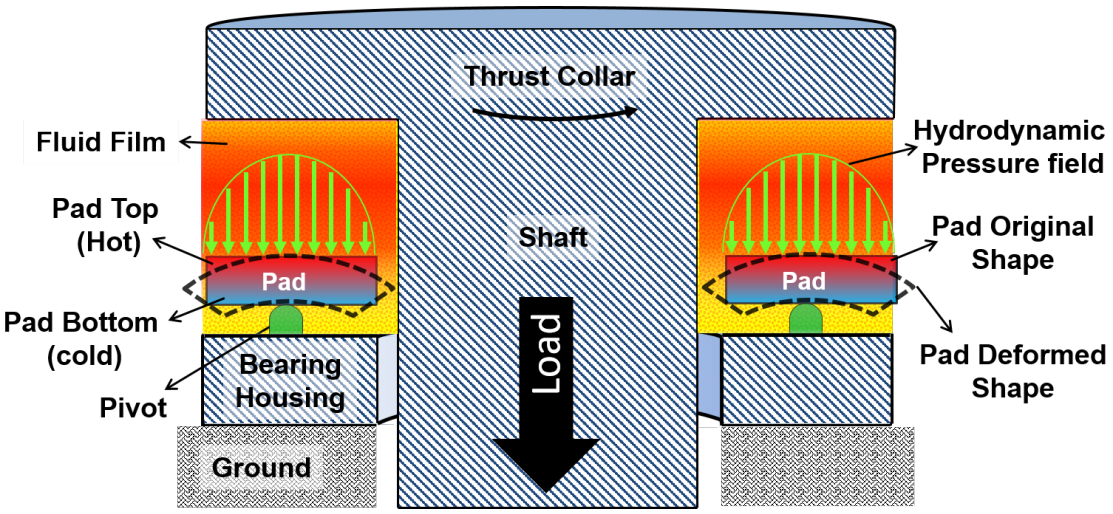

Fig. 5: Schematic view of bearing pads elastic deformations due to the combined actions of temperature gradient and hydrodynamic pressure. Pad temperature gradually decreases from the top surface (shown in red) toward the bottom surface (shown in blue).

in equilibrium [27] when,

$$\mathbf{D}_{\sigma}^{T}\boldsymbol{\sigma} + \mathbf{F}_{B} = 0 \tag{12}$$

where $\mathbf{D}_{\sigma}$ is the stress gradient operator for the cylindrical coordinate (r, θ, z). The thermoelastic law [28] correlates the stress components to any initial, thermal or mechanical strain tensors,

$$\varepsilon_{ij} = \frac{1+\nu}{E}\sigma_{ij} - (\frac{\nu}{E}\sigma_{kk} + \alpha_T \Delta T_P)\delta_{ij} \quad i, j, k = r, \theta, z \tag{13}$$

where ε_{ij} is the strain tensor and ΔT_P is the temperature variation relative to a reference temperature. δ_{ij} = zero for $i \neq j$ and unity for $i = j$. Parameters E, ν and α_T represent the elasticity modulus, Poisson ratio, and the thermal expansion coefficient, all properties of

the pad or liner material.

The strain tensor $\boldsymbol{\varepsilon}$ relates to the displacement vector $\mathbf{u}=[u_r, u_\theta, u_z]^T$ at each point by [27]

$$\boldsymbol{\varepsilon} = \mathbf{D}_u \mathbf{u} \tag{14}$$

with $\mathbf{D}_u$ as the displacement gradient operator (in the cylindrical coordinate system). The principle of virtual work combines the elasticity Eqns. (12-14) into a single equation, see Appendix B for description of the principle of virtual work. That equation is [19],

$$\begin{aligned} \iiint_V \delta\mathbf{u}^T \left[\mathbf{D}_u^T \, \mathbf{E} \, \mathbf{D}_u \mathbf{u} - \mathbf{D}_u^T \, \mathbf{E} \, \Delta T_P \boldsymbol{\alpha}_T - \mathbf{F}_B\right] dV \\ - \iint_S \delta\mathbf{u}^T \mathbf{P} \, dS = 0 \end{aligned} \tag{15}$$

where $\mathbf{P}$ is the pressure vector acting on a surface. Using shape functions (N_e, $e = 1, \ldots, N_{NE}$: number of nodes per element) associated with the FE model, Eqn.(15) becomes a linear system of algebraic equations on each element,

$$\mathbf{K}^e \, \mathbf{u} = \mathbf{f}_B^e + \mathbf{f}_P^e + \mathbf{f}_T^e, \qquad e = 1, \ldots, N_E \tag{16}$$

where $\mathbf{f}_B^e$ is the body force vector (gravity or magnetic), $\mathbf{f}_T^e$ is the force vector induced due to the temperature gradient, and $\mathbf{f}_P^e$ is induced due to the hydrodynamic pressure on a pad

top surface. The local stiffness matrix and load vectors for each element are,

$$\mathbf{K}^e = \iiint_{V^e} \mathbf{N}^T \mathbf{D}_u^T \, \mathbf{E} \, \mathbf{D}_u \mathbf{N} \, dV \tag{17a}$$

$$\mathbf{f}_B^e = \iiint_{V^e} \mathbf{N}^T \mathbf{F}_B \, dV \tag{17b}$$

$$\mathbf{f}_T^e = \iiint_{V^e} \mathbf{N}^T \mathbf{D}_u^T \, \mathbf{E} \, \mathbf{D}_u \, \mathbf{N} \, dV \tag{17c}$$

$$\mathbf{f}_P^e = \iint_{S^e} \mathbf{N}^T \mathbf{P} \, dS \tag{17d}$$

The local stiffness matrices and load vectors are assembled into a global stiffness matrix $\mathbf{K}^{\mathrm{G}} = \bigcup \mathbf{K}^{\mathrm{e}}$ and a global load vector $\mathbf{F}^{\mathrm{G}} = \bigcup (\mathbf{f}_B^e + \mathbf{f}_P^e + \mathbf{f}_T^e)$, respectively. After enforcing boundary conditions for the pivot, a Cholesky decomposition technique delivers for the global displacement vector $\mathbf{u}^{\mathrm{G}}$.

To predict bearing performance under a given certain load per pad (W_z/N_P), the analysis assumes an initial axial location (e_c) for the thrust collar and solves Reynolds Eqn.(2), the thermal energy transport Eqn.(4) in the fluid film, and the heat conduction Eqn.(9). The pressure field acting on a pad reacts with a load and also induces moments around the pivot point. Thus, iterations on the pad tilt angle take the pad into a position with null moment. Next, the FE elastic model, built with the pad and liner layer geometry and material properties, takes the pressure and temperature fields to produce a pad surface deformation field which changes the fluid film thickness and, therefore the pressure field. The analysis repeats until variations in the pressure, temperature and deformation fields satisfy a

convergence criteria, e.g. typically $<0.1\%$ of the peak magnitude.

The load W_z carried by a pad is calculated through integration of the pressure field over the pad surface. If the reaction load W_z does not equal the load applied on the pad, the thrust collar axial location is updated and the analysis starts over. The bearing drag power loss $\mathcal{P}$ follows from the shear force τ_w acting on the collar surface ($z = e_c$),

$$\begin{aligned} \mathcal{P} &= \sum_{i=1}^{N_P} \iint_{A_P^i} (r\,\Omega)\,\tau_{w(z=e_c)}\,dA \\ &= \sum_{i=1}^{N_P} \iint_{A_P^i} (r\,\Omega)\,\mu \left.\frac{\partial V}{\partial z}\right|_{z=e_c} dA \end{aligned} \tag{18}$$

where N_P is the number of pads.

At an equilibrium position, a small amplitude period force ($\Delta F^{i\omega t}$) with frequency ω excites a thrust collar displacement (Δe_C) and pad motions ($Deltae_P$, $\Delta\alpha$, $\delta\beta$) with identical frequency to produce perturbations in the fluid film thickness and pressure fields. Integration of the perturbed pressure fields over the i^{th} pad generates 16 (=4×4) fluid film complex stiffness coefficients [55],

$$Z_{XY}^i = K_{XY}^i + i\omega C_{XY}^i = \int_{R_i}^{R_o} \int_{\theta_{LE}}^{\theta_{TE}} P_X^i h_Y r\,d\theta\,dr, \quad X, Y = e_C, e_P, \alpha, \beta \tag{19}$$

where **K** and **C** are matrices of the film stiffness and damping coefficients, respectively,

and,

$$[h_{e_C} h_{e_P} h_\alpha h_\beta] = [1 - 1rsin(\theta_P - \theta)rcos(\theta_P - \theta)] \tag{20}$$

A frequency reduced model [55] assumes all pads move with the same frequency (ω) to reduce the 16×N_{Pad} stiffness coefficients into axial stiffness and damping coefficients (K_z, C_z).

3.2 Validation of TEHD Analysis

3.2.1 Validation of Finite Element Model for Pad Elastic Deformations

To verify the accuracy of the Finite Element (FE) model, pad elastic deformations from the in-house FE model are compared against those delivered by a commercial FE software package for two types of TPTBs. The first example is a 60% offset cylindrical pivot (1D tilting) TPTB from Guo et al.[56], and the second is a 50% offset spherical pivot (2D tilting) TPTB from Mikula [57]. Table 1 lists the geometry, lubricant properties, operating conditions, and thermal properties of the two example bearings.

Figure 6 shows 3D models of the test bearing pads in the commercial software with boundary conditions applied at the pivot location. The axial displacements of the pad pivot section are zero and the pivot center point is constrained to a null displacement in the radial and circumferential directions to avoid singularity of the pad stiffness matrix ($\mathbf{K}^{\mathrm{G}}$). Figures 7 and 8 depict elastic axial deformations (due to both pressure and temperature) of

Table 1: Geometry and operating condition for two TPTBs used for analysis validation. Reprinted with permission from [2].

Bearing properties	Cylindrical pivot[56]	Spherical pivot[57]
Number of pads, N_P	3	8
Inner diameter, ID	110 mm	133 mm
Outer diameter, OD	220 mm	267 mm
Pad arc length	45°	38°
Pivot circum. offset	60 %	50 %
Pivot radial offset	-	50 %
Pad thickness*, t_P	27 mm	25 mm
Babbitt thickness*	2 mm	2 mm
Pad area, A_P	35.6 cm^2	45.6 cm^2
Operating condition		
Specific load	1.0 MPa	1.0 MPa
Shaft rotational speed	3 krpm	3 krpm
Supply pressure*	0 bar	0 bar
Fluid properties		ISO VG32
Viscosity-temperature coefficient, α^*_{TV}		0.0247 1/°C
Viscosity, μ_{Su} (at 46°C)		22 cPoise
Density, ρ		821 kg/m^3
Specific heat capacity, c_P		2.17 kJ/(kg· °C)
Thermal conductivity, κ		0.13 W/(m· °C)
Pad material properties	Steel	Babbitt
Thermal conductivity, κ_P	51 W/(m·°C)	55 W/(m·°C)
Elasticity modulus, E	210 GPa	52 GPa
Thermal expansion, α_T	12 10^{-6}/°C	24 10^{-6}/°C
Poisson ratio, ν	0.3	0.3
Thermal properties		
FE reference temperature**		20 °C
Thermal mixing coefficient.* λ_{mix}		0.4-0.8
Heat Transfer coefficient on back of pad** η		100 W/(m^2·°C)

*Assumed or calculated based on the available data .
**Taken from Ref.[35]

the pad top surface as delivered by the (a) commercial software vs. those obtained by (b) the current model. The pad surface axial deformations obtained by the in-house FE model match those delivered by the commercial software with a maximum difference of 1.5%.

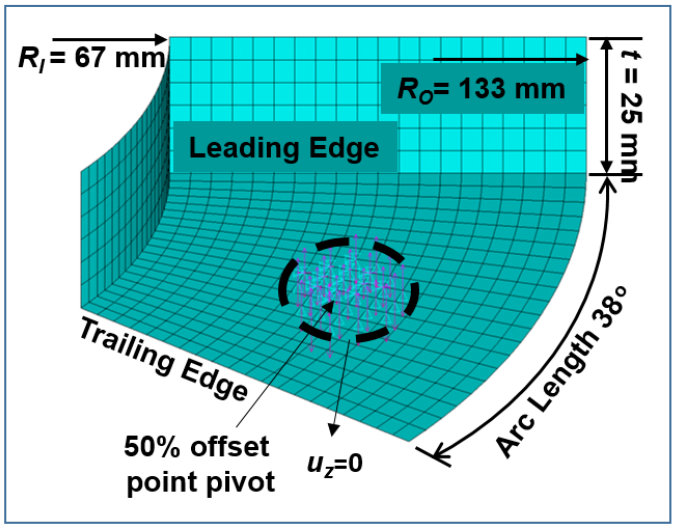

(b) Spherical Pivot Pad

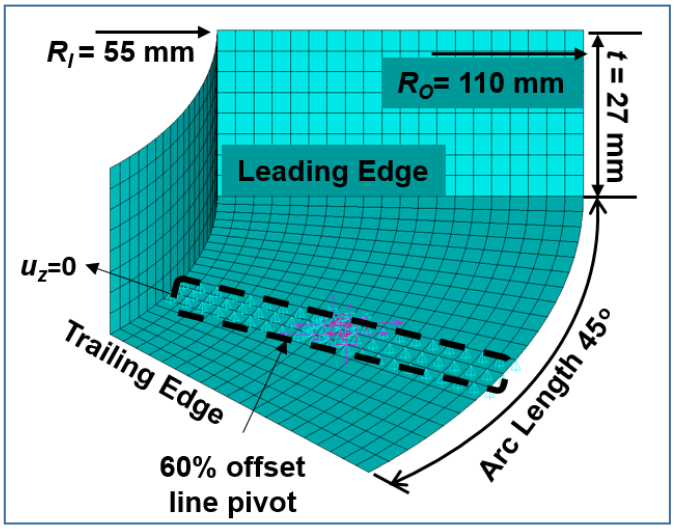

(b) Cylindrical Pivot Pad

Fig. 6: Pad model in commercial software for (a) a cylindrical pivot TPTB from Ref.[56], and (b) a spherical pivot TPTB from Ref.[57]. Reprinted with permission from [2].

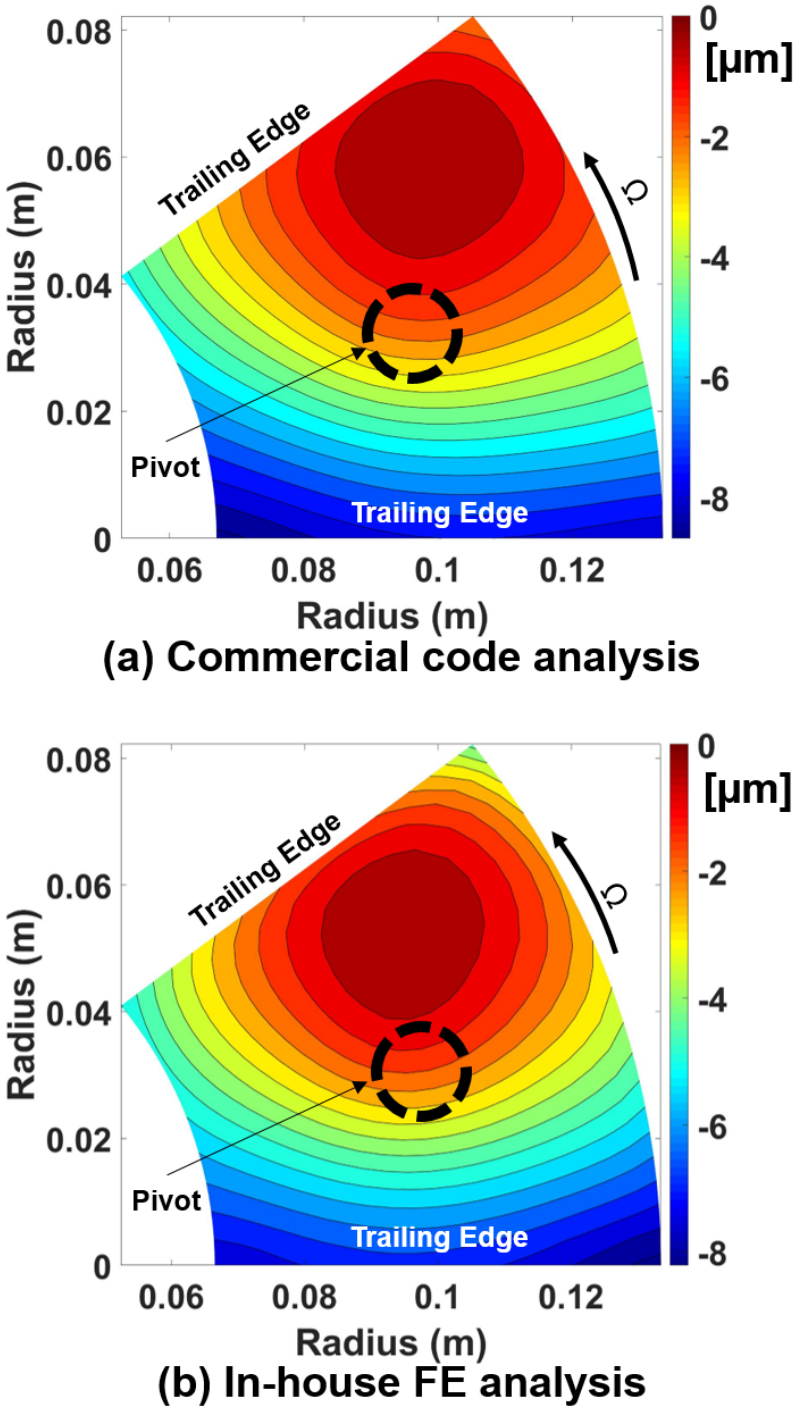

Fig. 7: Predictions of pad top surface elastic deformations for a spherical pivot TPTB from Ref.[57]. Comparison between (a) commercial software and (b) in-house FE model. Oil supply temperature = 46° , Rotor speed = 3 krpm and specific load = 1.0 MPa. Reprinted with permission from [2].

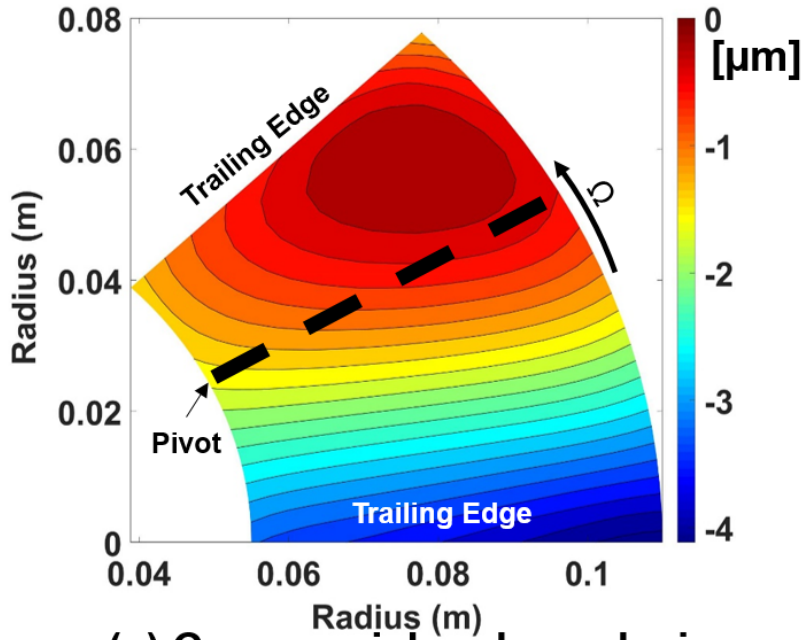

(a) Commercial code analysis

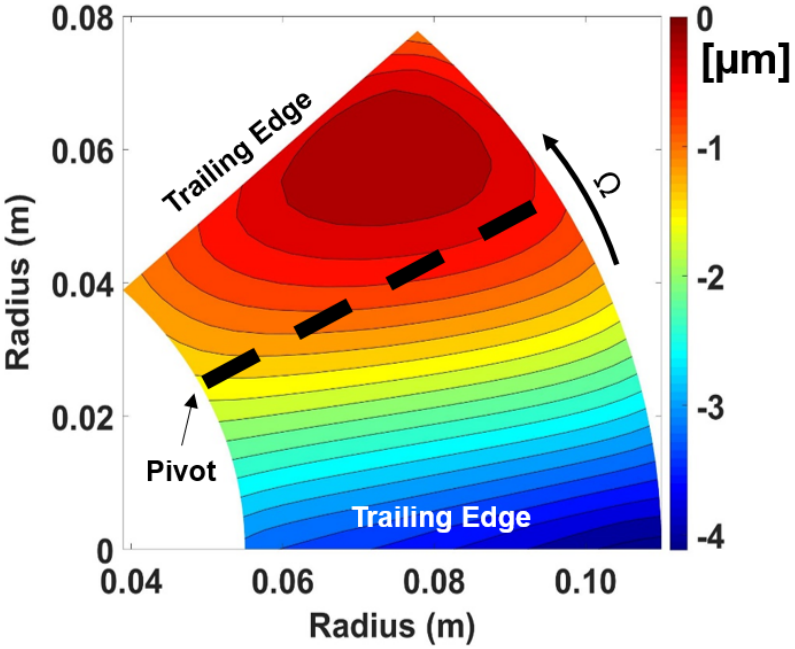

(b) In-house FE analysis

Fig. 8: Predictions of pad top surface elastic deformations for a cylindrical pivot TPTB from Ref.[56]. Comparison between (a) commercial software and (b) in-house FE model. Oil supply temperature = 46° , Rotor speed = 3 krpm and specific load = 1.0 MPa. Reprinted with permission from [2].

3.2.2 Validation of TEHD Predictions vs. Test Data for Laminar Flow TPTB

To further validate the thermo-elasto-hydrodynamic (TEHD) model, predictions are benchmarked vs. published test data in Refs. [25, 58] for a six-pad TPTB with 228 mm in OD, 114 mm in ID, and 50°in pad arc length. Table 2 highlights the bearing geometry, fluid properties, and operating conditions for test TPTB. The bearing pads are made of steel with a 1 mm thick Babbitt layer. The lubricant is an ISO VG46 oil at a supply temperature of 40°.

Two pressure transducers mounted on the thrust collar measure the oil film pressure at 25% and 75% of the pad radial length. Two eddy current proximity sensors, installed at the mean radius of a pad leading edge and trailing edge, measure the oil film thickness. A thermocouple placed at the 75% offset from the pad leading edge and inner radius, 3 mm below the Babbitt surface, measures the pad subsurface temperature. The bearing power loss is also obtained through direct measurement of the shear torque acting on the bearing housing. Table 3 list uncertainties associated to the measurements.

Figure 9 shows the TEHD predicted oil film pressure across the pad arc length at the 25% and 75% of the pad radial length vs. test data for the test TPTB operating under a specific load per pad ranging from 0.5 MPa to 2.0 MPa and with 3 krpm of rotor speed (ΩR_o = 36 m/s). The predicted pressure field correlates well with test data with a maximum of difference of 0.3 MPa (9% with respect to the measurements).

Table 2: Geometry, fluid properties, and operating condition for TPTB in Refs.[25, 58]

Bearing properties		
Number of pads, N_P		6
Inner diameter, ID		114 mm
Outer diameter, OD		228 mm
Pad arc length		50°
Pivot circum. offset		60 %
Pivot radial offset		50 %
Pad thickness*, t_P		28.1 mm
Babbitt thickness*		1 mm
Pad area, A_P		42.5 cm^2
Operating condition		
Specific load		0.5-2.0 MPa
Shaft rotational speed		1.5-3.0 krpm
Supply pressure*		0 bar
Fluid properties		ISO VG46
Viscosity-temperature coefficient, α^*_{TV}		0.0334 1/°C
Viscosity, μ_{Su} (at 40°C)		39 cPoise
Density, ρ		861 kg/m^3
Specific heat capacity, c_P		2.019 kJ/(kg· °C)
Thermal conductivity, , κ		0.13 W/(m· °C)
Pad material properties	Steel	Babbitt
Thermal conductivity, κ_P	51 W/(m·°C)	55 W/(m·°C)
Elasticity modulus, E	210 GPa	52 GPa
Thermal expansion, α_T	12 10^{-6}/°C	24 10^{-6}/°C
Poisson ratio, ν	0.3	0.3
Thermal properties		
FE reference temperature*		20 °C
Thermal mixing coefficient.* λ_{mix}		0.4-0.6
Heat Transfer coefficient on back of pad* η		100 W/(m^2·°C)

*Assumed or calculated based on the available data.

Table 3: Measurement uncertainty of test data in Refs.[25, 58].

Measurement	**Uncertainty**
Temperature, [°C]	±1
Oil film pressure, [MPa]	±4%
Oil film thickness, [μm]	±1.5
Power loss, [kW]	±1.0

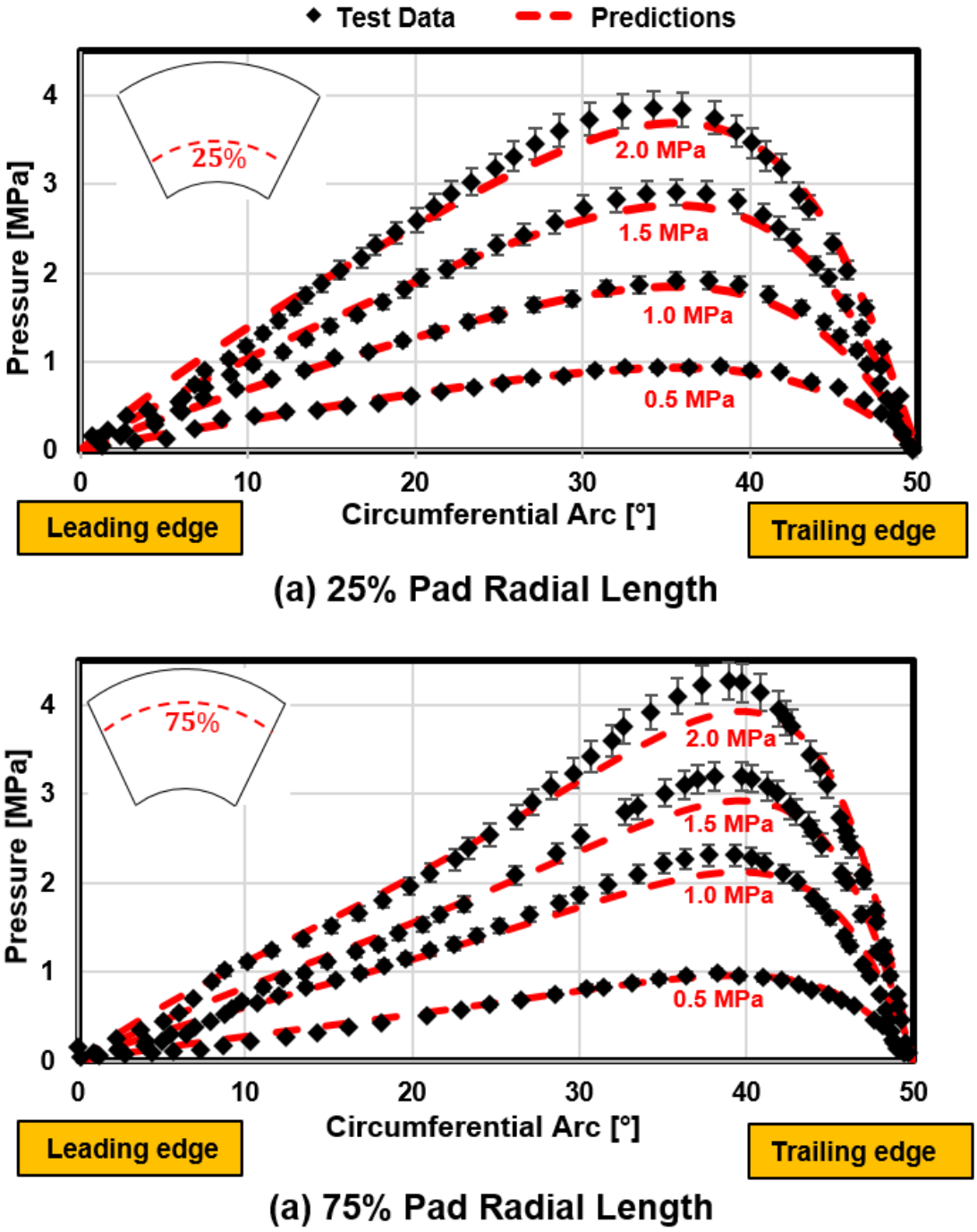

Fig. 9: TEHD predicted and measured [58] oil film pressure along circumferential length of a pad at the 25% (top) and 75% (bottom) of the radial length for a six-pad TPTB operating under 0.5, 1.0, 1.5, and 2.0 MPa of specific load per pad. Oil supply temperature = 40°, Rotor speed = 3 krpm.

Figure 10 depicts test data from Ref.[58] and the predicted fluid film thickness at the mean radius of the pad leading edge on the top graph, and the pad trailing edge on the bottom graph vs. rotor speed and vs. specific load. On the right side graph, results are benchmarked vs. rotor speed ranging from 1.5 krpm to 3 krpm (ΩR_o = 18-36 m/s), while the left side graph shows the results vs. specific load ranging from 0.5 MPa to 2 MPa per pad. The oil supply temperature is 40°C. Predictions match the test data with a maximum difference of 10 μm at the pad leading edge and 6 μm at the pad trailing edge. Note the said differences present 10% and 8% of the respective measured magnitude.

Figure 11 shows TEHD predictions of (a) pad subsurface temperature rise and (b) bearing drag power loss vs. test data. The current model predictions follow the test data with a difference no more than 5°C for pad subsurface temperature and 0.6 kW for bearing power loss. These differences represent 17% and 7% of the measured magnitudes, respectively.

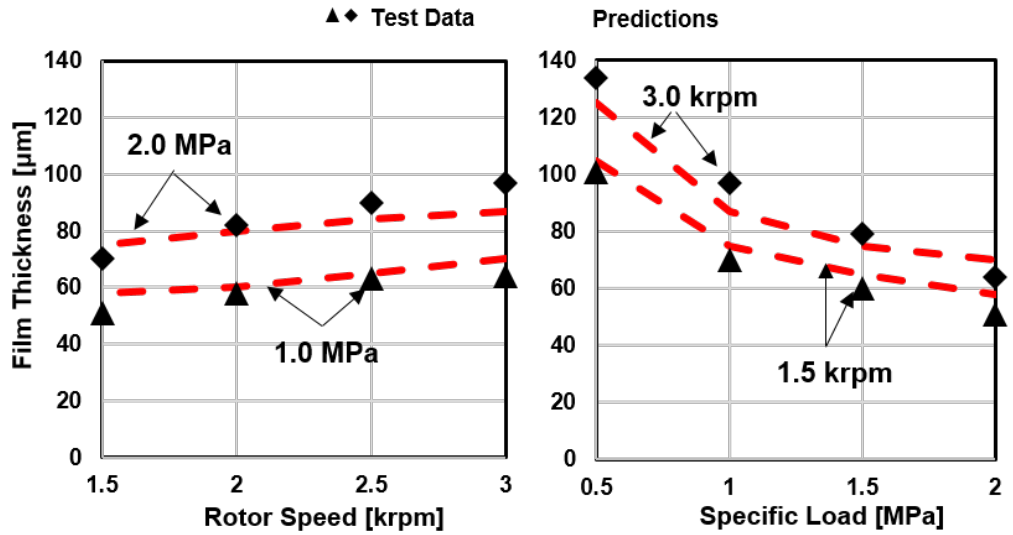

(a) Pad Leading Edge Film Thickness vs. speed and vs. load

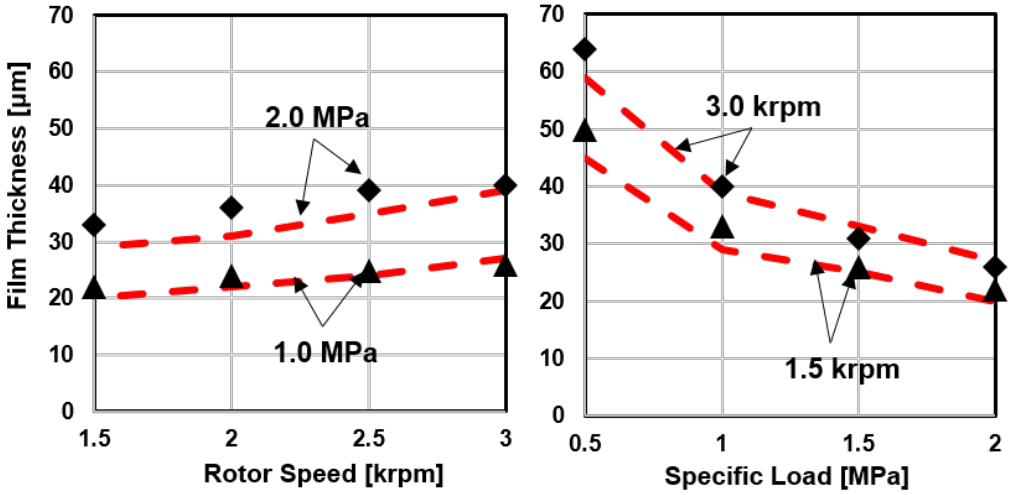

(b) Pad Trailing Edge Film Thickness vs. speed and vs. load

Fig. 10: TEHD predicted oil film thickness at the mean radius of the pad leading edge (top graphs) and trailing edge (bottom graphs) vs. test data from [58] for a six-pad TPTB. Oil supply temperature = 40℃.

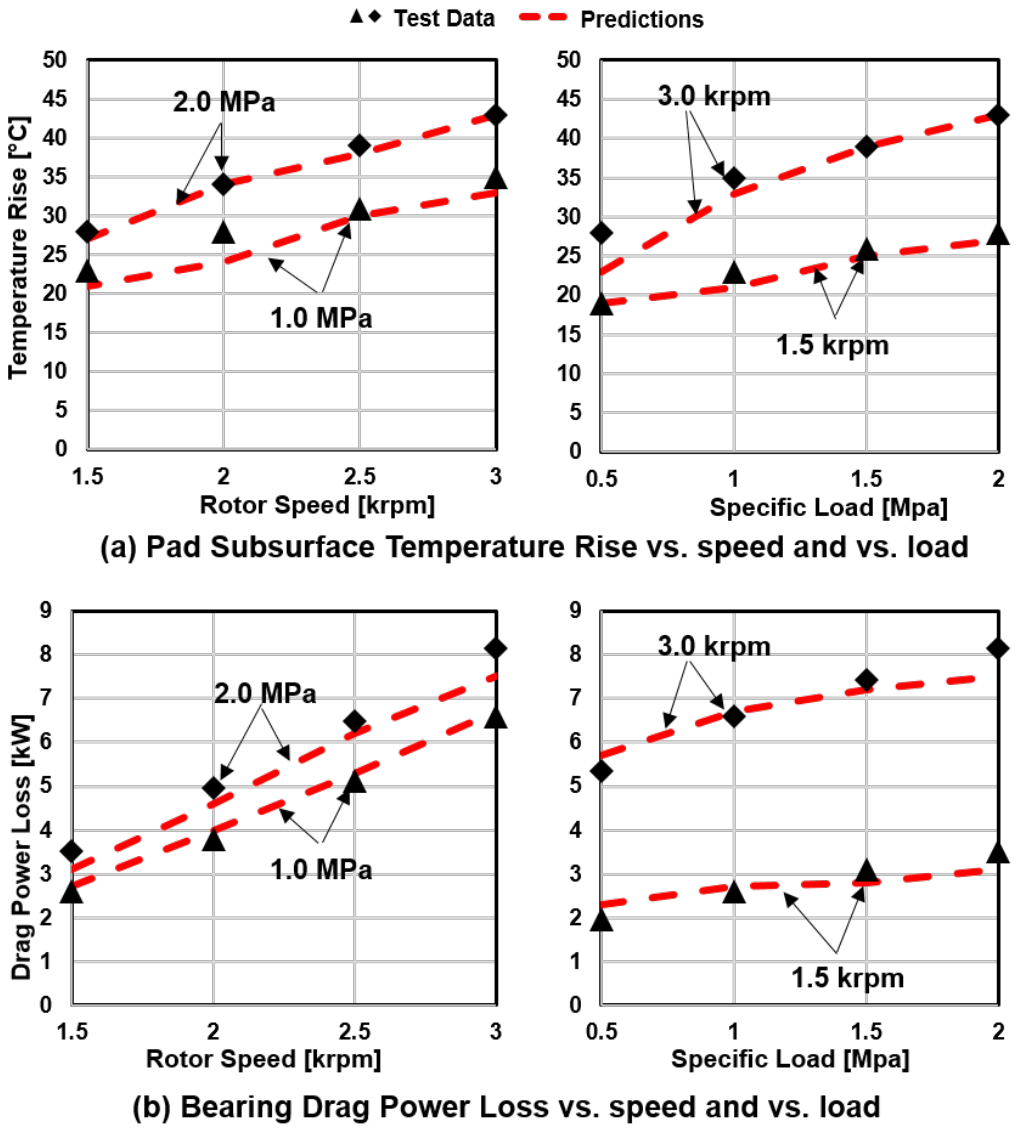

Fig. 11: TEHD predicted and measured [58] of pad subsurface temperature rise (top graphs) and and bearing drag power loss (bottom graphs) for a six-pad TPTB. Oil supply temperature = 40℃.

3.2.3 Validation of predictions vs. Measured Pad Subsurface Temperature for Turbulent Flow TPTB

Mikula [57] measures pad (subsurface) temperatures in a TPTB operating under both laminar and turbulent flow conditions. See Table4 for the bearing geometry, lubricant properties, and operating condition. The test bearing has eight pads with 267 mm in OD, 133 mm in ID, and 38° in arc length. The lubricant is VG32 oil at a supply temperature of 46°.

The following compares TEHD predictions against a measured pad subsurface temperature increase. In Ref. [57], a 2 mm thick babbitt layer covers the pad top surface and two thermocouples, 0.8 mm below the babbitt surface, locate at the pad mean radius, one at 15% of arc length upstream of the trailing edge, and the other one at 15% of arc length downstream of the leading edge.

The load applied (W_z) on the bearing varies between 24 kN and 123 kN, equivalent to a specific load per pad ($\frac{W_z}{A_P N_P}$) ranging from 0.69 to 3.44 MPa. The rotor speed ranges from 4 krpm to 13 krpm and gives a maximum surface speed between ΩR_o = 54 m/s and 181 m/s, and which determines operation in either a laminar flow, transition from laminar to turbulent flow, or turbulent flow regimes as based on the Reynolds number, Re=$\frac{\rho R_m \Omega h_{min}}{\mu}$. Recall the flow is laminar for operation at $Re < Re_L$ = 580, and transits to fully turbulent for $Re > Re_U$ = 800.

Figures 12 through 14 show the calculated Reynolds number for the test TPTB as well as the measured pad subsurface temperature rise vs. predictions from the current model.

Predictions are obtained at the same locations as those recorded by thermocouples installed in a pad.

Table 4: Geometry and operating condition for a TPTB from [57] used for analysis validation.

Bearing properties		
Number of pads, N_P		8
Inner diameter, ID		133 mm
Outer diameter, OD		267 mm
Pad arc length		38°
Pivot circum. offset		50 %
Pivot radial offset		50 %
Pad thickness*, t_P		25 mm
Babbitt thickness*		2 mm
Pad area, A_P		45.6 cm^2
Operating condition		
Specific load		0.6-3.5 MPa
Shaft rotational speed		4-13 krpm
Supply pressure*		0 bar
Fluid properties		ISO VG32
Viscosity-temperature coefficient, α^*_{TV}		0.0247 1/°C
Viscosity, μ_{Su} (at 46°C)		22 cPoise
Density, ρ		821 kg/m^3
Specific heat capacity, c_P		2.17 kJ/(kg· °C)
Thermal conductivity, κ		0.13 W/(m· °C)
Pad material properties	Steel	Babbitt
Thermal conductivity, κ_P	51 W/(m·°C)	55 W/(m·°C)
Elasticity modulus, E	210 GPa	52 GPa
Thermal expansion, α_T	12 10^{-6}/°C	24 10^{-6}/°C
Poisson ratio, ν	0.3	0.3
Thermal properties		
FE reference temperature**		20 °C
Thermal mixing coefficient.* λ_{mix}		0.4-0.6
Heat Transfer coefficient on back of pad** η		100 W/(m^2·°C)

*Assumed or calculated based on the available data .
**Taken from Ref.[35]

In Figure 12, the bearing operates at 4 krpm ($R_o\Omega$=54 m/s) and the maximum Reynolds number =540 for the lightest load (0.69 MPa) and decreases to 187 under the largest applied load (3.44 MPa). Hence, the flow is laminar as the operation remains below Re_L=580. The predictions of pad temperate rise based on the laminar flow model match well the test data, differing by no more than 3°C and 4°C at the pad leading edge and trailing edge, respectively.

In Figure 13, the bearing operates at 10 krpm ($R_o\Omega$=135 m/s) and $Re = 1,380 > Re_U$ at the lowest load (0.69 MPa), then drops to $Re = 676 < Re_U$ at the largest load (3.44 MPa). The measured pad subsurface temperature significantly increases at the pad trailing edge for specific loads higher than 2.75 MPa, thus evidencing a transition from turbulent flow (Re= 1,380) to a superlaminar flow condition (Re= 676). This flow transition is recognized by a rapid increase in the temperature as the thermal mixing in the flow lessens. In general, the current turbulent flow predictions show a good agreement with the test results. The maximum temperature difference is 11°C, amounting to 10% with respect to the measurements. Also note that predictions based on a laminar flow model for all conditions substantially differ from the test results with up to a 30° difference.

In Figure 14, the rotor speed ranges from 4 krpm to 13 krpm ($R_o\Omega$=54-181 m/s) and the specific load equals 3.44 MPa. Re= 199 at the lowest rotor speed (4 krpm) and thus the flow is laminar. With operation at rotor speed of 9 krpm, $Re \rightarrow 672 > Re_L = 580$, and the flow transits to the superlaminar flow condition. For rotor speeds above 11 krpm,

$Re > Re_U$=800, and the flow is fully turbulent. A transition from laminar flow to turbulent flow is evidenced by a fast drop in the pad temperature due to an enhanced thermal mixing of the flow. Observe that predictions based on the turbulent flow model closely follow the test data with a maximum difference of 8°C, that is 6% with respect to the measured temperature. Predictions derived from an *always* laminar flow model show a substantial difference, up to 50°C.

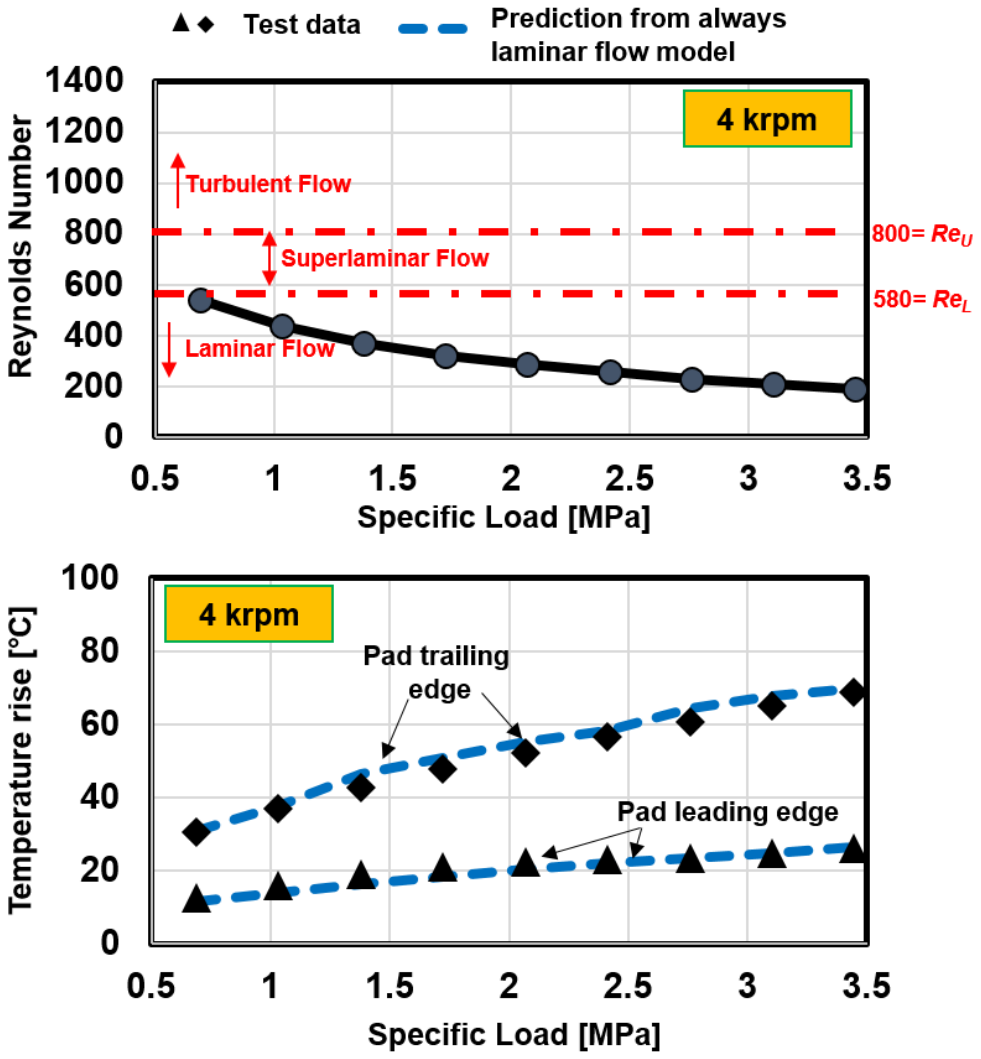

Fig. 12: TEHD predicted pad subsurface temperature rise derived from both a laminar flow model and a turbulent flow model vs. test data for a six-pad TPTB [57]. Oil supply temperature = 46℃, Rotor speed = 4 krpm. . Reprinted with permission from [2].

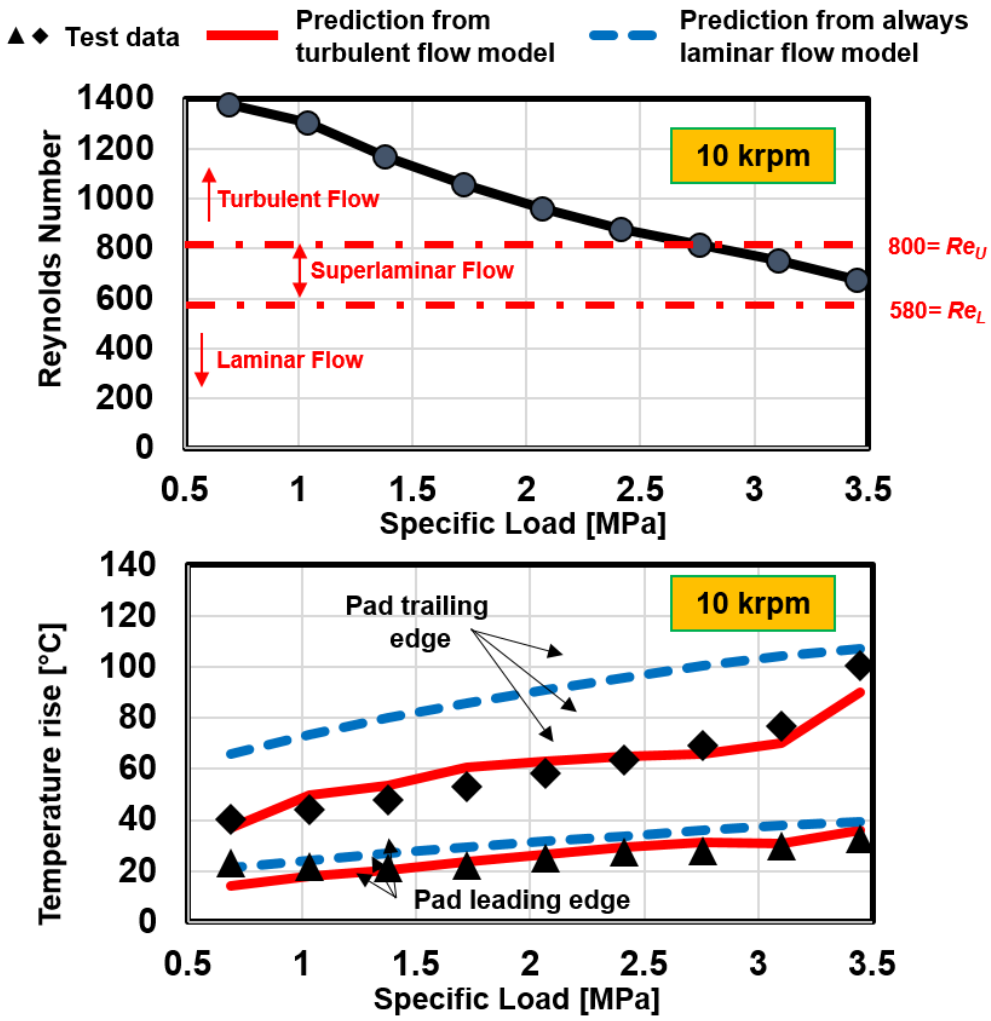

Fig. 13: TEHD predicted pad subsurface temperature rise derived from both a laminar flow model and a turbulent flow model vs. test data for a six-pad TPTB [57].Oil supply temperature = 46℃, Rotor speed = 10 krpm. Reprinted with permission from [2].

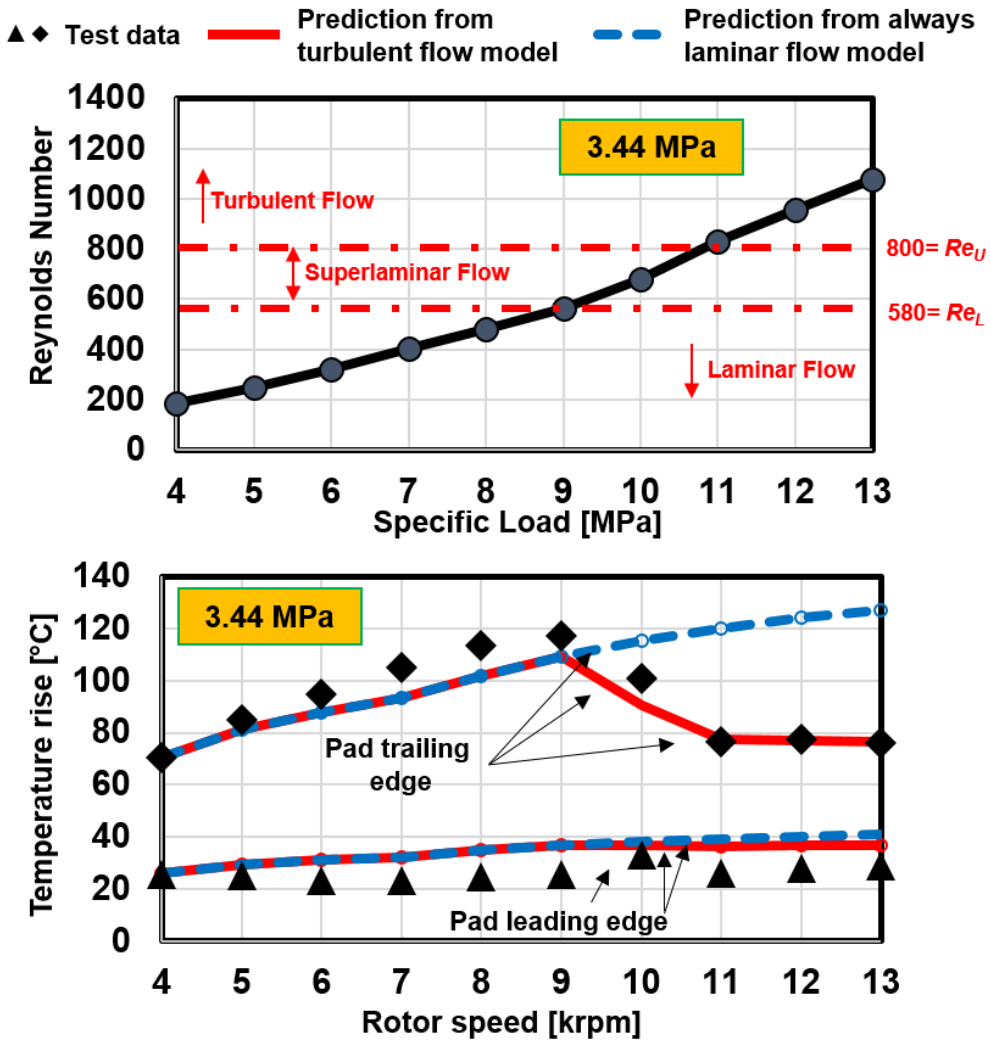

Fig. 14: TEHD predicted pad subsurface temperature rise derived from both a laminar flow model and a turbulent flow model vs. test data for a six-pad TPTB [57]. Oil supply temperature = 46℃, Specific load = 3.44 MPa. Reprinted with permission from [2].

4 A PREDICTIVE TOOL FOR THE ANALYSIS OF SELF-EQUALIZING TILTING PAD THRUST BEARING[7]

This section implements a model for the pad leveling system into the TEHD analysis tool (see the prior chapter) to deliver load performance analysis for self-equalizing TPTBs. The following describes the pad leveling system analysis, the validation of the analysis, and the load performance predictions for an example self-equalizing bearing.

4.1 Description of the Analysis for the Pad Leveling System

A self-equalizing TPTB includes a series of leveling plates. The lower plates carry the upper plates and upper plates support the bearing pads and which tilt and relocate to evenly distribute the load across the pads. Figure 15 depicts the geometry of a self-equalizing TPTB and definition of variables. The bearing pads pivot atop the upper plates; hence the pad fluid film thickness $h_{(r,\theta,t)}$ alters as the upper plates relocate along the axial direction h_u. The upper plates are themselves carried on the shoulders of the lower plates.

Therefore, the fluid film thickness Eqn.(1) extends to account the upper plate axial location h_u,

$$\begin{aligned} h^i_{(r,\theta,t)} &= [e_c - (e^i_P + t_P) - h^i_u] + (\varphi\, r)\sin\theta - (\psi\, r)\cos\theta \\ &+(\alpha^i\, r)\sin(\theta^i_P - \theta) + (\beta^i\, r)\cos(\theta^i_P - \theta) - (\beta^i\, R^i_P) + d^i_{(r,\theta,t)} \end{aligned} \qquad \theta^i_l < \theta < \theta^i_t \qquad (21)$$

[7]Reprinted with permission from material published by the author and advisor in Refs.[3, 59]

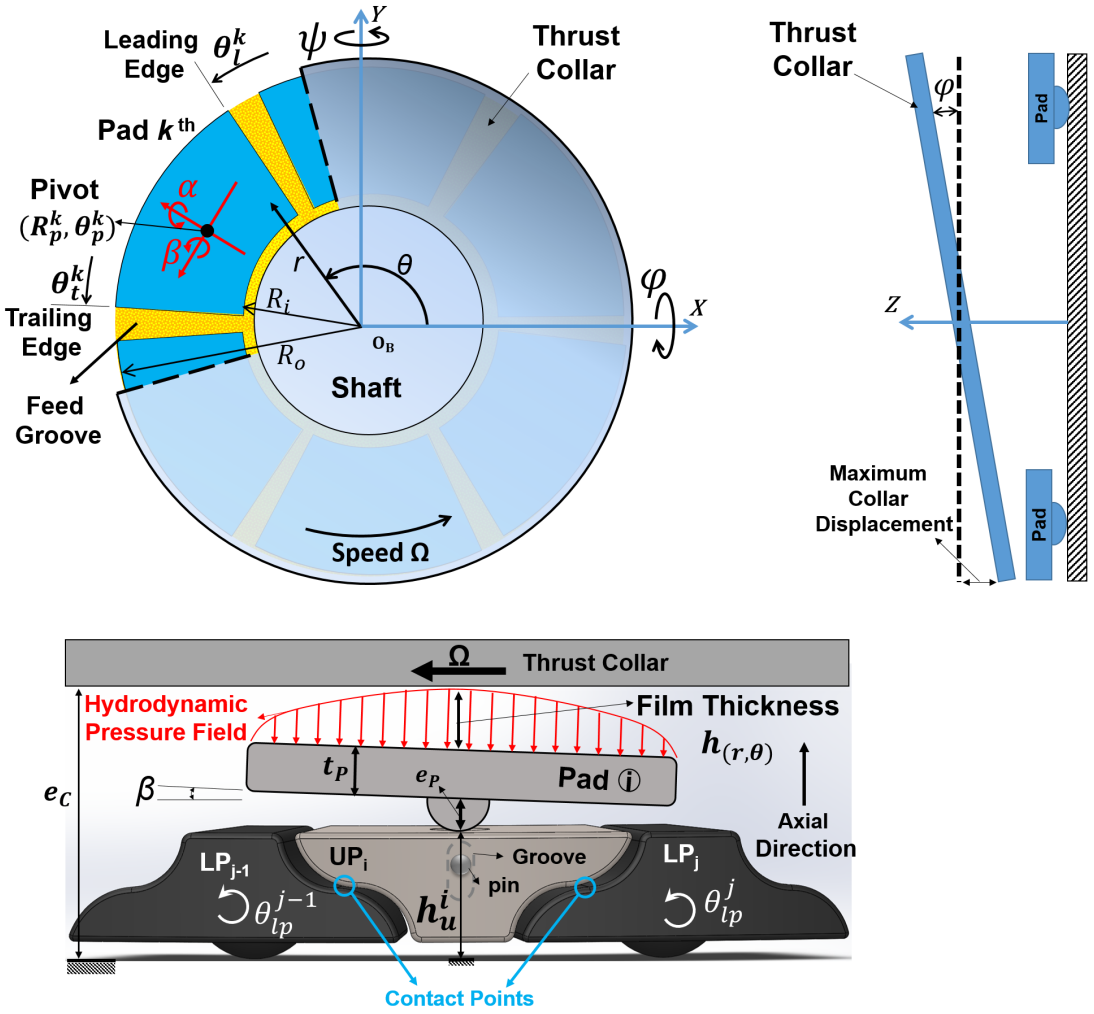

e_c	Thrust collar axial location.	t_P	Pad thickness.
e_P	Pivot thickness.	(X,Y,Z)	Cartesian coordinate system.
h	Fluid film thickness.	α, β	Pad radial and circumferential tilt angles.
h_u	Upper plates axial location.	θ_l, θ_t	Leading edge and trailing edge circumferential location.
O_B	Bearing housing center point.	φ, ψ	Misalignment angles of thrust collar around *y* and *x* axes.
(r,θ,z)	Global cylindrical coordinate system.	Ω	Shaft rotational speed
R_p, θ_p	Pivot radial and circumferential location.		
R_i, R_o	Pad inner and outer radius.		

Fig. 15: Schematic view of a self-equalizing TPTB with nomenclature for tilts of pads and plate. Reprinted with permission from [3].

Recall $e_{C)}$ and $e_{P)}$ are the axial locations of the thrust collar and pivot, respectively; $(\alpha_{(t)}, \beta_{(t)})$ are the pad tilt angle, and (φ, ψ) represent the thrust collar misalignment angles around x-axis and y-axis, respectively. (θ_l^i, θ_t^i) are the circumferential location of the pad leading edge and trailing edge, respectively.

Since the upper plates are carried by the lower plates, their location h_u varies as the lower plates tilt with angles (θ_{lp}). To model the pad leveling system, one should derive a model for the upper plates location as a function of the lower plates tilt angles. Pad leveling systems are available in several designs, each with distinct leveling plates' geometry, often proprietary to the manufacturer. Thus, deriving a single analytical model for all designs is impractical. To build an analysis tool applicable for a variety of designs, the analysis herein develops a numerical scheme that implements the leveling plates' geometry (both the upper plate and lower plate) from any commercial solid modeling software and performs an iterative approach to find the upper plates axial location based on the lower plates tilt angles. The solution also determines a location for the contact points between the leveling plates. Note the analysis only considers the angular tilting (θ_{lp} , see Fig. 15) of the leveling plates.

Figure 16 outlays a flowchart for the various tasks performed. Each task is self-explanatory including a decision ascertaining the line contacts, tasks (4) and (5) enforced by tasks (7) and (8). Tasks (9) through (11) pertain to updating the film thickness and performing the TEHD analysis to obtain the film pressure, and the temperature and de-

formation fields in the films and pads, and with a final outcome delivering forces and moments. On task (12), the check on the balance of moments on the lower plates determines convergence; otherwise the tilt angle of the leveling plates changes in reaction to the direction and magnitude of the imbalanced moments acting on them. A final task (15) verifies convergence on the applied loads; otherwise the algorithm routes the process to a new beginning with task (3).

Figure 17(a) shows predictions from the analysis for an example pad leveling system and that demonstrates the numerical scheme, steps (4) through (8), to find the axial displacement of the upper leveling plates h_u. The leveling plates have 50 mm in circumferential length at the bearing mid radius. With both the lower plates held at a flat position (zero tilting), the upper plate also positions flat with a nominal axial location of h_u = 15.601 mm. As the lower leveling plates tilt, say to $\theta^1_{lp} = 8^\circ$ and $\theta^2_{lp} = 4^\circ$ the upper plate relocates h_u = 16.196 mm, i.e. an upward displacements of $\Delta h_u = 595\mu$m. Note the leveling plates tilt angles are exaggerated here for demonstration purposes. In practice, the tilt angles of the leveling plates are very small, θ_{lp} <1°. Figure 17(b) shows predictions for the upper plate axial displacement from a nominal position as a function of the lower plates tilt angles up to 1°around a flat position. Accordingly, the pad moves downward $\Delta h_u = -334\mu$m (away from the collar to open the fluid thickness) with $\theta^1_{lp} = 1^\circ$ and $\theta^2_{lp} = -1^\circ$ and lifts $\Delta h_u = 338\mu$m (to close the film thickness) when $\theta^1_{lp} = 1^\circ$ and $\theta^2_{lp} = -1^\circ$.

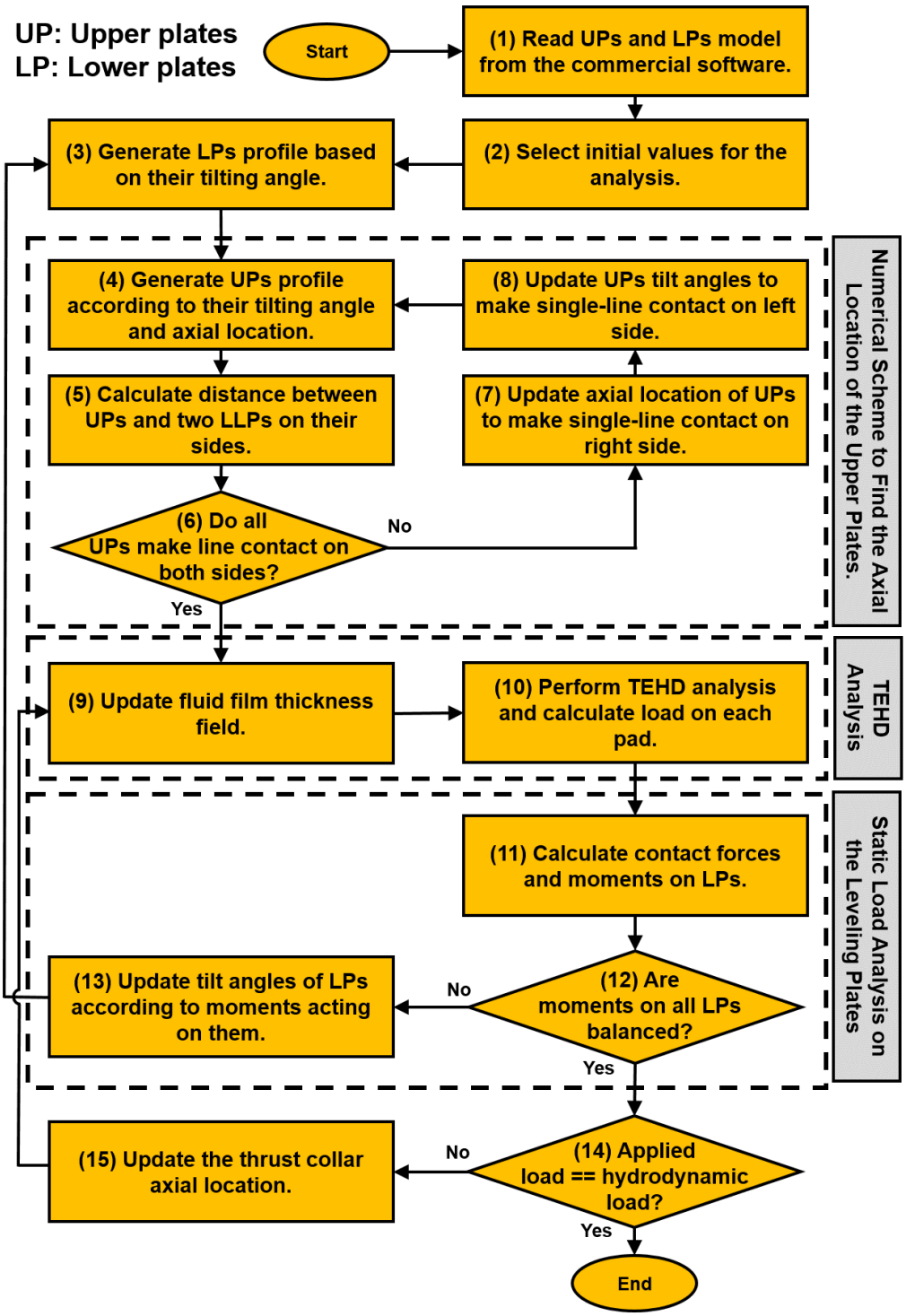

Fig. 16: Flowchart of analyses performed including a numerical scheme to find contact between leveling plates, TEHD analysis, and static force analysis. Reprinted with permission from [3].

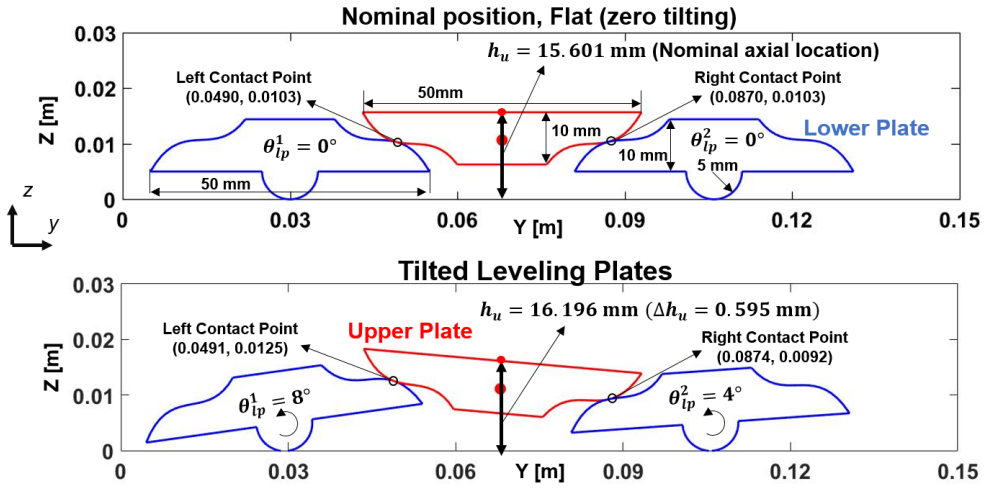

(a) Contact between Leveling Plates

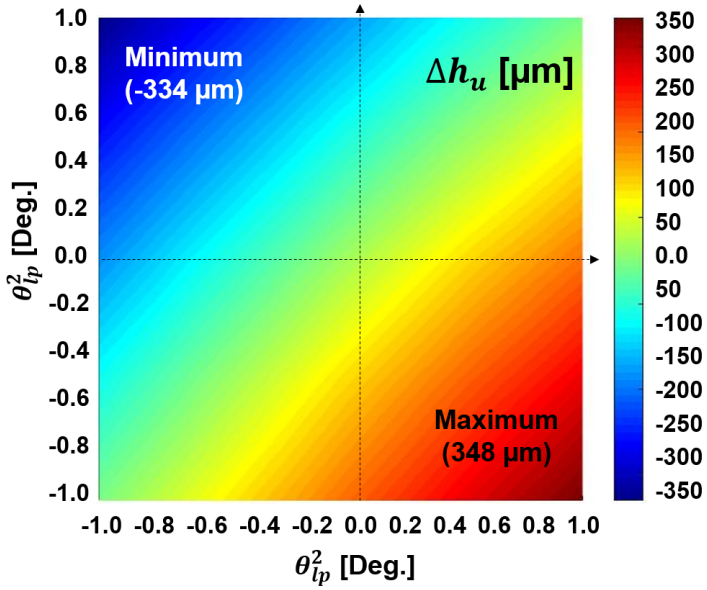

(b) Relative Displacement of Upper Plate

Fig. 17: Position of an upper plate with flat lower plates (with no tilting) and for tilted lower plates. (b) Predicted axial displacement of an upper plate relative to nominal height vs. lower plates tilt angles. Reprinted with permission from [3].

4.1.1 Analysis for the Static Forces and Null Moments in a Pad Leveling System

Figure 18 shows a schematic view of an upper plate making contact with two lower plates. An equivalent hydrodynamic load $\vec{\mathbf{F}}^{n}_{pad}$ (normal)[8] and a tangential frictional force $\vec{\mathbf{F}}^{f}_{piv}$ acts where the pad pivot seats at the top surface of the upper plate. A pin attached to the upper plates that slides inside a groove in the bearing housing (or the other way around) prevents the upper plates from displacing along the y-axis (horizontal direction). Thus, force $\vec{\mathbf{F}}^{n}_{pin}$ acts on the upper plates at the pin location.

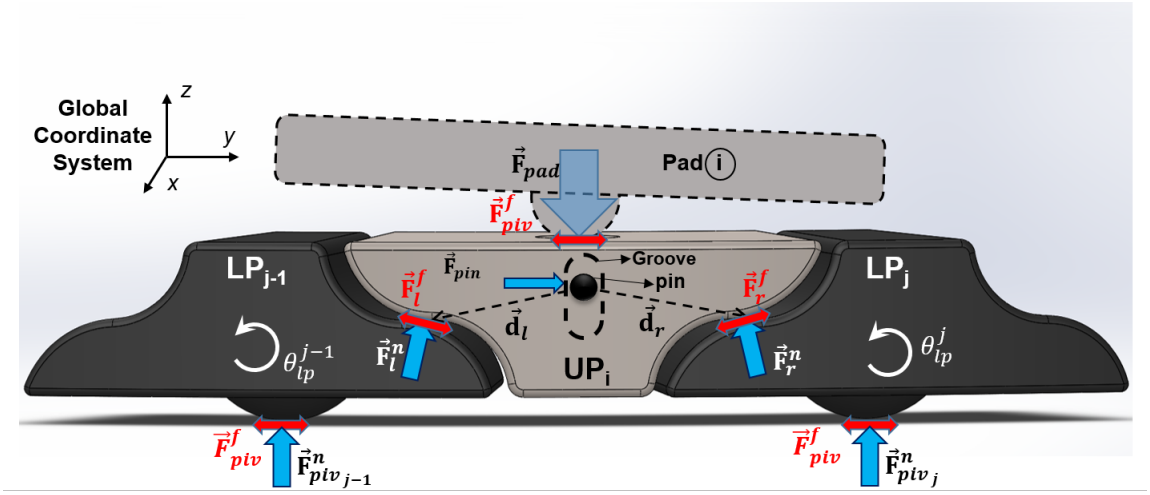

Fig. 18: Schematic view of a thrust pad and support upper plate, both carried on the shoulders of two adjacent lower plates. Forces acting on the plates shown. Reprinted with permission from [3].

For an upper plate to be at an equilibrium state, the forces and moments acting on it should balance. Assuming the weight of the leveling plates is negligible, the equations for

[8] A shear force from the fluid film, perpendicular to the acting normal force, is not considered as in practice it is insignificant.

force and moment balance in an upper plate are,

$$\sum \vec{\mathbf{F}} = \vec{\mathbf{F}}^n_l + \vec{\mathbf{F}}^f_l + \vec{\mathbf{F}}^n_r + \vec{\mathbf{F}}^f_r + \vec{\mathbf{F}}^n_{pin} + \vec{\mathbf{F}}^n_{pad} + \vec{\mathbf{F}}^f_{piv} = 0 \tag{22a}$$

$$\sum \vec{\mathbf{M}}_{pin} = \vec{\mathbf{d}}_l \times [\vec{\mathbf{F}}^n_l + \vec{\mathbf{F}}^f_l] + \vec{\mathbf{d}}_r \times [\vec{\mathbf{F}}^n_r + \vec{\mathbf{F}}^f_r] + \vec{\mathbf{d}}_{pad} \times [\vec{\mathbf{F}}^n_{pad} + \vec{\mathbf{F}}^f_{piv}] = 0 \tag{22b}$$

where vector $\vec{\mathbf{d}} = (d^y, d^z)$ is the distance from the pin to a force acting point, and $\vec{\mathbf{F}}^n$ is the normal force at a contact point and $\vec{\mathbf{F}}^f$ is the respective tangential (friction) force. Solution of Eqns. (22) yields a magnitude for the contact forces acting on the left side ($|\vec{\mathbf{F}}^f_r|$) and right side ($|\vec{\mathbf{F}}^f_l|$) of the upper plate,

$$|F_l| = \frac{v^z_{pad}(d^y_r v^z_r - d^z_r v^y_r) - v^z_r(d^y_{pad} v^z_{pad} - d^z_{pad} v^y_{pad})}{v^z_l(d^y_r v^z_r - d^z_r v^y_r) - v^z_r(d^y_l v^z_l - d^z_l v^y_l)} |F_{pad}| \tag{23a}$$

$$|F_r| = \frac{v^z_l(d^y_{pad} v^z_{pad} - d^z_{pad} v^y_{pad}) - v^z_{pad}(d^y_l v^z_l - d^z_l v^y_l)}{v^z_l(d^y_r v^z_r - d^z_r v^y_r) - v^z_r(d^y_l v^z_l - d^z_l v^y_l)} |F_{pad}| \tag{23b}$$

where $|\vec{\mathbf{F}}^n_{pad}|$ is the magnitude of the hydrodynamic force acting on a pad top surface.

As stated in Ref. [60], a friction force at a bearing pad pivot is either a sliding friction for a ball and socket type, or a rolling friction for a rocker back type. The friction forces at the contact points between leveling plates are sliding friction as the leveling plates are assumed to remain fixed along the y-axis. The friction forces at the contact point of the lower plates pivot and the bearing housing might be either sliding or rolling based on the type of pivot in the lower plates. For both sliding and rolling type motions, the friction

force is modeled using a friction coefficient (μ). The rolling and sliding friction forces are

$$\text{Rolling friction} \qquad |F^f| \leq \mu_r |F^n| \tag{24a}$$

$$\text{Sliding friction} \qquad |F^f| \leq \mu_s |F^n| \tag{24b}$$

where μ_r is a rolling friction coefficient with a typical value ranging from 0.01 to 0.1 [61] and μ_s is a sliding friction coefficient ranging from 0.01 to 0.4 [62]. Both the sliding and rolling friction coefficients are functions of the materials elastic modulus and hardness, the lubricant properties, and surface condition [63]. Particular to a pad leveling system, their surface condition varies over the time as the leveling plates do wear.

At a contact point, the total force (equals the sum of normal and friction forces) is,

$$\vec{\mathbf{F}} = \vec{\mathbf{F}}^n + \vec{\mathbf{F}}^f = |F^n|\vec{\mathbf{n}} + \mu|F^n|\vec{\mathbf{t}} = |F^n|\left(\vec{\mathbf{n}} + \mu\,\vec{\mathbf{t}}\right) = |F^n|\sqrt{1+\mu^2}\begin{Bmatrix} v_l^y \\ \\ v_l^z \end{Bmatrix} = |F|\vec{\mathbf{v}} \tag{25}$$

here $\vec{\mathbf{F}}$ and $\vec{\mathbf{v}}$ represent the magnitude and direction vector for the resultant force, respectively.

Figure 19 shows a schematic view of a lower plate carrying two upper plates on its shoulders. The friction forces at the contact points of the leveling plates are of sliding type whereas the friction force at the pivot is of rolling type. Hence, the moment acting on the

lower plate is,

$$\vec{M}_{piv} = \vec{\mathbf{d}}_l \times \vec{\mathbf{F}}_l + \vec{\mathbf{d}}_r \times \vec{\mathbf{F}}_r + \vec{\mathbf{d}}_{piv} \times \vec{\mathbf{F}}_{piv} \rightarrow 0 \tag{26}$$

where, $\vec{\mathbf{d}}$ is a distance from the lower plate mass center to the respective contact point. Note the forces $\vec{\mathbf{F}}_r$ and $\vec{\mathbf{F}}_l$ represent an equivalent force at the contact points, each equal to the sum of the normal force and friction forces, see Eqn. (25).

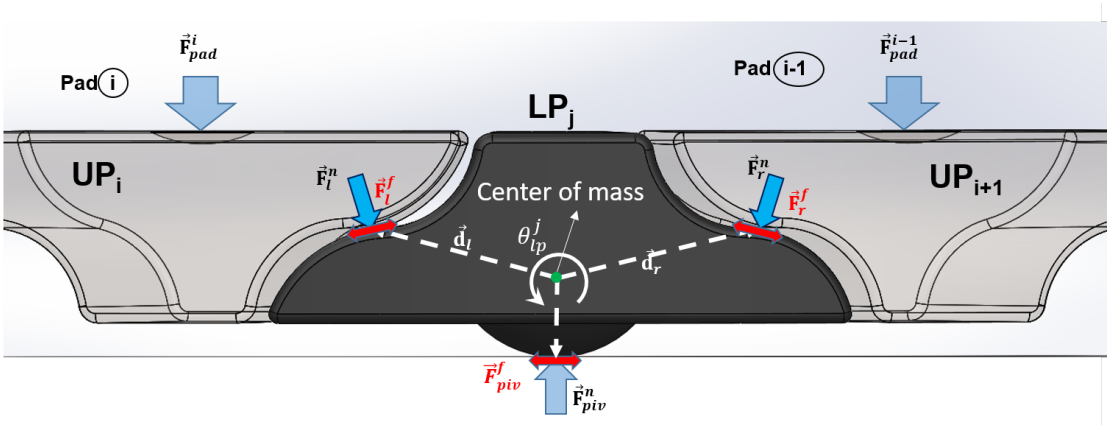

Fig. 19: Schematic view of a lower plate holding two upper plates on its shoulders. Forces acting on the plates shown. Reprinted with permission from [3].

Once the moments acting on the lower plates are derived, the algorithm performs a Newton-Raphson technique to obtain the lower plates tilt angles (θ_{lp}) that satisfy the balance of moments on them. Expanding the moment Eqn. (26) in a Taylor series about an equilibrium point (${}^0\theta^i_{lp}$ where $i = 1, \ldots, N_{pad}$) gives,

$$\vec{M}^i_{piv}\Big|_{(\theta^1_{lp},\ldots,\theta^{N_{Pad}}_{lp})} = \vec{M}^i_{piv}\Big|_{(\theta^1_{l_0},\ldots,\theta^{N_{Pad}}_{l_0})} + \sum_{j=1}^{N_{Pad}} K_{\Theta_{ij}}(\theta^j_{lp} - \theta^j_{l_0}) \tag{27}$$

where $K_{\Theta_{ij}}$ is a moment/tilt stiffness coefficient obtained using a first degree forward finite difference method, i.e,

$$K_{\Theta_{ij}} = \left.\frac{\partial \vec{M}^i_{piv}}{\partial \theta^j_{lp}}\right|_{(\theta^1_{lp},\ldots,\theta^{N_{Pad}}_{lp})} \tag{28}$$

Note the number of both lower plates and upper plates in a self-equalizing TPTB equals to the number of pads ($Npad$). Then, the lower plates tilt angles at each iteration of the Newton-Raphson technique are,

$$\{\theta\} = \{{}^0\theta\} + [\mathbf{K}_\theta]^{-1}\{M_{piv}\} \tag{29}$$

$$\begin{Bmatrix} \theta^1_{lp} \\ \theta^2_{lp} \\ \theta^3_{lp} \\ \vdots \\ \theta^{N_{Pad}}_{lp} \end{Bmatrix} = \begin{Bmatrix} {}^0\theta^1_{lp} \\ {}^0\theta^2_{lp} \\ {}^0\theta^3_{lp} \\ \vdots \\ {}^0\theta^{N_{Pad}}_{lp} \end{Bmatrix} - \begin{bmatrix} \frac{\partial \vec{M}^1_{piv}}{\partial \theta^1_{lp}} & \frac{\partial \vec{M}^1_{piv}}{\partial \theta^2_{lp}} & \frac{\partial \vec{M}^1_{piv}}{\partial \theta^3_{lp}} & \cdots & \frac{\partial \vec{M}^1_{piv}}{\partial \theta^{N_{Pad}}_{lp}} \\ \frac{\partial \vec{M}^2_{piv}}{\partial \theta^1_{lp}} & \frac{\partial \vec{M}^2_{piv}}{\partial \theta^2_{lp}} & \frac{\partial \vec{M}^2_{piv}}{\partial \theta^3_{lp}} & \cdots & \frac{\partial \vec{M}^2_{piv}}{\partial \theta^{N_{Pad}}_{lp}} \\ \frac{\partial \vec{M}^3_{piv}}{\partial \theta^1_{lp}} & \frac{\partial \vec{M}^3_{piv}}{\partial \theta^2_{lp}} & \frac{\partial \vec{M}^3_{piv}}{\partial \theta^3_{lp}} & \cdots & \frac{\partial \vec{M}^3_{piv}}{\partial \theta^{N_{Pad}}_{lp}} \\ \vdots & \vdots & \vdots & \ddots & \vdots \\ \frac{\partial \vec{M}^{N_{Pad}}_{piv}}{\partial \theta^1_{lp}} & \frac{\partial \vec{M}^{N_{Pad}}_{piv}}{\partial \theta^2_{lp}} & \frac{\partial \vec{M}^{N_{Pad}}_{piv}}{\partial \theta^3_{lp}} & \cdots & \frac{\partial \vec{M}^{N_{Pad}}_{piv}}{\partial \theta^{N_{Pad}}_{lp}} \end{bmatrix}^{-1} \begin{Bmatrix} \vec{M}^1_{piv} \\ \vec{M}^2_{piv} \\ \vec{M}^3_{piv} \\ \vdots \\ \vec{M}^{N_{Pad}}_{piv} \end{Bmatrix} \tag{30}$$

4.1.2 Hertz Contact Analysis for the Leveling Plates

The analysis in the prior section, see Eqns.(21), calculates a magnitude for the forces acting on the contact points of the leveling plates, left and right. This section describes a Hertz contact analysis model using the contact forces to predict a peak pressure over the contact area. The contact between the leveling plates is modeled as a cylinder-on-

cylinder solid contact (line), as shown in Fig.20. Note the wear rate at the contact area of the leveling plates directly relates to the contact pressure. Hence, a proper leveling plates design should minimize the peak pressure at the contact area.

The analysis adopts well known formulas stated by Shigley [64]. Let E and v be the elastic modulus and the Poison ratio for the leveling plates material, respectively, the peak pressure over the leveling plates contact area as [64],

$$P_{max} = \frac{2F}{\pi b L} \tag{31}$$

where

$$b = \sqrt{\frac{8F\frac{1-v^2}{E}}{\pi L\left(\frac{1}{R_1}+\frac{1}{R_2}\right)}} = \sqrt{\frac{8\frac{1-v^2}{E}}{\pi L\left(\frac{1}{R_1}+\frac{1}{R_2}\right)}}\sqrt{F} \tag{32}$$

with b as half of the half-width of the contact area, L as the length of the contact, and F is the magnitude of the contact force. Above R_1 and R_2 are the surface radii curvature at the line of contact as Figure 20 shows [64].

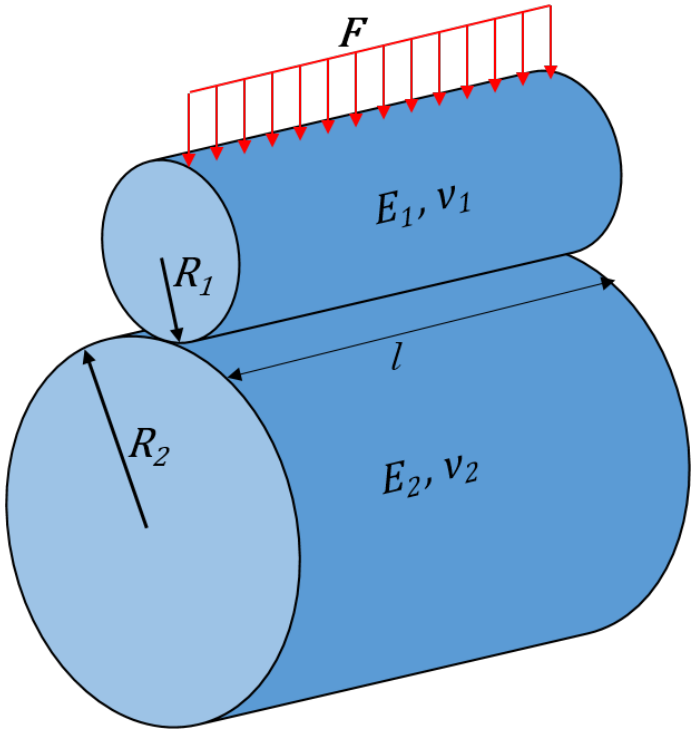

Fig. 20: Schematic view of line contact between two cylinders (non conformal surfaces). Reprinted with permission from [3].

4.2 Validation of Static Force and Contact Analyses

To evaluate the present analysis, this section models an example pad leveling system in a commercial finite element software tool (ANSYS® Mechanical) to perform analysis and to benchmark the results versus predictions delivered by the present model. The pad leveling system includes lower plates and upper plates assembled on the bearing housing. Figure 21 shows the leveling plates modeled using the commercial software; the graphs depict an exploded mode and an assembled mode.

The pad leveling system modeled here is a part of a test self-equalizing TPTB with 126.8 mm in OD and 63.4 mm in ID. The bearing operating condition determines the load applied on each pad and which is transferred to the upper plates through the pad pivots. Figure 22 shows leveling plates meshed by the commercial software with boundary conditions imposed on them to perform the contact analysis. The equivalent hydrodynamic load is applied on the mean radial length of the upper plate top surface exactly where the pad pivot seats. The groove on the upper plate outer radius is set to zero displacement along the radial and circumferential directions to simulate the restrictive pin in the actual design. Based on the measured contact frictions reported[9] in [61], the friction coefficient $\mu_s = 0.2$ is used to account for the frictional contacts between the leveling plates.

[9]Ref. [61] states that for temperature < 200 °C, the measured sliding friction coefficients for several sample materials including steel-on-steel and copper-on-copper are roughly same, $\mu_s \approx 0.2$.

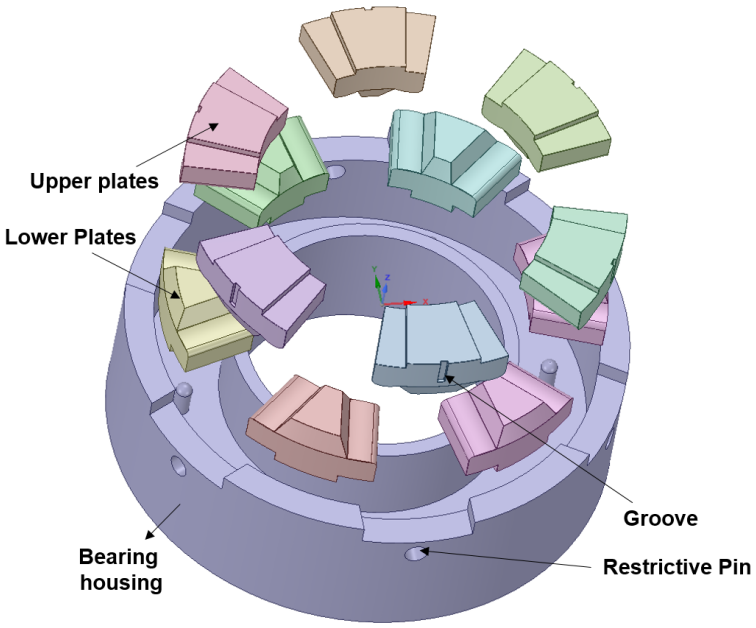

(a) Exploded View Mode

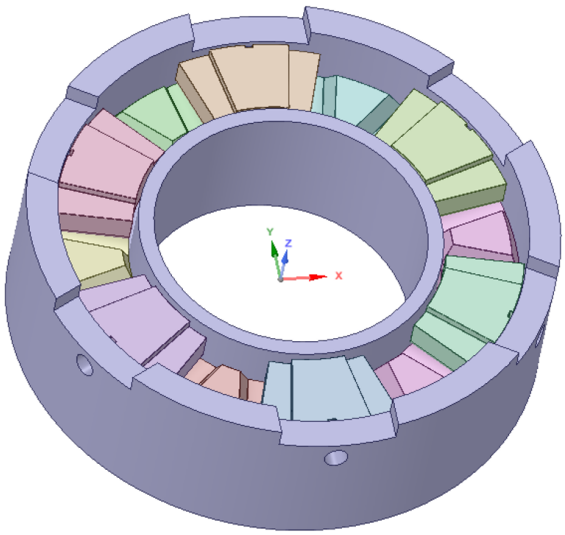

(b) Assembled View Mode

Fig. 21: A pad leveling system modeled in a commercial finite element software to perform contact analysis. Reprinted with permission from [3].

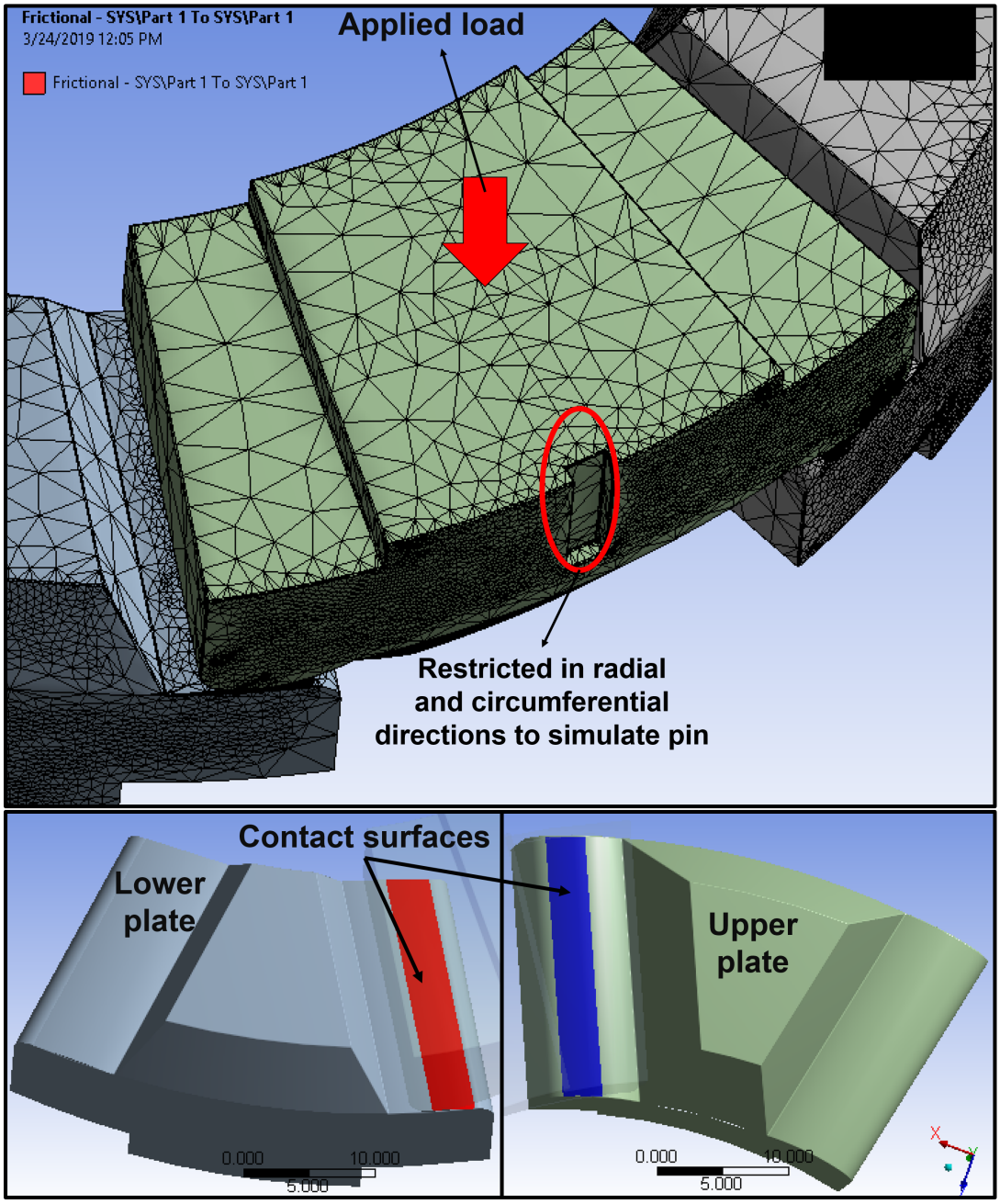

Fig. 22: Boundary conditions applied on leveling plates and the arrangement of contact surfaces to perform analysis in a commercial FEM software. Reprinted with permission from [3].

Figure 23 through 25 portray contact analysis from the commercial software for the example equalizing system under an applied load on the upper plates ranging from 664 N to 4650 N. The range of applied load relates to the thrust bearing operating under a light load of 0.5 MPa to a heavy load of 3.5 MPa specific load per pad. The outputs of the analysis are a contact status map and the pressure profile over the contact area. In Figure 23, operating under a light load of 664 N load per pad, the peak pressure at the contact points of the leveling plates ranges from 314 MPa to 372 MPa over the contact line except for near the edges where stress concentration occurs and the peak pressure rises up to 490 MPa. The status of the contact region shows the upper plate slides over the surface of the lower plate. In Figure 25 with the load increasing to 4650 N, the peak pressure ranges from 745 MPa to 890 MPa over the center of the contact line and to 1780 MPa at the edges of the line contact.

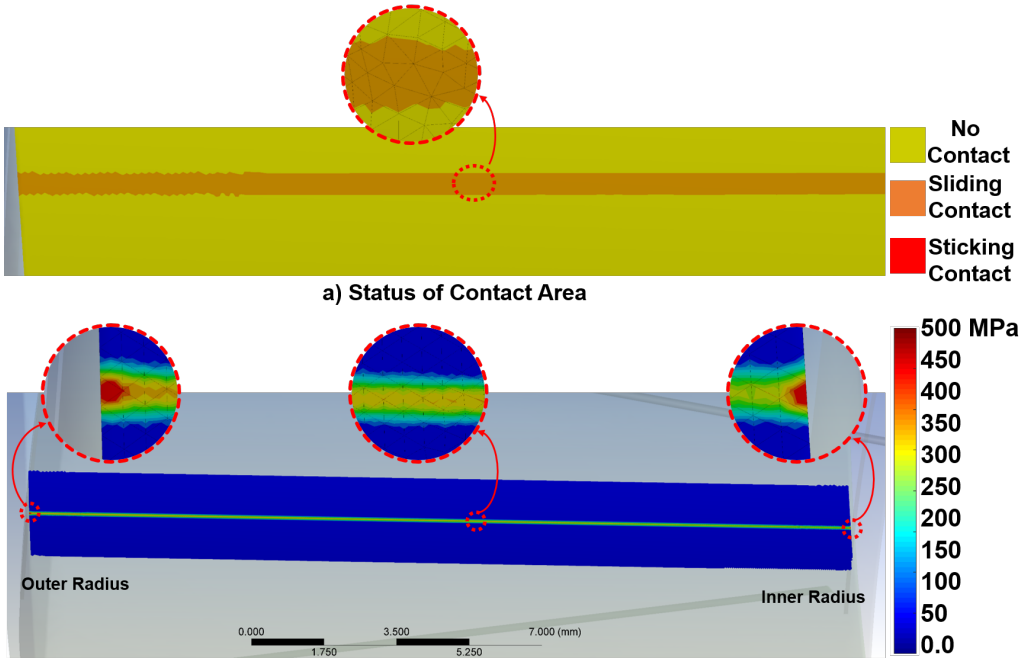

Fig. 23: Contact analysis on leveling plates under 664 N load equivalent to a heavy load of 3.5 MPa specific pressure per pad. Friction coefficient μ_s=0.2.

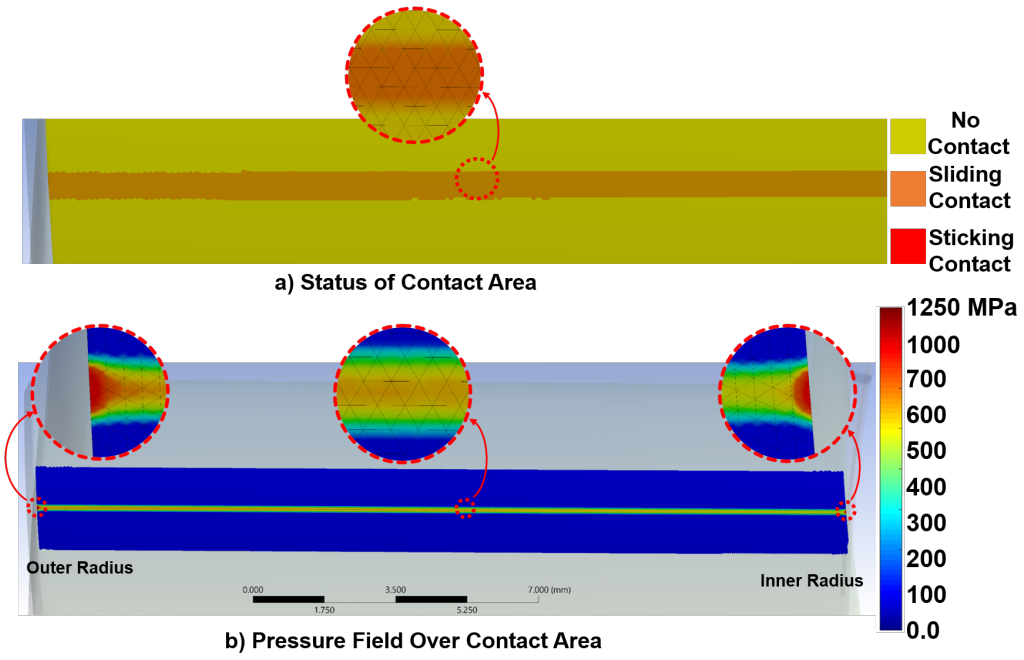

Fig. 24: Contact analysis on leveling plates under 2630 N load equivalent to a heavy load of 3.5 MPa specific pressure per pad. Friction coefficient μ_s=0.2.

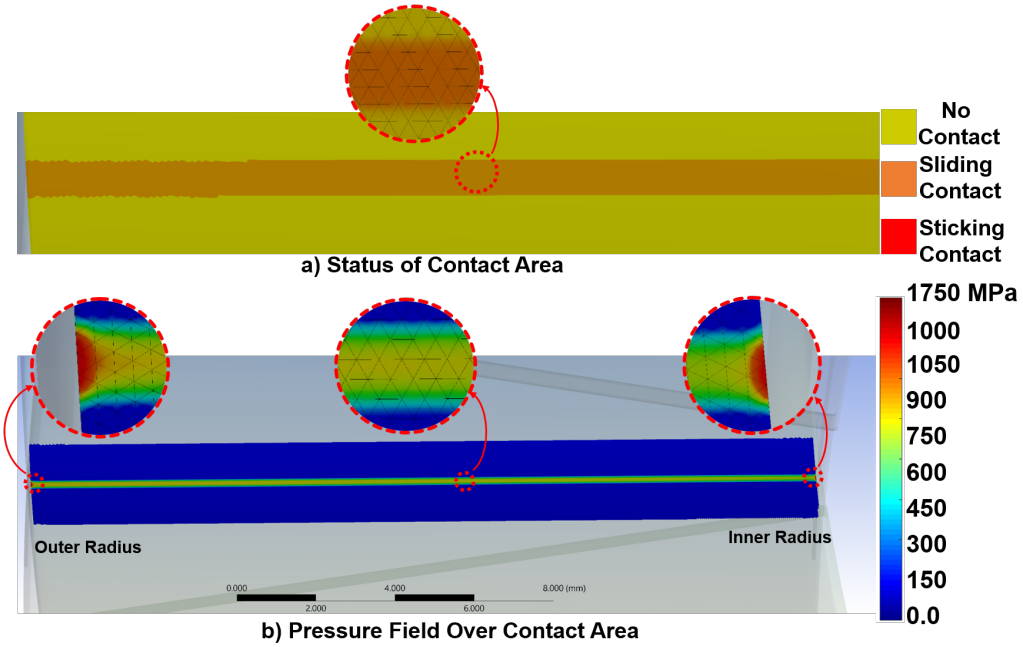

Fig. 25: Contact analysis on leveling plates under 4560 N load equivalent to a heavy load of 3.5 MPa specific pressure per pad. Friction coefficient μ_s=0.2. Reprinted with permission from [3].

Figure 26 compares the peak contact pressures delivered by the commercial FE analysis software against those produced by the Hertz contact analysis implemented in the present model versus pad specific load ranging from 0.5 MPa to 3.5 MPa. The friction coefficient for the FE analysis is μ= 0.2. The predicted commercial software. Note the results depicted in Fig. 11 do not include the stress concentration at both ends of the contact line.

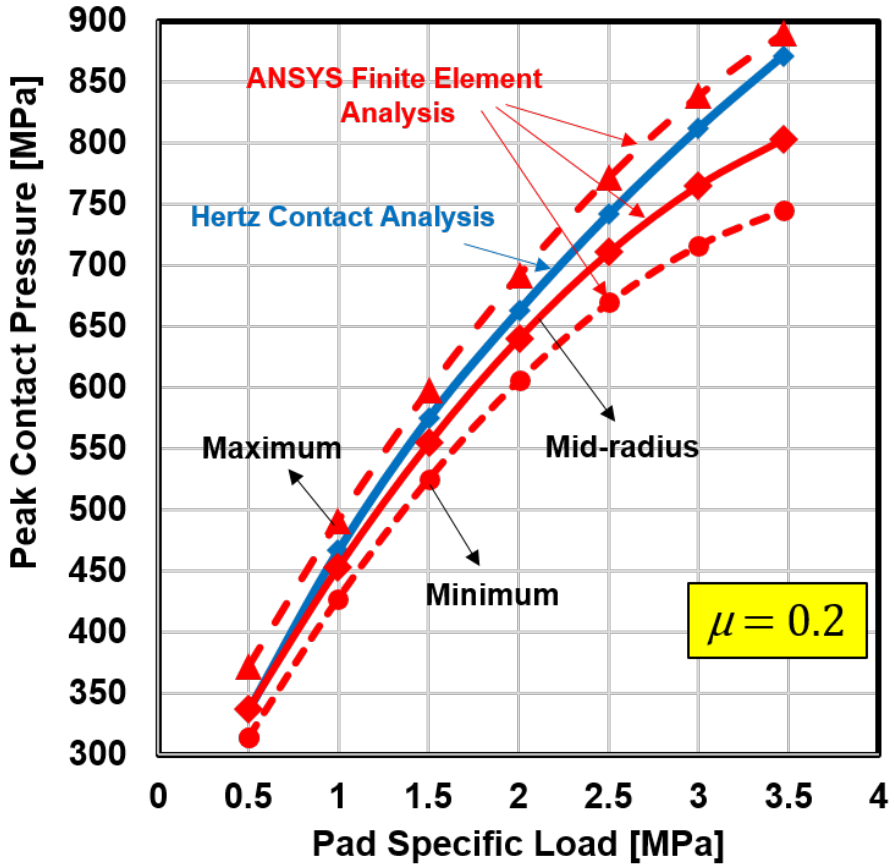

Fig. 26: Comparison of peak contact pressure on leveling plates vs pad specific load predicted by a commercial software finite element analysis and by a Hertz contact analysis. Friction coefficient μ_s=0.2. Reprinted with permission from [3].

4.3 Load Performance Predictions for an Example Self-Equaling TPTB

This section describes thermo-elasto-hydrodynamic (TEHD) predictions from the current model for an example self-equalizing TPTB . Table 5 details the example bearing geometry, lubricant properties, and operating conditions. In brief, the bearing has six pads with 126.8 mm in OD and 50° in arc length and operates at 4.0 krpm ($Ro\Omega$ = 26.8 m/s) and under specific load ranging from 1 MPa to 3 MPa per pad, i.e., light to heavy load conditions. Figure 27 depicts a schematic view of the arrangement of pads and leveling plates with respect to a global coordinate system (X, Y, Z). See prior sections for the geometry of the pads' leveling system. To lubricate the bearing, a mineral ISO VG32 oil is supplied at an inlet temperature of 46 ° C.

For operation at 4 krpm and under a 2 MPa specific load/pad, Figures 28 through 30 portray characteristic load performance predictions assuming a thrust collar static misalignment with angle $\phi = 0.01°$ around the X-axis. Note the maximum axial displacement $R_o\phi$= 11.25 μm, about 75% of the nominal minimum film thickness (=14.9 μm) should the bearing operate under 2 MPa load/pad and without collar misalignment. Note $\phi > 0$, a positive rotation around X, opens the film thickness on pads ① to ③ and closes the film on pads ④ to ⑥ .

Table 5: Geometry and operating conditions for an example self-equaling TPTB used for demonstrating predictions delivered by the present model. Reprinted with permission from [3].

Bearing properties			
Number of pads, N_P		6	-
Inner diameter, ID		63.4	mm
Outer diameter, OD		126.8	mm
Pad arc length		50	°
Pivot circumferential offset		50	%
Pivot radial offset		50	%
Pad thickness, t_P		14.5	mm
Babbitt thickness*		2	mm
Pad area, A_P		13.14	cm^2
Operating condition			
Specific load		1-3	MPa
Shaft rotational speed		4	krpm
Supply pressure*		0	bar
Fluid properties		ISO VG32	
Viscosity-temperature coefficient, α^*_{TV}		0.0247	1/°C
Viscosity, μ_{Su} (at 46°C)		22	cPoise
Density, ρ		821	kg/m^3
Specific heat capacity, c_P		2.17	kJ/(kg· °C)
Thermal conductivity, , κ		0.13	W/(m· °C)
Pad material properties	Steel	Babbitt	
Thermal conductivity, κ_P	51	55	W/(m·°C)
Elasticity modulus, E	210	52	GPa
Thermal expansion, α_T	12	24	10^{-6}/°C
Poisson ratio, ν	0.3	0.3	-
Analysis Assumptions			
Finite Element reference temperature*		20	°C
Thermal mixing coefficient.* λ_{mix}		0.4-0.6	
Heat Transfer coefficient on back of pad* η		100	W/(m^2·°C)

*Assumed or calculated based on the available data .

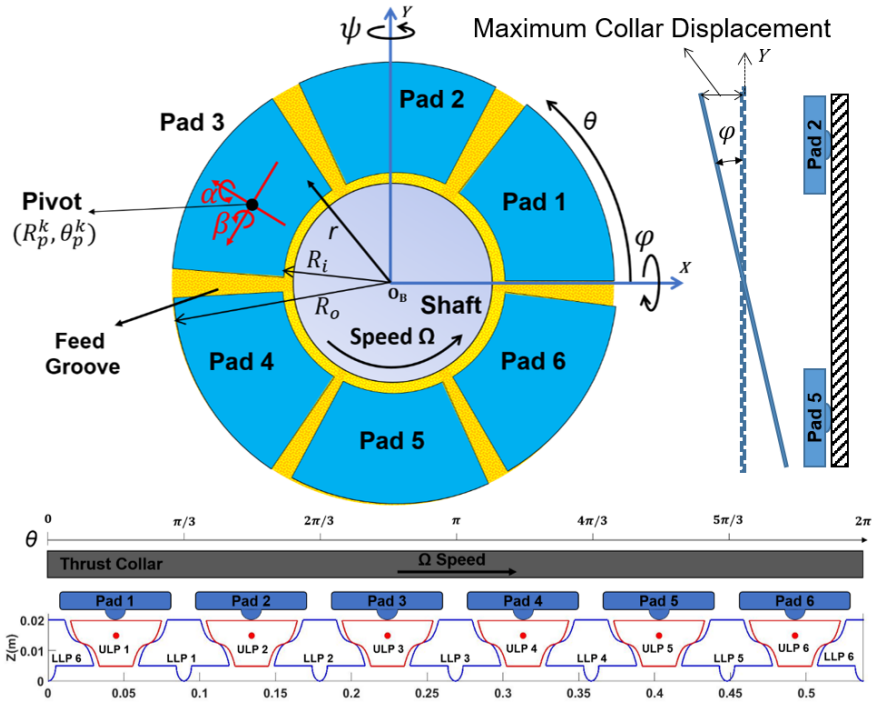

Fig. 27: Schematic view of an example self-equalizing TPTB. Reprinted with permission from [3].

Predictions follow for three cases. A first case, (a) without including the pad leveling system model to simulate the performance of a regular (non-equalizing) TPTB. A second case, (b) with the pad leveling system model included but disregarding the friction forces, i.e. an ideal performance. And a third case, (c) with the pad leveling system model included and accounting for the friction forces at the contact points, i.e., a more realistic performance. The sliding friction coefficient and rolling friction coefficient used for case (c) are μ_s= 0.2 and μ_r= 0.01, respectively, based on measurements in Refs. [61, 62].

Figure 28 depicts the fluid film thickness fields (top graphs) and pressure fields (bottom graphs) for the three TPTB cases analyzed. The regular (non-equalizing) TPTB (left

graphs) shows significant variations of fluid film thickness and pressure across the pads. The fluid film on pad ② has a minimum thickness h_{min} = 25.3 μm, roughly two and half times of that on pad ⑤ with h_{min} = 9.8 μm. Variations of pressure field magnitude across the pads are, however, more substantial; and such that the peak pressure on pad ⑤ (P_{Peak} = 11.3 MPa) is eight times of that on pad ② (P_{Peak} = 1.4 MPa). In Figure 28(b), depicting the ideal pad leveling system (disregarding friction forces), the fluid film thickness and pressure fields are nearly identical among the pads, h_{min} = 15 μm and P_{Peak} = 4.7 MPa. In Figure 28(c), as the analysis accounts for friction forces at the contact surfaces, differences still remain in the film thickness and pressure fields across the pads. These differences are, however, significantly smaller compared to those in the non-equalizing TPTB, i.e., the one without leveling plates, and where the pads' peak pressures range from 3.6 MPa to 5.8 MPa while the minimum film thickness in a pad varies between 17.1 μm and 13.5 μm.

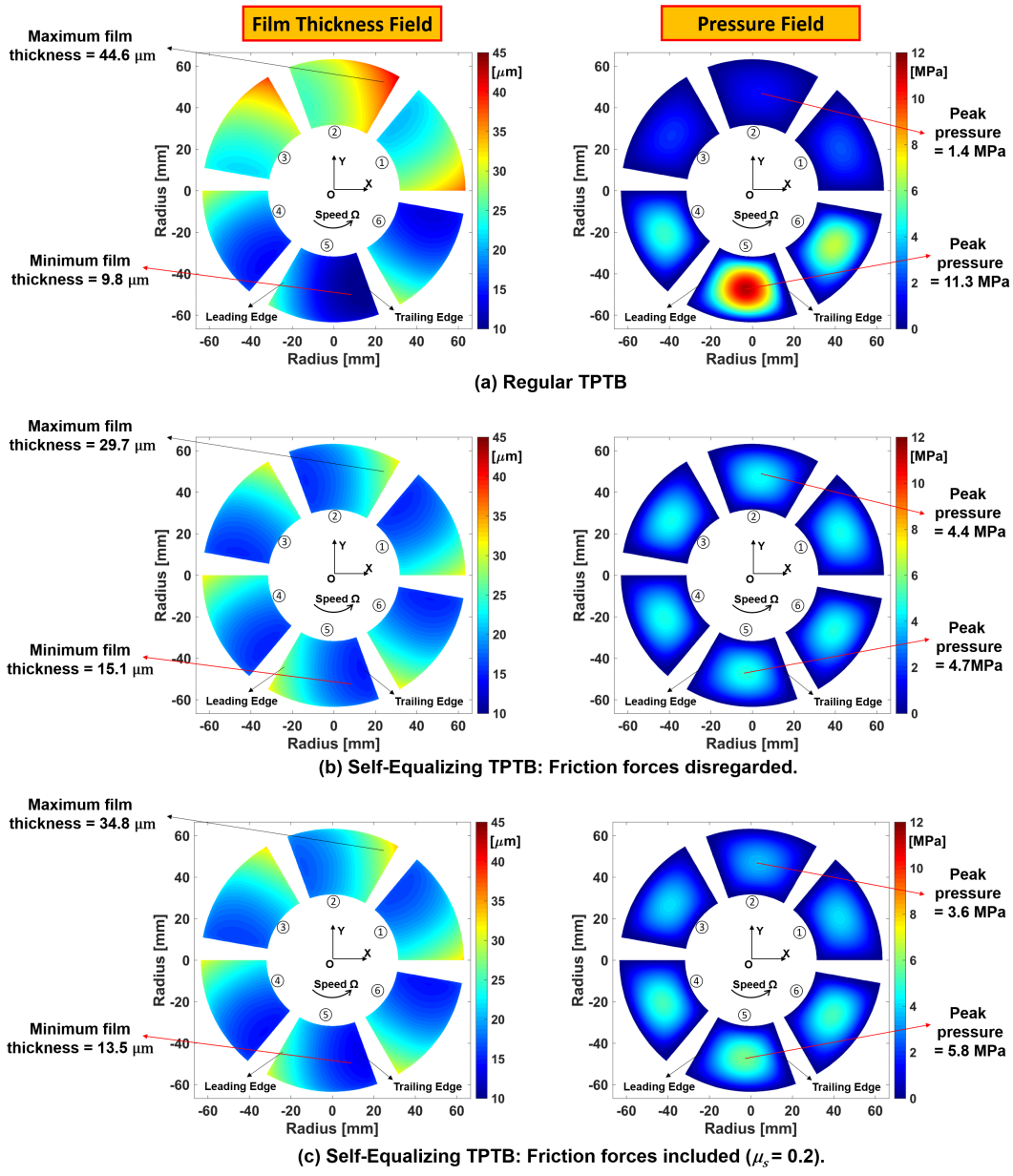

Fig. 28: Predicted fluid film thickness field (top) and pressure field (bottom) for a TPTB of (a) regular (non-equalizing) type, (b) self-equalizing type without including contact friction forces, and (c) self-equalizing type with contact friction forces (μ_s = 0.2 and μ_r = 0.01). Bearing operates with 0.01° thrust collar (static) misalignment. Rotor speed = 4 krpm, specific load per pad = 2 MPa. Reprinted with permission from [3].

Figure 29 depicts the predicted temperature fields: fluid film domain on the top graphs,

and in the bearing pads on the bottom graphs. The differences of both fluid film peak temperature and pad peak temperature are not significant even for the regular (non-equalizing) TPTB shown in the top graphs. The peak temperature on the non-equalizing bearing varies only 8.6° C, from a minimum of 70.3° C in pad ② to a maximum of 78.9° C in pad ⑤ . Differences in the pads' peak temperatures vanish for the ideal self-equalizing TPTB, case (b). Lastly, for case (c), the self-equalizing bearing with friction included shows a maximum difference of 5° C in the pads peak temperature.

For the three cases considered, Figure 30 shows the bearing pads' elastic deformation fields under a specific load/pad equal to 2.0 MPa. The top graphs show mechanical (pressure) deformations and the bottom graphs show thermal (temperature variations) deformations. Observe the mechanical deformations are negative and which means the pads displace away from the thrust collar to open the film thickness. On the other hand, the thermal deformations of the pad top surface are positive and push the pad closer to the thrust collar to reduce the fluid film thickness. Pressure induced deformations show significant differences across the bearing pads and rise up to 4 μm in magnitude for the non-equalizing TPTB in graph (a) where the pressure field concentrates on pad ⑤ . In case (b), disregarding the friction forces leads to nearly identical pressure deformations for all pads with a maximum of 1.6 μm. The realistic self-equalizing TPTB case (c), the one with friction at the contacts, shows a peak pressure deformation of 2.1 μm.

Pad thermal deformations follow the same trend as the pad temperature field depicted

in Figure 28, and with marginal variations across the pads. Thermal induced deformations are larger than pad mechanical deformations, hence contributing most to the overall deformation fields that adds both the pressure and temperature induced fields (not shown here).

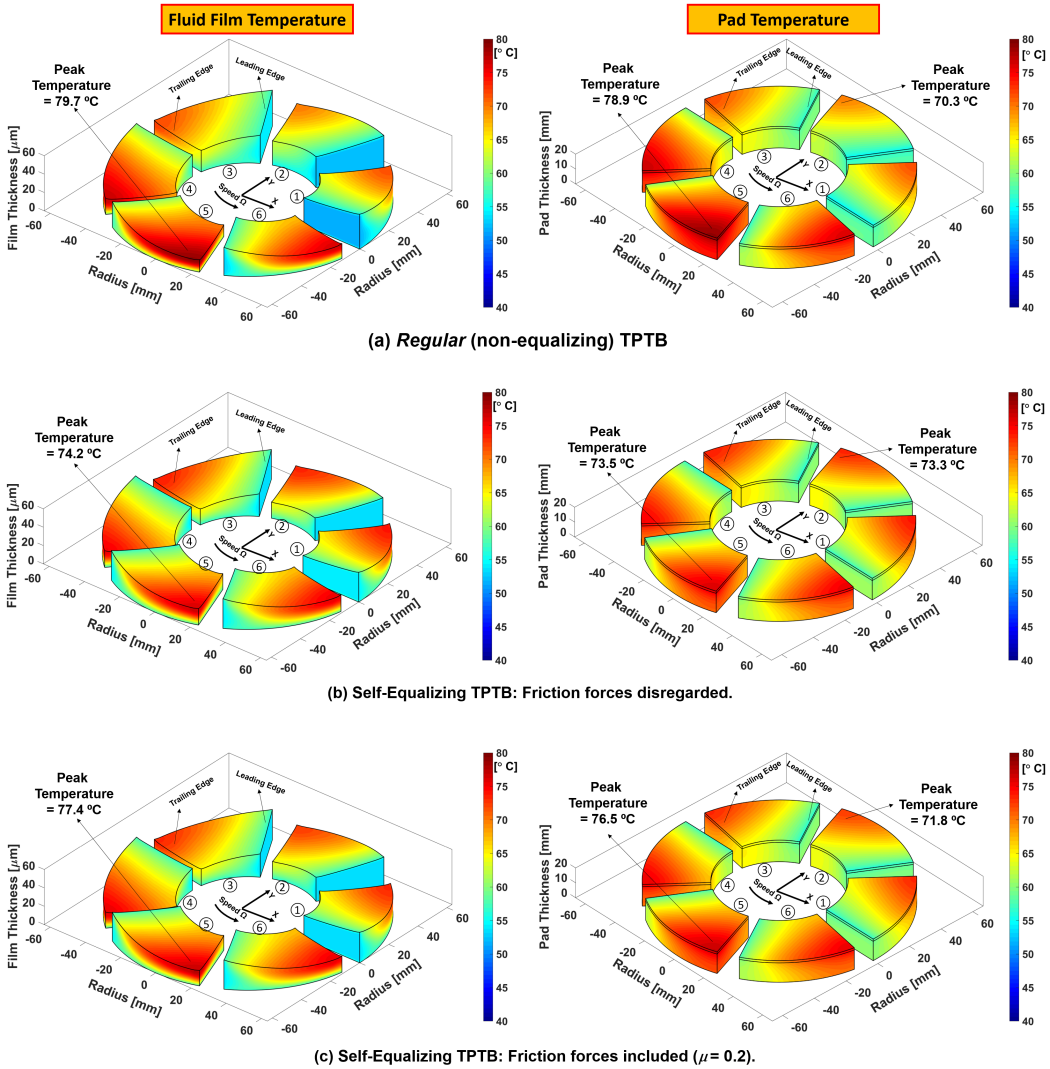

(a) *Regular* (non-equalizing) TPTB

(b) Self-Equalizing TPTB: Friction forces disregarded.

(c) Self-Equalizing TPTB: Friction forces included (μ = 0.2).

Fig. 29: Predicted fluid film temperature field (top) and pad temperature field (bottom) for a TPTB of (a) regular (non-equalizing) type, (b) self-equalizing type without including contact friction forces, and (c) self-equalizing type with contact friction forces (μ_s = 0.2 and μ_r = 0.01). Bearing operates with 0.01° thrust collar (static) misalignment. Rotor speed = 4 krpm, specific load per pad = 2 MPa. Reprinted with permission from [3].

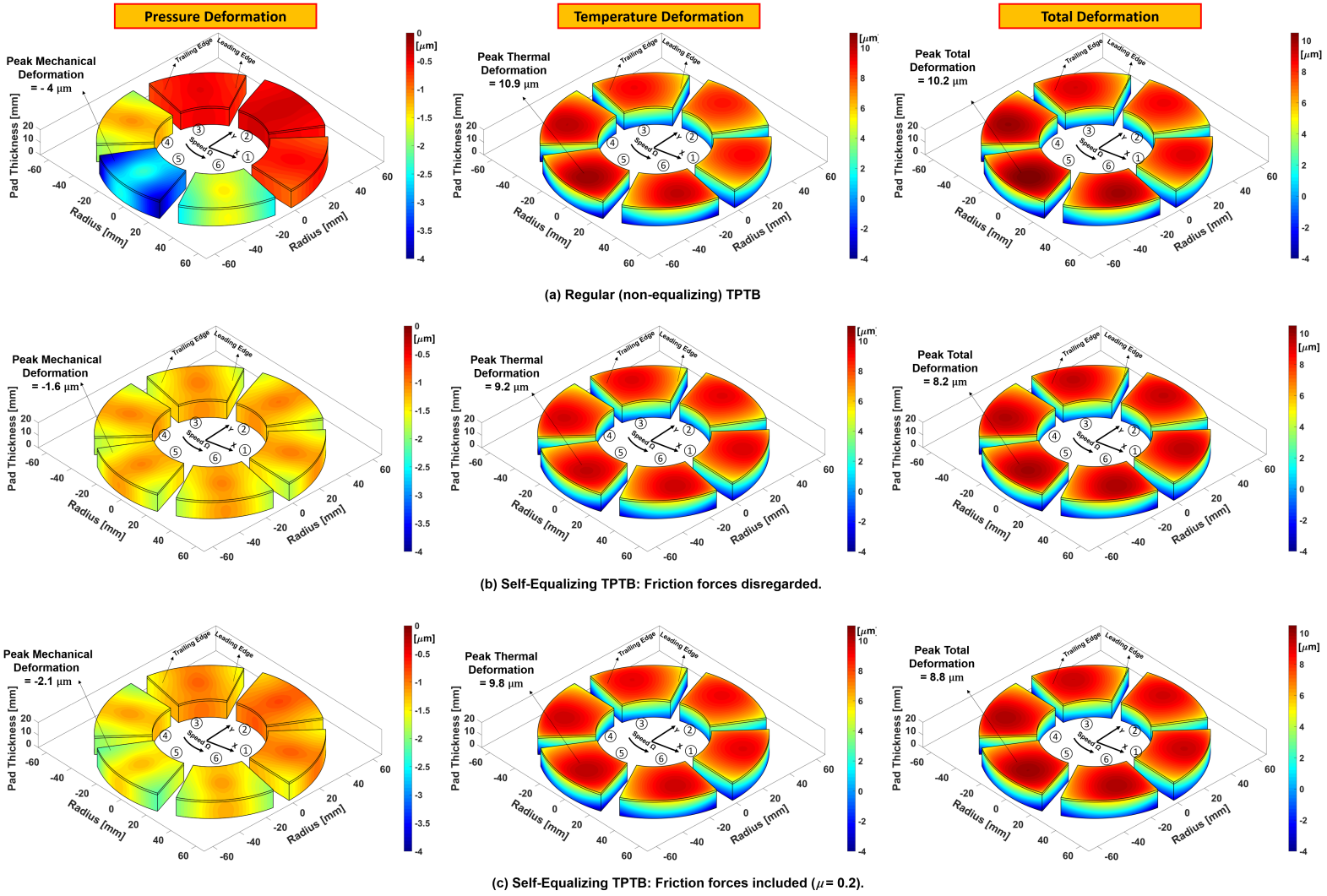

Fig. 30: Predicted pad mechanical deformation (top) and thermal induced deformation (bottom) for a TPTB of (a) regular (non-equalizing) type, (b) self-equalizing type without including contact friction forces, and (c) self-equalizing type with contact friction forces (μ_s = 0.2 and μ_r = 0.01). Bearing operates with 0.01 ° thrust collar (static) misalignment. Rotor speed = 4 krpm, specific load per pad = 2 MPa. Reprinted with permission from [3].

Figures 31 depicts (a) the predicted minimum film thickness and (b) peak pressure for the example self-equalizing TPTB operating with ϕ = 0.01° ($R_o\phi$= 11.25 μm) misalignment, versus sliding friction coefficient ranging from 0 to 0.3. Note that the friction forces acting at the contact points of the leveling plates restrict their tilting, i.e., they limit the desired action of the pad leveling system. The bearing operates at 4 krpm (26.8 m/s OD speed) and under light to heavy specific load per pad = 1.0 MPa, 2.0 MPa and 3.0 MPa. For reference, Figures 31 and 32 show with large symbols the predictions for an identical size non-equalizing TPTB. The symbols appear on the right vertical axis. The predictions should not be interpreted as a function of the friction coefficient.

In Figure 31 (a), as the coefficient of friction increases, the minimum film thickness of the pads in the self-equalizing bearing reduces toward that of the regular (non-equalizing) bearing. For the heavily loaded condition (3 MPa) with a null friction coefficient, the self-equalizing bearing shows a minimum film thickness of 12.4 μm, and which is 54% larger than that of the regular (non-equalizing) bearing. As the friction coefficient increases to 0.3, the aligning ability of the pad leveling system lessens and the bearing minimum film thickness reduces to 10.7 μm.

In Figure 31 (b), the pad leveling system proves effective to reduce the peak hydrodynamic pressure. For a 3.0 MPa load, the peak pressure (on the most loaded pad) in the regular TPTB is 19.3 MPa, whereas the bearing using the self-equalizing leveling system produces a peak pressure roughly half in magnitude. Increasing $\mu_s$from 0 to 0.3, as

expected, increases the pads' peak pressure.

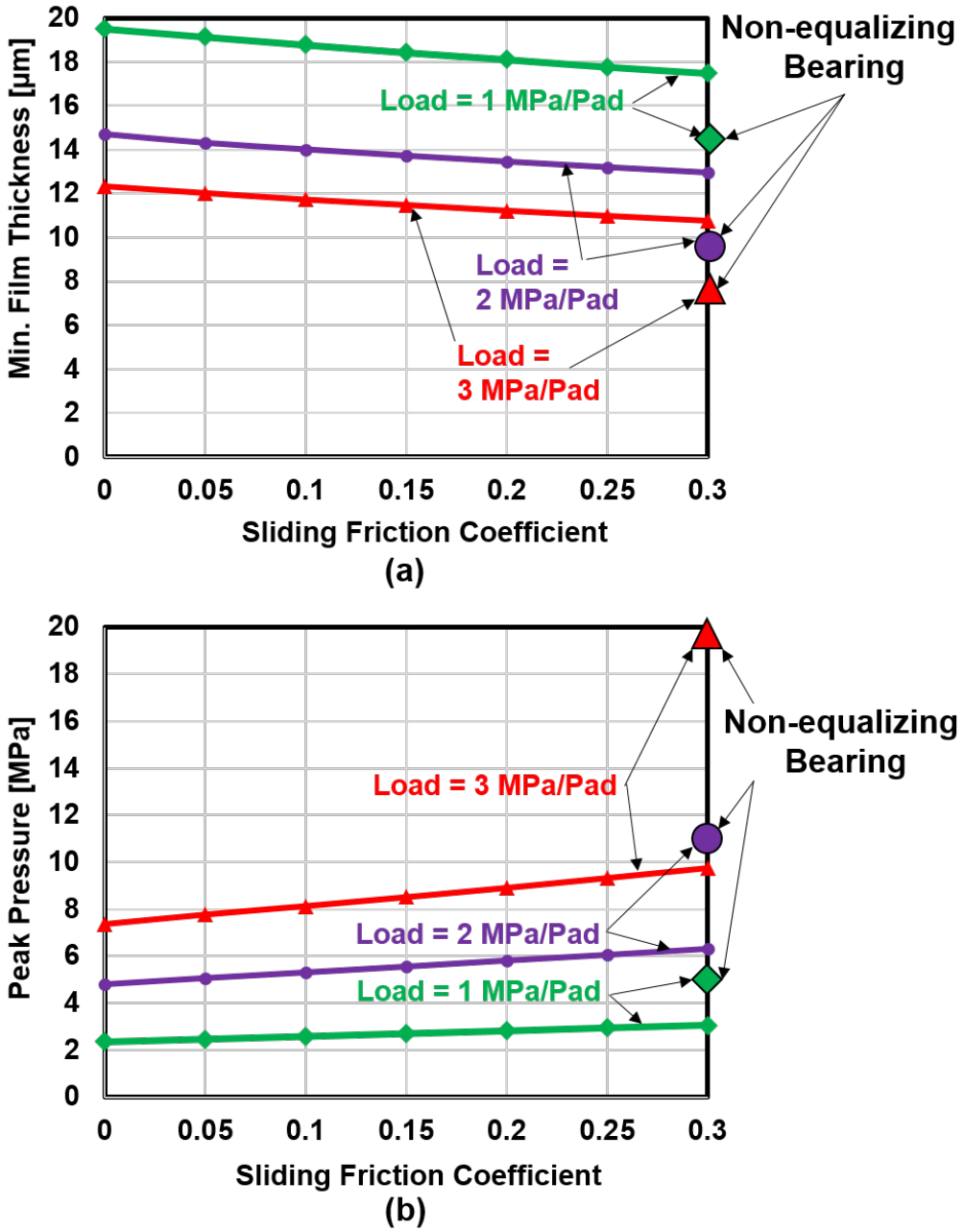

Fig. 31: Self-equalizing TPTB: predicted (a) minimum fluid film thickness and (b) peak pressure vs. sliding friction coefficient and for applied load= 1 MPa to 3 MPa per pad. Bearing operates with 0.01° thrust collar (static) misalignment. Rotor speed = 4 krpm. Reprinted with permission from [3].

Figure 32 shows the predicted maximum Hertz contact pressure versus μ_s. The bearing operates at 4 krpm rotor speed with $\phi = 0.01°$ thrust collar misalignment. As the pad specific load triples from 1.0 MPa to 3.0 MPa, the maximum contact pressure shows a roughly 80% increase, from less than 600 MPa to more than 900 MPa. Changes of the peak contact pressure versus friction coefficient are small though increasing.

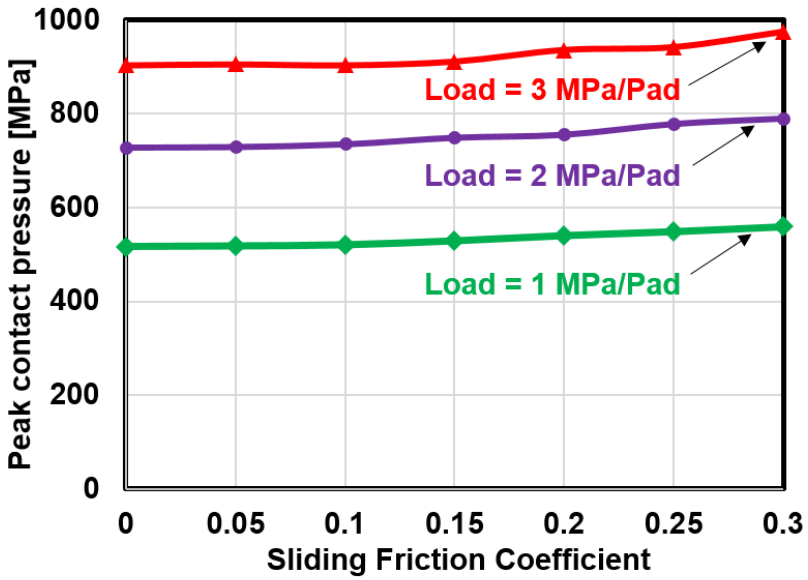

Fig. 32: Self-equalizing TPTB: Maximum (Hertzian) contact pressure vs. sliding friction coefficient and for applied load= 1 MPa to 3 MPa per pad. Bearing operates with 0.01° thrust collar (static) misalignment. Rotor speed = 4 krpm. Reprinted with permission from [3].

5 A REDUCED FLOW MODEL FOR TILTING PAD THRUST BEARINGS

This chapter describes a model for either starved flow or over-flooded flow TPTBs and its implementation into the previously developed TEHD model to deliver load performance predictions vs. supply flow rate. The following describes the flow starvation model, compares pad subsurface and discharge flow temperature rise predictions vs. measurements, and further details load performance predictions for an example starved flow TPTB with evacuated-ends.

5.1 DESCRIPTION OF THE ANALYSIS FOR FLOW STARVATION

Bearing load performance substantially depends on the temperature of the flow entering its pads, and which is determined by the flow thermal mixing in the bearing grooves. The conventional hot oil carry-over model [47] described in Chapter 3 (Eqn. (8)) uses a hot oil carry-over coefficient to determine the temperature of the flow entering the downstream pad. The hot oil carry-over coefficient is an empirical parameter that varies with the bearing operating condition, e.g. load, speed, and, and supply flow rate. [25, 47]. Thus, to predict the load performance of a bearing operating with either an over-flooded flow condition or a starved flow condition, the respective magnitude of the hot oil carry-over coefficient should be estimated through experiments, i.e. by measuring the pad temperature or fluid film thickness.

In addition, thrust bearings operate with either end-seals to limit the oil leakage and hold the oil inside the bearing housing or with evacuated-ends in which the hot oil leaving the pad at its ID and OD immediately leaves the bearing. In bearings with end-seals, the churning flow in th bearing housing mixes with flow in the feed grooves to enter the down-stream pad leading edge. Hence, under an identical operating condition, the temperature of the flow entering the pads in a bearing with end-seals varies from that in a bearing of the same size but with evacuated-ends.

The hot oil carry-over model also does not account for the churning oil in the grooves and thus comes short to differentiate between bearings with end-seals vs. those with evacuated-ends.

The following analysis builds a thermal mixing model for the flow inside a feed groove that accounts for the supply flow rate and differentiates between bearings with end-seals and those with evacuated-ends.

5.1.1 Groove Thermal Mixing Model for Bearings with End-Seals

Thrust bearings with end-seals limit the oil leakage from the sides, thus the oil trapped inside the bearing housing churns to produce a mechanical drag power loss. The hot oil churning in the bearing housing also mixes with the supply flow and enters the fluid film through the pad leading edge. As a result, the temperature of the flow entering the film increases to reduce the lubricant viscosity and that causes a reduction in the fluid film

thickness.

Figure 33 shows a schematic view of the flow into and out of a feed groove in a thrust bearing with end-seals. Observe the end-seals installed with a small clearance (< 0.1 mm, see Ref. [66]) from the collar at both the bearing ID and OD to limit the oil leakage. The oil churns within the gap between the pads and the end-seals. The bearing housing has a collection of oil discharge holes[10] at the OD to let the oil leaves the bearing while a small fraction of the oil still leaves the bearing through the end-seals clearance, mostly through the OD [33].

A hot stream of oil enters the groove from the upstream pad trailing edge (Q_{TE}) to mix with a cold supply flow (Q_{Su}) and leaves the groove to enter the downstream pad leading edge (Q_{LE}). Further, a feed groove may also receive a back flow (Q_{BF}) leaving the downstream pad through its leading edge due to a large pressure gradient at the pad leading edge.

[10]Note the configuration for oil discharge varies from one bearing design to another. For instance, the test thrust bearing in Ref.[33] only has a single hole at the OD of the bearing housing to let the oil discharge. The thrust bearing in Ref. [67], however, has multiple oil discharge holes similarly located at the OD of the bearing housing.

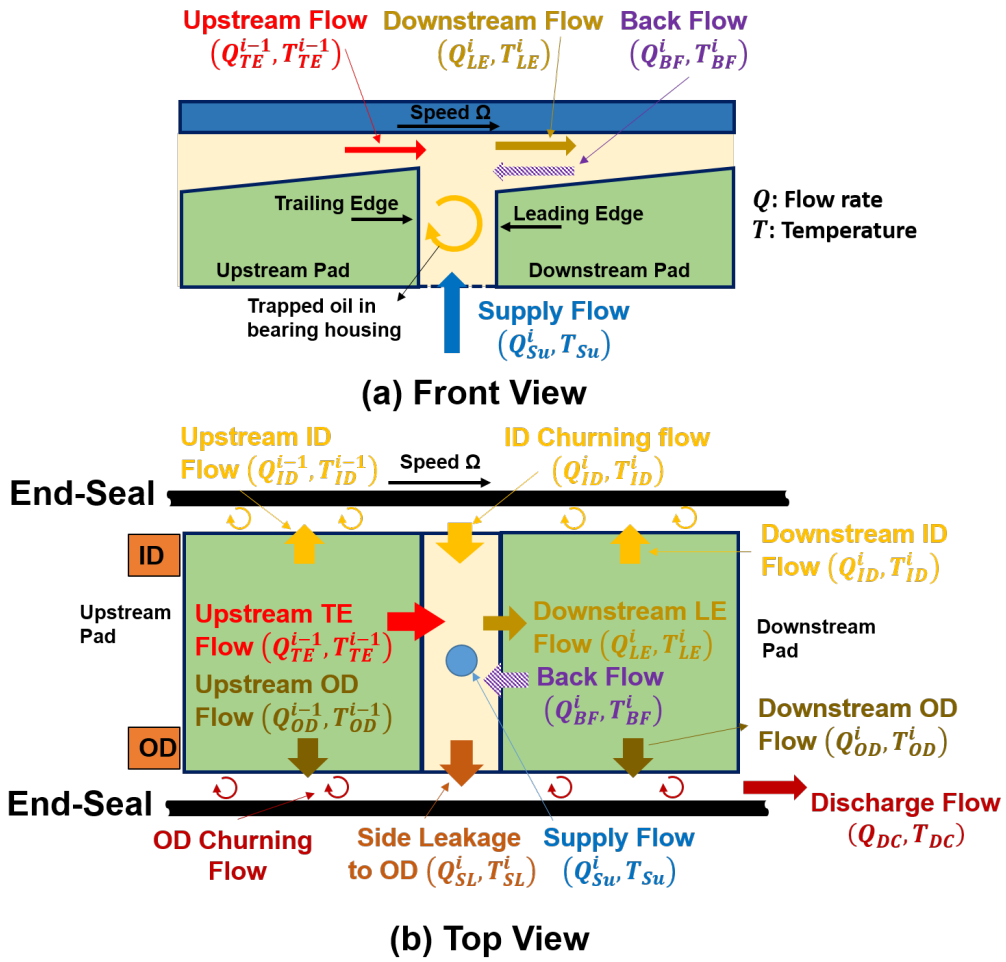

Fig. 33: Schematic (a) front view and (b) top view of the flows into and out of a feed groove and pads in a TPTB with end-seals. $i-1$ and i refer to the upstream and downstream pads, respectively.

Recall from Chapter 3 that the combined solution of a general Reynolds Eqn. (2) and thermal energy transport Eqn. (4) produces a 3-dimensional (3D) temperature field ($T_{(r,\theta,z)}$) and flow velocity fields ((U, V, W) in the radial, circumferential, and axial directions, respectively) for the film gap. The global cylindrical system has its circumferential axis along the direction of the speed, i.e. from pad leading edge toward the pad trailing

edge. The flow velocity field follows from Eqn. (5) in Chapter 3 with respect to the global coordinate system, i.e. the fluid velocity is positive when the flow moves along the positive direction of the global coordinate system and vise versa.

At the leading edge of pad i^{th}, the flow enters the film gap where the circumferential flow velocity is positive ($V_{(r,\theta_{LE},z)} > 0$). Thus, the flow rate entering a pad through its leading edge is Q_{LE} is,

$$Q^i_{LE} = \int_{R_i}^{R_o} \int_{z=0}^{z=h^i_{(r,\theta_{LE})}} (V^i_{(r,\theta_{LE},z)}, \text{ if } \quad V^i_{(r,\theta_{LE},z)} > 0) dr dz \qquad i = 1, ..., N_P \tag{33}$$

On the other hand, a back flow my occur since, over portions of the film, the pressure gradient pushes flow out of the leading edge and into the groove. The back flow rate Q_{BF} and back flow temperature T_{BF} are,

$$Q^i_{BF} = \int_{R_i}^{R_o} \int_{z=0}^{z=h^i_{(r,\theta_{LE})}} (|V^i_{(r,\theta_{LE},z)}|, \text{ if } \quad V^i_{(r,\theta_{LE},z)} < 0) dz dr \tag{34a}$$

$$T^i_{BF} = \frac{\int_{R_i}^{R_o} \int_{z=0}^{z=h^i_{(r,\theta_{LE})}} (|V^i_{(r,\theta_{LE},z)}| T_{(r,\theta_{LE},z)}, \text{ if } \quad V^i_{(r,\theta_{LE},z)} < 0) dz dr}{Q_{BF}} \tag{34b}$$

Similarly, the flow Q_{TE} with temperature T_{TE} leaves the pad through its trailing edge, i.e.

$$Q^i_{TE} = \int_{R_i}^{R_o} \int_{z=0}^{z=h^i_{(r,\theta_{TE})}} V^i_{(r,\theta_{TE},z)} dz dr \tag{35a}$$

$$T^i_{TE} = \frac{\int_{R_i}^{R_o} \int_{z=0}^{z=h^i_{(r,\theta_{TE})}} V^i_{(r,\theta_{TE},z)} T^i_{(r,\theta_{TE},z)} dz dr}{Q^i_{TE}} \tag{35b}$$

Note the flow circumferential velocity at the pad trailing edge is always positive since both the shear and pressure induced flows move in the positive direction, see Eqn. (5).

The film side leakage flow rate Q_{ID} and temperature T_{ID} to the pad ID yield from an integration of the film radial velocity field $U_{(R_i,\theta,z)}$ along the pad ID edge, i.e.,

$$Q^i_{ID} = \int_{\theta_{LE}}^{\theta_{TE}} \int_{z=0}^{z=h^i_{(R_i,\theta)}} |U^i_{(R_i,\theta,z)}| r dz d\theta \tag{36a}$$

$$T^i_{ID} = \frac{\int_{\theta_{LE}}^{\theta_{TE}} \int_{z=0}^{z=h^i_{(R_i,\theta)}} |U^i_{(R_i,\theta,z)}| T^i_{(R_i,\theta,z)} r dz d\theta}{Q^i_{ID}} \tag{36b}$$

Likewise, the side leakage flow rate Q_{OD} and temperature T_{OD} to the OD are,

$$Q^i_{OD} = \int_{\theta_{LE}}^{\theta_{TE}} \int_{z=0}^{z=h^i_{(R_o,\theta)}} U^i_{(R_o,\theta,z)} r d\theta dz \tag{37a}$$

$$T^i_{OD} = \frac{\int_{\theta_{LE}}^{\theta_{TE}} \int_{z=0}^{z=h^i_{(R_o,\theta)}} U^i_{(R_o,\theta,z)} T^i_{(R_o,\theta,z)} r d\theta dz}{Q^i_{OD}} \tag{37b}$$

Recall the fluid radial velocity is positive at the OD but negative at the ID.

Wasilczuk and Rotta [31] built a 3D computational fluid dynamics (CFD) model of the flow in a feed groove for thrust bearings with end-seals. Their study considered both flooded lubrication systems and direct lubrication systems. The CFD results show a centrifugal force induced by the thrust collar rotation highly affects the motion of the fluid in the groove to develop a dominant radial velocity field along the positive direction over the entire flow domain. That indicates the flow in thrust bearing feed groove can only move

from the groove ID toward the groove OD.

In another study, Bielec and Leopard [33] also experimentally investigated the fluid motion inside the groove in a TPTB. The authors built a test rig with feed ports placed at the bearing OD. They observed the oil supplied to the bearing OD does not travel toward the ID due to a centrifugal force induced by thrust collar rotation. As a consequent, areas near the pad ID remained denuded of oil while the majority of oil supplied into the bearing churned at the OD until exiting the bearing to return to the sump. Accordingly, the findings of Bielec and Leopard's work [33] confirm the results of CFD analysis in Wasilczuk and Rotta [31] that the flow inside a thrust bearing groove only moves from ID toward OD.

Consistent with the findings above, Glavatskih et al. [26] developed a thermal mixing model for the flow inside a thrust bearing groove. For bearings with end-seals, the model assumes the flow exiting a pad from the ID (Q_{ID}) churns inside the bearing housing (around and underneath the pad) and reaches the downstream pad's groove to enter the fluid film again. Meanwhile any additional flow inside the groove is pushed to the bearing OD as a side leakage (Q_{SL}) to mix with the flow leaving the pads at the OD (Q_{OD}) and churns until eventually returning to the sump, see Figure 33.

The work here adopts the groove thermal mixing model introduced by Glavatskih et al. in [26][11] to determine the temperature of the flow entering the pad. The flow continuity equation balances the flows entering a groove with the flows leaving the groove. The flow

[11] Glavatskih et al. [26] validates the model predictions of film thickness, pad temperature rise and drag power loss vs. measurements for a six-pad TPTB operating under specific load per pad = 0.5-2.0 MPa and at rotor speed = 1.5-3.0 krpm.

continuity equation in the groove upstream of the i^{th} pad is,

$$Q^i_{SL} = Q^i_{Su} + Q^{i-1}_{TE} + Q^{i-1}_{ID} + Q^i_{BF} - Q^i_{LE} \qquad i = 1, ..., N_P \tag{38}$$

where Q_{SL} is the groove side leakage displaced to the OD and only occurs if the oil flow into the bearing groove exceeds the flow Q_{LE} going to the downstream pad.

Therefore, the nominal supply flow rate Q^i_{Nm} required to fully wet the pad is,

$$Q^i_{Nm} = Q^i_{LE} - \{Q^{i-1}_{TE} + Q^{i-1}_{ID} + Q^i_{BF}\} \tag{39}$$

As Figure 33 shows, the flow exiting a flooded bearing (with end-seals) is a mixture of the flow leaving the pads at their OD and the grooves' side leakage. The discharge flow Q_{DC} and discharge flow temperature T_{DC} are,

$$Q_{DC} = \sum_{i=1}^{N_{Pad}} Q^i_{SL} + Q^i_{OD} \tag{40a}$$

$$T_{DC} = \frac{\sum_{i=1}^{N_{Pad}} Q^i_{SL} T^i_{SL} + Q^i_{OD} T^i_{OD}}{Q_{DC}} \tag{40b}$$

Note substituting the side leakage flow Eqn.(38) into the discharge flow Eqn.(40.a) confirms the conservation of the flow into and out of a bearing, i.e. $Q_{DC} = Q_{Su}$.

Fluid motion transports thermal energy (heat) inside and outside of a bearing feed groove, i.e., an advection heat transfer mechanism. The heat transported by flow Q from

one location to another depends on the temperature difference ΔT as well as the lubricant density ρ and specific heat capacity c_P,

$$\Phi = \rho c_P Q \Delta T \tag{41}$$

Accordingly, heat streams into the groove with upstream pad leading edge flow ($\Phi_{TE\to Gr}$), the ID churning oil that enters the groove ($\Phi_{ID\to Gr}$), the supply flow ($\Phi_{Su\to Gr}$), and the downstream pad back flow ($\Phi_{BF\to Gr}$). The total heat into the groove is,

$$\begin{aligned}\Phi^i_{in} &= \Phi^i_{TE\to Gr} + \Phi^i_{ID\to Gr} + \Phi^i_{Su\to Gr} + \Phi^i_{BF\to Gr} \\ &= \rho c_P \left(Q^{i-1}_{TE} T^{i-1}_{TE} + Q^{i-1}_{ID} T^{i-1}_{ID} + Q^i_{Su} T_{Su} + Q^i_{BF} T^i_{BF}\right)\end{aligned} \tag{42}$$

At the same time, heat leaves the groove with the downstream pad leading edge flow ($\Phi_{Gr\to LE}$) and the side leakage flow ($\Phi_{Gr\to SL}$). The groove thermal mixing model in Glavatskih et al. [26] (Eqns.(45) and (38)) assumes the flow inside a groove is well mixed, thus the temperature of the flow that enters the downstream pad leading edge (T_{LE}) equals to the temperature of the flow leaving the groove through side leakage. Thus, the heat flowing out of a feed groove is,

$$\begin{aligned}\Phi^i_{out} &= \Phi^i_{Gr\to LE} + \Phi^i_{Gr\to SL} \\ &= \rho c_P \left(Q^i_{LE} + Q^i_{SL}\right) T^i_{LE}\end{aligned} \tag{43}$$

Conservation of energy states that the thermal energy (heat) transported into a bearing groove equals the heat carried out of the groove. A steady state thermal energy conservation equation for a feed groove is,

$$\Phi^i_{in} = \Phi^i_{out} \tag{44a}$$

$$\rho c_P \left(Q^{i-1}_{TE} T^{i-1}_{TE} + Q^{i-1}_{ID} T^{i-1}_{ID} + Q^i_{Su} T_{Su} + Q^i_{BF} T^i_{BF}\right) = \rho c_P \left(Q^i_{LE} + Q^i_{SL}\right) T^i_{LE} \tag{44b}$$

Note this equation does not account for heat accumulation or heat conduction into the thrust collar or bearing housing. Thus, the temperature T_{LE} of the flow Q_{LE} entering the pad leading edge follows as,

$$T^i_{LE} = \frac{Q^i_{Su} T_{Su} + Q^{i-1}_{TE} T^{i-1}_{TE} + Q^{i-1}_{ID} T^{i-1}_{ID} + Q^i_{BF} T^i_{BF}}{Q^i_{LE} + Q^i_{SL}} \tag{45}$$

Per the thermal energy transport Eqn.(43) and energy conservation Eqn. (44), the fraction of the heat from the upstream pad trailing edge and ID that is carried to the downstream pad leading edge equals the ratio of the downstream pad leading edge flow Q_{LE} over the sum of all the flow that leaves the groove,

$$\frac{\Phi^i_{Gr\to LE}}{\Phi^i_{in}} = \frac{\Phi^i_{Gr\to LE}}{\Phi^i_{out}} = \frac{Q^i_{LE} T^i_{LE}}{\left(Q^i_{LE} + Q^i_{SL}\right) T^i_{LE}} = \frac{Q^i_{LE}}{Q^i_{LE} + Q^i_{SL}} \tag{46}$$

while the rest of the energy leaves the groove with the side leakage flow. Increasing the

supply flow rate produces a larger side leakage flow (see Eqn.(38)) to reduce the fraction of the heat (leaving upstream pad) that is carried to the downstream pad. On the other hand, if the side leakage flow is null (starved flow condition), all the heat from the upstream pad flows into the downstream pad leading edge.

The model, however, disregards the heat conducted into the bearing housing and the thrust collar.

5.1.2 Groove Thermal Mixing Model for Bearings with Evacuated-Ends (Without End-Seals)

Bearings with evacuated-ends do not trap the oil inside the bearing housing and the oil exiting a pad at its ID (Q_{ID}) and its OD (Q_{OD}) joins the groove side leakage flow Q_{SL} to leave the bearing and returns to the sump. Compared to bearings with end seals, evacuated-ends bearings operate with a lesser drag power loss, a lower pad temperature, and a larger fluid film thickness; though requiring a larger supply flow rate, see measurements in Ref.[68]. In most cases, evacuation of a bearing is effectively achieved through the absence of end-seals or by using end-seals with a large clearance ($\sim$ 3-5 mm). Then, the oil is thrown out of the bearing housing with no resistance as the thrust collar turns [66, 68]. The bearing housing cannot be pressurized in bearings with evacuated-ends.

Figure 34 shows a schematic view of the flow inside a bearing with evacuated-ends. Observe the oil does not churn inside the bearing housing and the feed groove only receives

oil from the upstream pad trailing edge flow Q_{TE} and the supply flow Q_{Su}.

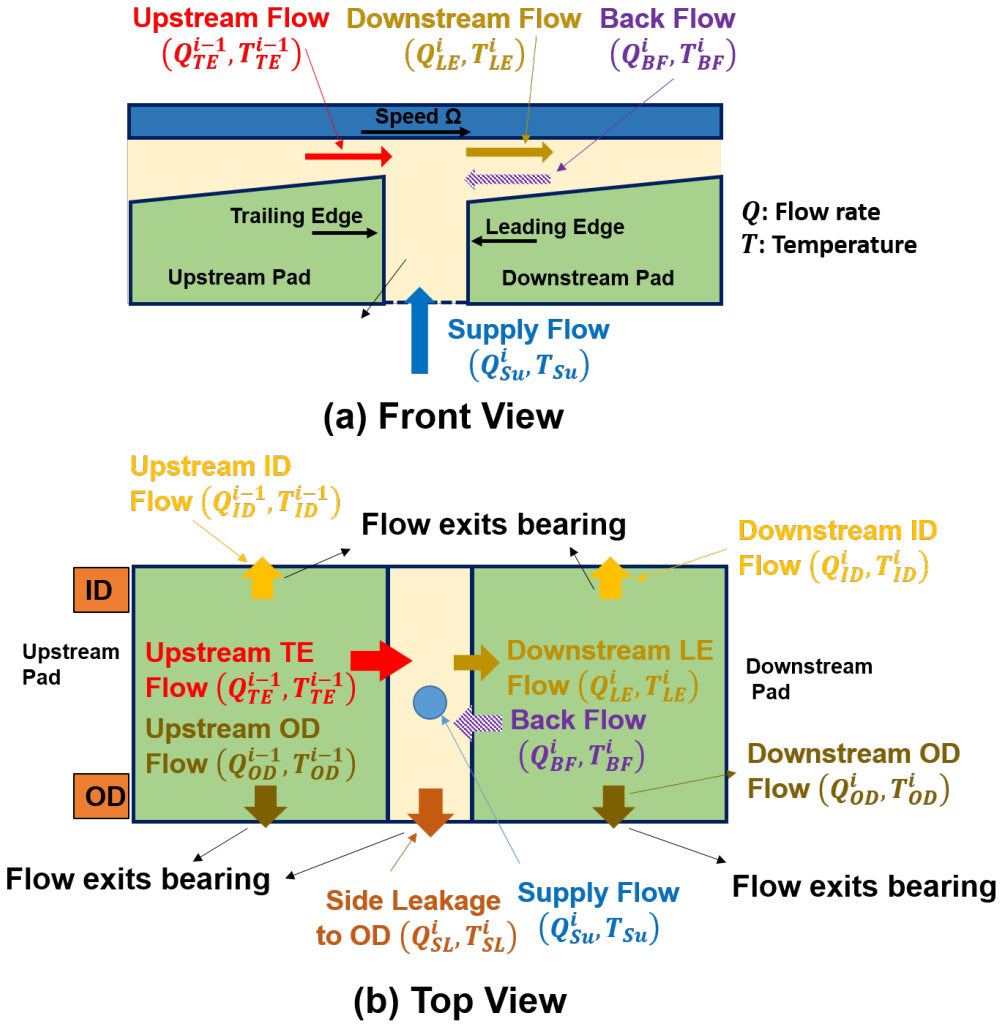

Fig. 34: Schematic (a) front view and (b) top view of the flows into and out of a feed groove and pads in a TPTB with evacuated-ends. $i-1$ and i refer to the upstream pad and downstream pad, respectively.

In the absence of any churning oil, the flow continuity equation for a groove in a bearing with evacuated-ends is

$$Q_{SL}^{i} = Q_{Su}^{i} + Q_{TE}^{i-1} + Q_{BF}^{i} - Q_{LE}^{i} \qquad i = 1, ..., N_P \tag{47}$$

Consequently, the temperature T_{LE} of the flow entering the pad leading edge is

$$T^i_{LE} = \frac{Q^i_{Su} T_{Su} + Q^{i-1}_{TE} T^{i-1}_{TE} + Q^i_{BF} T^i_{BF}}{Q^i_{LE} + Q^i_{SL}} \tag{48}$$

Bearings with evacuated-ends demand a larger nominal supply flow rate than that in bearings with end seals (Eqn.(39)) as the flow from the upstream pad ID is evacuated out of the bearing and doesn't reach to the downstream pad groove. The nominal flow rate for a bearing with evacuated-end is,

$$Q^i_{Nm} = Q^i_{LE} - \{Q^{i-1}_{TE} + Q^i_{BF}\} \tag{49}$$

The discharge flow in an evacuated-ends bearing is a mixture of the flow leaving the pads at OD and ID and the grooves' side leakage flow. Thus, the discharge flow Q_{DC} and discharge flow temperature T_{DC} are

$$Q_{DC} = \sum_{i=1}^{N_{Pad}} Q^i_{SL} + Q^i_{OD} + Q^i_{ID} \tag{50a}$$

$$T_{DC} = \frac{\sum_{i=1}^{N_{Pad}} Q^i_{SL} T^i_{SL} + Q^i_{OD} T^i_{OD} + Q^i_{ID} T^i_{ID}}{Q_{DC}} \tag{50b}$$

5.1.3 A Flow Starvation Model for TBs

The work here further implements the flow starvation model in San Andrés et al. [15] to quantify the effect of flow rate on the performance of TPTBs. In a flooded flow con-

dition, the supply flow rate mixed with the flow from the upstream pad trailing edge is enough to fully fill in the gap region between the thrust collar and bearing pads. Any additional flow is quickly forced out through the bearing OD and which produces churning power loss if the bearing is not evacuated.

If the supply flow is less than the one needed, the bearing pads starve. Figure 35 portrays a schematic view of a bearing pad operating under flow starvation. Q_{TE} is the flow leaving an upstream pad that is carried by the rotating collar, while Q_{Su} is the externally supplied flow that is not enough to fill in the gap at the pad leading edge. The mixing of both flows occurs at a distance inside the pad. The arc length defined as effective is the region where a hydrodynamic pressure builds to sustain an applied load. A flow starved pad has a shorter effective arc length than the actual physical length of a pad, thus resulting in a smaller effective pivot offset for the lubricated part of the pad.

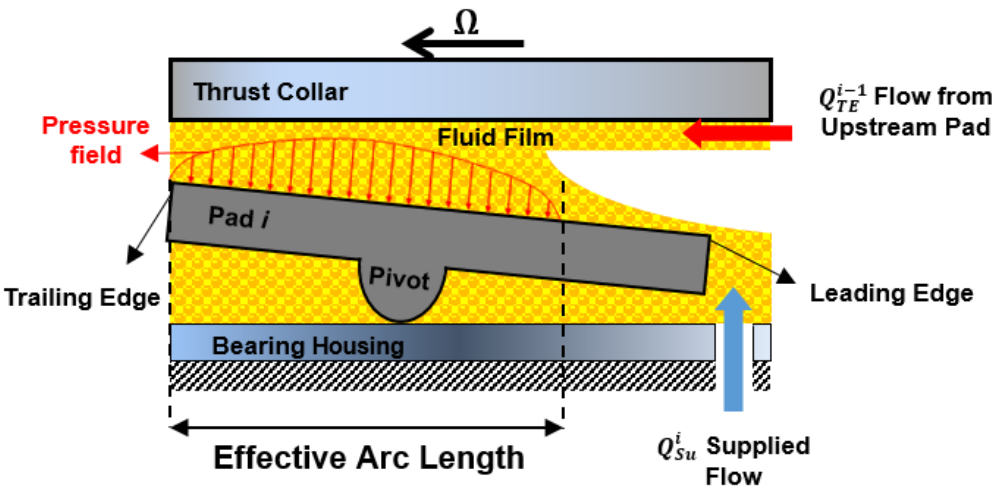

Fig. 35: Idealized view of a flow starvation in a pad. Q_{Su} and Q_{TE} are the (cold) supply flow and the (hot) flow from an upstream pad.

A reduction in supply flow rate initially results in a decrease in the groove side leakage (see Eqns. (38) and (47)) up to a point that side leakage becomes null. A further reduction in supply flow, therefore, decreases the downstream pad leading edge flow to produce a starved flow condition. The inlet flow rate Q_{LE} into a pad in a bearing with end-seals follows from Eqn. (38), i.e.

$$Q_{SL}^{i} = 0, \quad \rightarrow \quad Q_{LE}^{i} = Q_{Su}^{i} + Q_{TE}^{i-1} + Q_{ID}^{i-1} + Q_{BF}^{i} \tag{51}$$

and the inlet flow temperature T_{LE} in Eqn. (45) becomes,

$$T_{LE}^{i} = \frac{Q_{Su}^{i} T_{Su} + Q_{TE}^{i-1} T_{TE}^{i-1} + Q_{ID}^{i-1} T_{ID}^{i-1} + Q_{BF}^{i-1} T_{BF}^{i-1}}{Q_{LE}^{i}} \tag{52}$$

Similarly, the inlet flow rate Q^i_{LE} and inlet flow temperature Q^i_{LE} for a starved flow bearing with evacuated-ends are (from Eqns. (47) and Eqn. (48))

$$Q^i_{SL} = 0, \quad \rightarrow \quad Q^i_{LE} = Q^i_{Su} + Q^{i-1}_{TE} + Q^i_{BF} \tag{53}$$

and the leading edge flow temperature is (from Eqn. (48)),

$$T^i_{LE} = \frac{Q^i_{Su} T_{Su} + Q^{i-1}_{TE} T^{i-1}_{TE} + Q^{i-1}_{BF} T^{i-1}_{BF}}{Q^i_{LE}} \tag{54}$$

The groove thermal model in Ref.[26] (Eqns. (51) and (52) for bearings with end seals and Eqns. (53) and (54) for those with evacuated-ends) assumes the heat from the upstream pad trailing edge is entirely[12] carried into the downstream pad leading edge when the bearing starves, i.e., $Q^i_{SL} = 0$. Other works in Refs.[45, 68] also utilize the same assumption when modeling the load performance of starved flow bearings. Further, measurements in Heshmat and Gorski [69] also support this assumption and shows the groove ability to redirect the upstream pad flow (heat) out of the bearing declines as the supply flow rate decreases. Heshmat and Gorski [69] concluded that all the heat from the upstream pad trailing edge goes into the downstream pad leading edge when the bearing starves.

During the solution process, the analysis initially predicts the bearing performance

[12]Note this assumption is likely acceptable when heat conduction into both the bearing housing and the thrust collar is negligible.

by first considering pressure boundary conditions (not flow) to determine the nominal (demand or supply) flow rate, the one needed to wet all the pads in a whole bearing. Over flooded operation ensues when the actual supply flow rate exceeds the nominal flow; and here the analysis assumes the extra flow simply displaces toward the bearing OD to return to sump flow. Note an increase in supply flow rate lowers the pad inlet flow temperature while the groove side leakage increases, see the thermal energy balance Eqns. in a feed groove (Eqn.(45) for sealed ends and Eqn. (48) for evacuated ends bearings). On the other hand, a starved flow condition ensues when the actual supply flow rate is lesser than the nominal. Here the analysis iteratively reduces the film arc length until the supply flow rate is enough to fully fill the film gap. The pressure boundary condition is set to ambient pressure at the new found film inception location.

The present analysis includes two groove oil thermal mixing models: the hot oil carry-over model (detailed in Chapter 2) and the model adopted from Ref. [26]. The hot oil carry-over model is used in Chapters 3 and 4 for operation with a flooded flow condition when the groove thermal mixing coefficient λ_{mix} is determined through experiments[13]. Whereas, the groove thermal mixing model from Ref.[26] is used here for operations with either starved flow or an over-flooded flow condition.

[13] As Ref. [26] describes, when load performance measurements (pad temperature or fluid film thickness) are available for a bearing, a trial and error process produces the groove thermal mixing coefficient λ_{mix} that produces predictions in close agreement with the measurement.

5.2 VALIDATION OF FLOW STARVATION ANALYSIS

Mikula [57] and Capitao et al. [40] measure pad subsurface temperature rises and oil discharge temperature rise in a centrally pivoted tilting pad thrust bearing (TPTB) operating under three supply flow rates: the manufacturer recommended flow rate, 50% higher and 50% lesser than recommended rate.

This work uses the configuration of the test TPTB in Refs. [40, 57] to evaluate the effect of supply flow rate on the TB load performance. Table 6 highlights the bearing configuration, lubricant properties, and operating conditions. The bearing has eight pads with ID=133 mm, OD=267 mm and 38° pad arc length. The bearing operates at 4 krpm (ΩR_o = 54m/s) and 10 krpm (ΩR_o = 135m/s) and under a specific load/pad ranging from 0.7 MPa to 3.5 MPa. The test bearing is lubricated with a flooded lubrication system and has end-seals to hold the oil inside the bearing housing.

Figure 36 depicts the supply flow rate recommended by the bearing manufacturer[14] and predicted nominal flow rate (Eqn. (39)) for operation at 4 krpm and 10 krpm vs. specific load per pad [57]. The recommended flow increases with load from 34 LPM to 55 LPM at 4 krpm and from 83 LPM to 131 LPM at 10 krpm. Opposed to the recommended flow rate, the predicted nominal flow rate required to fully fill the pads' films decreases from 34 LPM to 10 LPM at 4 krpm, and from 58 LPM to 38 LPM at 10 krpm as the specific load increases from 0.7 MPa/pad to 3.4 MPa/pad. Figure 36 also shows the nominal flow

[14]Note the recommended supply flow rate is taken from Ref.[16] published in 1979. The manufacturer may no longer recommend the said flow rates for their bearings.

rate (Eqn. (49)) predicted for an identical bearing configuration but with evacuated-ends. The nominal flow rate supplied to the bearing is roughly 30% larger with evacuated-ends than that with end-seals.

Table 6: Geometry and operating condition for a TPTB from [40, 57] used for validation of reduced flow analysis.

Bearing properties		
Number of pads, N_P		8
Inner diameter, ID		133 mm
Outer diameter, OD		267 mm
Pad arc length		38°
Pivot circum. offset		50 %
Pivot radial offset		50 %
Pad thickness*, t_P		25 mm
Babbitt thickness*		2 mm
Pad area, A_P		45.6 cm^2
Operating condition		
Specific load		0.6-3.5 MPa
Shaft rotational speed		4-10 krpm
Supply pressure*		1 bar
Fluid properties		ISO VG32
Viscosity-temperature coefficient, α^*_{TV}		0.0247 1/°C
Viscosity, μ_{Su} (at 46°C)		22 cPoise
Density, ρ		821 kg/m^3
Specific heat capacity, c_P		2.17 kJ/(kg· °C)
Thermal conductivity, κ		0.13 W/(m· °C)
Pad material properties	Steel	Babbitt
Thermal conductivity, κ_P	51 W/(m·°C)	55 W/(m·°C)
Elasticity modulus, E	210 GPa	52 GPa
Thermal expansion, α_T	12 10^{-6}/°C	24 10^{-6}/°C
Poisson ratio, ν	0.3	0.3
Thermal properties		
FE reference temperature**		20 °C
Heat Transfer coefficient on back of pad** η		100 W/(m^2·°C)

*Assumed or calculated based on the available data .
**Taken from Ref.[35]

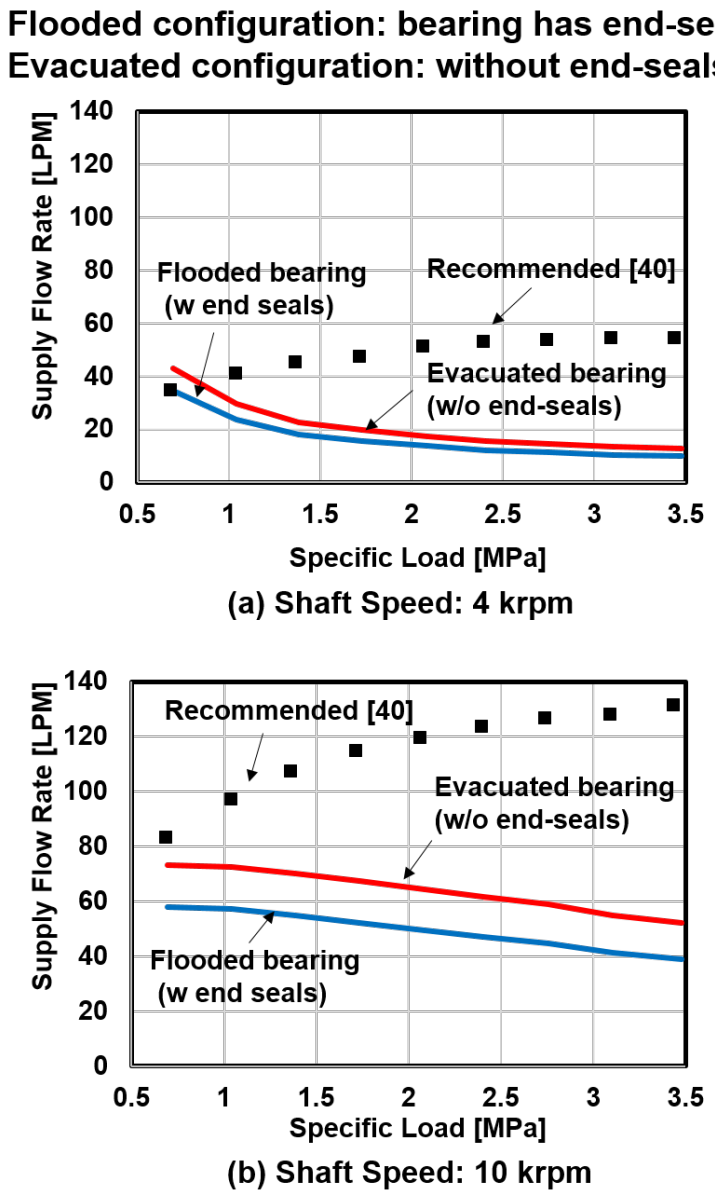

Fig. 36: Recommended and predicted (nominal) supply flow rate vs. specific load/pad for TPTB in Refs. [40, 57] with flooded configuration and evacuated configuration for operation at two shaft speeds: (a) 4 krpm and (b) 10 krpm. Graphs also show the nominal flow for TPTB with evacuated-ends.

The difference between the recommended flow rate and the nominal flow rate comes from their distinct function. Recall the purpose of the nominal flow is to fully lubricate the entire pad surface. Whereas, the recommended flow rate (taken from Ref. [16]) intends to increase heat transfer (advection) out of the bearing to reduce the pad temperature rise for all operating conditions, i.e. loads and speeds. Gregory [16] initially predicts the bearing load performance using a pressure boundary condition. Then, the recommended flow rate is calculated proportionate to the predicted bearing drag power loss. Gregory [16] states the calculated recommended flow rate is substantially larger than that needed to fully wet the entire bearing pads (nominal rate) but does not account for the influence of the excess supply flow rate on the bearing performance or drag power loss.

Measurements in Refs. [40, 57] show the recommended flow rate significantly increases the bearing drag power but has little influence on the pad maximum temperature. Nonetheless, the bearing discharge flow temperature shows notable reduction with the recommended flow rate. The predictions here are in agreement with measurements in Refs. [40, 57].

An increase in supply flow rate is mainly achieved by increasing the supply pressure[15] and that changes the pressure boundary condition at the pad leading edge. Refs.[40, 57] state that the maximum capacity of the lubrication system (pump) is $P_{Su_{max}}$ = 1.4 bar. However, the specific supply pressure associated with each supply flow rate (50%, 100%, and 150% recommended rate) is not disclosed.

[15]Supply pressure is measured with respect to the ambient pressure

Figure 37 depict the predicted discharge oil temperature rise and temperature rise at the pad mid radius and angular locations denoting a pad leading edge, pad center, and pad trailing edge from the present analysis. The experimental data in Ref. [23] relates to operation at three distinct supply flow rates; 50%, 100% and 150% of recommended flow. The bearing operates at 4 krpm angular speed and under a specific load per pad ranging from 0.7 MPa to 3.4 MPa. The flow is laminar for the operating conditions noted.

In Figure 37 (a), the experimentally recorded oil discharge temperature rise does not vary with an increasing load and increases significantly as the flow rate reduces to 50% of recommended rate. Operation with an over flow (150%) reduces the oil discharge temperature. The difference between oil discharge temperatures for the 50% and 150% flows is sizable. Predictions for the discharge temperature rise agree with the measurements, in particular for the flooded and over-flooded conditions. In any case, the maximum difference between a prediction and the test magnitude is < 4 °C.

In Figure 37 (b-d), the measured pad subsurface temperatures increase almost linearly with the specific load while showing a minor dependency on the supplied flow, above or below the recommended rate. The difference in temperatures at the pad trailing edge (hotter) and at the pad leading edge (colder) increases with the specific load. The predictions of temperature are very accurate when compared to those measured temperature at the pad center and at its trailing edge. The predicted temperature at the pad leading edge is higher than the one measured for operation with flow starvation. The discrepancy between

measurements and predictions does not exceed 11 °C (14% with respect to measurements).

Note, a 50% recommended flow rate produces flow starvation only for operation under a specific load per pad ranging from 0.7 MPa to 1.0 MP. See in Figure 36 (a) the nominal flow is more than half of the recommended flow rate under a light specific load < 1.0 MPa/pad. In fact, with a 50% flow, the pad effective arc length reduces from (actual) 38° to 35.4° when operating at 4 krpm and under 0.7 MPa/pad load, i.e a 7% reduction in the pad effective arc length. For loads > 1.0 MPa/pad, however, a 50% recommended flow is still larger than the predicted nominal rate, thus the bearing does not starve of flow.

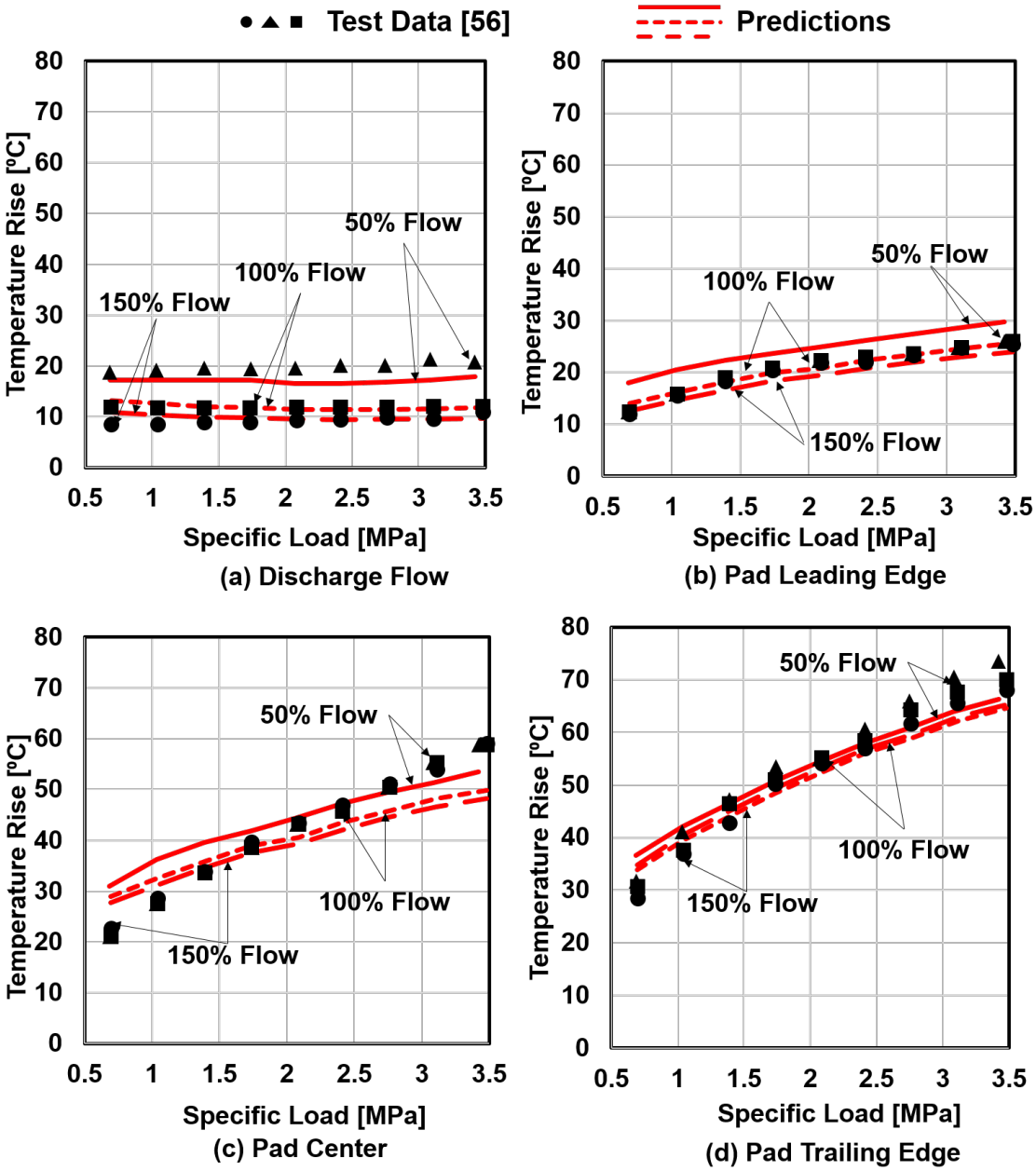

Fig. 37: Predicted (a) oil discharge temperature rise and subsurface temperature rises in (b) pad leading edge, (c) pad center and (c) pad trailing edge. Test data for a TPTB supplied with 50%, 100%, and 150% of recommended flow rate [57]. Supply temperature = 46℃ and shaft speed = 4 krpm.

For operation at 10 krpm rotor speed and with the fluid flow as fully turbulent, Figure 38 shows predictions and test data for the oil discharge temperature rise and pad subsurface temperature rise at an location at a 75% offset from the pad leading edge and 75% way from the pad inner radius. Note the oil discharge temperature slightly decreases with applied load and is much higher for the starved flow condition, the prediction lagging the recorded magnitude by nearly 10°C. Operation with an over flow (1.5 of recommended rate) produces a drop in the oil discharge temperature albeit increasing as the applied load increases. The predictions on the other hand do not show the apparent cooling effect as the load increases.

The measured pad subsurface temperature rise shows a linear increase with specific load. Under a light load of 0.7 MPa/pad, the pad temperature rise increases by 42%, from 43 °C to 61 °C, as the supply flow decreases to 50% of the recommended rate. The largest increase in pad temperature equals 90 °C and is independent of the flow condition, reduced or increased flow rate. Considering the oil supply temperature is 46 °C, a pad temperature of 136 °C is just above the Babbitt critical temperature of 130 °C. Experiments in Guo et al. [56] show that operation with a pad temperature exceeding 130 °C damages the Babbitt and results in bearing failure. The predicted pad temperature rise shows a trend consistent with the reduction in flow rate and is also proportional to the applied load. The differences with the measured temperatures decreases as the load increases.

At 10 krpm, the bearing lubricated with a 50% recommended flow starves under spe-

cific load < 1.5 MPa/pad. The pad effective length is 36.7° for operation with 50% flow and under 0.7 MPa, i.e. a 4% reduction in pad effective arc length. See in Figure 36 that 50% of the recommended rate still exceeds the nominal rate for specific load > 1.5 MPa/pad, thus the bearing does not starve of flow.

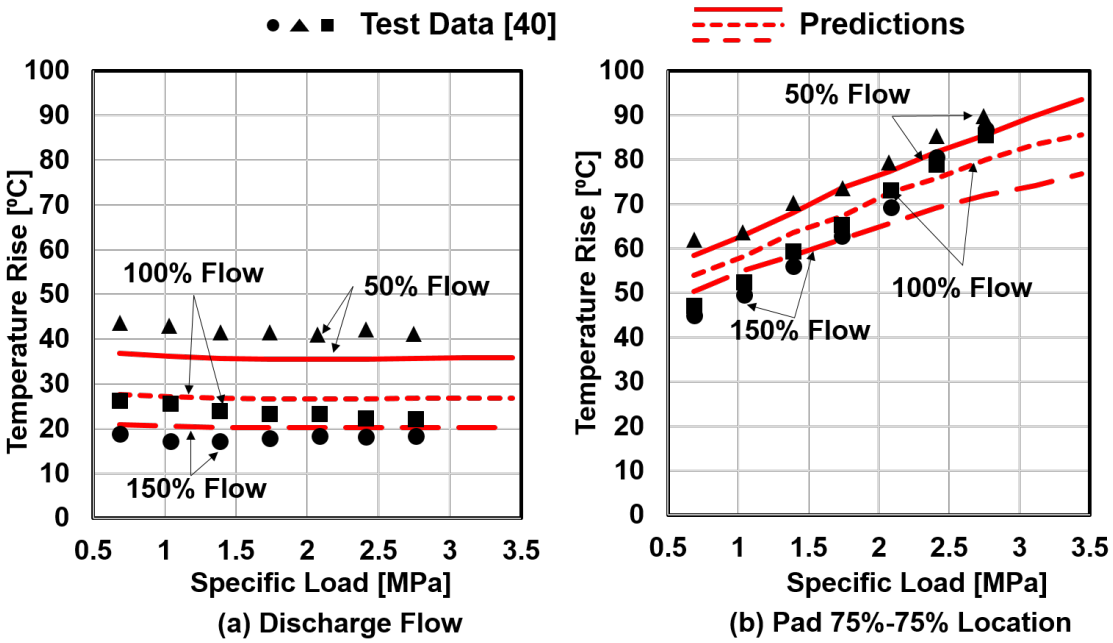

Fig. 38: Predicted (a) oil discharge temperature rise and (b) pad subsurface temperature rise at 75% offset from pad leading edge and 75% offset from pad inner radius. Test data for a TPTB supplied with 50%, 100%, and 150% of recommended flow rate [40]. Supply temperature = 46 ℃ and shaft speed = 4 krpm.

5.3 Flooded Configuration vs. Evacuated Configuration TPTB Load Performance

Figure 39 depicts load performance predictions for the TPTB in Table 6 with end-seals vs. those for an identical bearing but with evacuated-ends. The bearings operate under a

specific load per pad ranging from 0.5 MPa to 3.5 MPa and at speeds of 4 krpm (ΩR_o = 54m/s) and 10 krpm (ΩR_o = 135m/s), thus producing a laminar flow and a fully turbulent flow, respectively. The supply flow rate is nominal. Recall from Figure 36 that the nominal flow rate for the evacuated bearing is roughly 30% larger than that for the flooded bearing.

Note based on the measurements in Ref. [70], the heat transfer coefficient at the back surface of a pad in a flooded bearing varies from 200 W/ °C m^2 for operation at a low shaft speed with a laminar flow to 450 W/ °C m^2 for operation at a high rotor speed with a fully turbulent flow. In the absence of churning flow in an evacuated bearing, the heat transfer at the back surface of a pad is ~ 100 W/ °C m^2 [71].

In Figure 39 (a) as the specific load increases, the minimum film thickness in the end-seals bearing reduces from 49 μm to 20 μm at 4 krpm and from 97 μm to 39 μm at 10 krpm. The bearing with evacuated-ends operates with a thicker fluid film than that in the end-seals bearing. At 10 krpm, the difference reaches 11 μm under a light load of 0.5 MPa/pad, i.e. 12% larger than that in the end-seals bearing. The difference is, however, insignificant at 4 krpm and does not exceed 2 μm.

The predicted drag torque in Figure 39 (b) increases with load and shaft speed in both bearings, though the drag torque in the evacuated bearing is up 8% larger than that in the flooded bearing. For instance, at 10 krpm and under 3.5 MPa/pad, the predicted drag torque is 48 N.m in the flooded bearing but 51 N.m in the evacuated bearing. Note, end-seals trap the oil within the bearing housing, thus the oil churns and adds to the bearing

drag torque. The analysis is not capable of accounting for the churning oil drag torque in the end-seals bearing. Nonetheless in practice, end-seals bearings likely produce a larger drag torque than that in evacuated-ends bearings, specially at high rotor speeds. [66].

In Figure 39 (c), the bearing with evacuated-ends operates with a lower pad maximum temperature rise than that in the end-seals bearing and the difference increases with load and speed. At 10 krpm and under a heavy load of 3.5 MPa/pad, the pad maximum temperature rise is 95 °C in the end-seals bearing but 85 °C in the evacuated-ends bearing. The difference is 10 °C, and which represents a 11% reduction of the pad temperature rise in the end-seals bearing.

The pad peak hydrodynamic pressure in Figure 39 (d) is almost identical for both bearings and increases with the specific load from 1.2 MPa to 10.5 MPa at 4 krpm and 1.1 MPa to 8 MPa at 10 krpm.

In Figure 39 (e), the bearing (synchronous speed) axial stiffness coefficient increases with load and speed in both bearings. The end-seals bearing produces a larger axial stiffness than that in the evacuated-ends bearing. The difference is, however, notable only at a high rotor speed. At 10 krpm and under a heavy load of 3.5 MPa/pad, the end-seals bearing axial stiffness is 31 GN/m and which is 11% larger than that in the evacuated-ends bearing.

The bearing (synchronous speed) axial damping coefficient in both bearings in Figure 39 (f) increases with load but decreases with shaft speed. For instance, as the specific

load increases, the axial damping coefficient increases from 1.8 MN.s/m to 9.4 MN.s/m at 4 krpm and 0.7 MN.s/m to 3.2 MN.s/m at 10 krpm. The axial damping coefficient in the evacuated-ends bearing closely trails that in the bearing with end-seals, though the difference increases with speed.

In general, in an agreement with measurements in Refs.[66, 68], the predictions here show that the bearing ends configuration with end-seals vs. without end-seals (flooded vs. evacuated) affect bearing load performance only at high surface speeds >130 m/s.

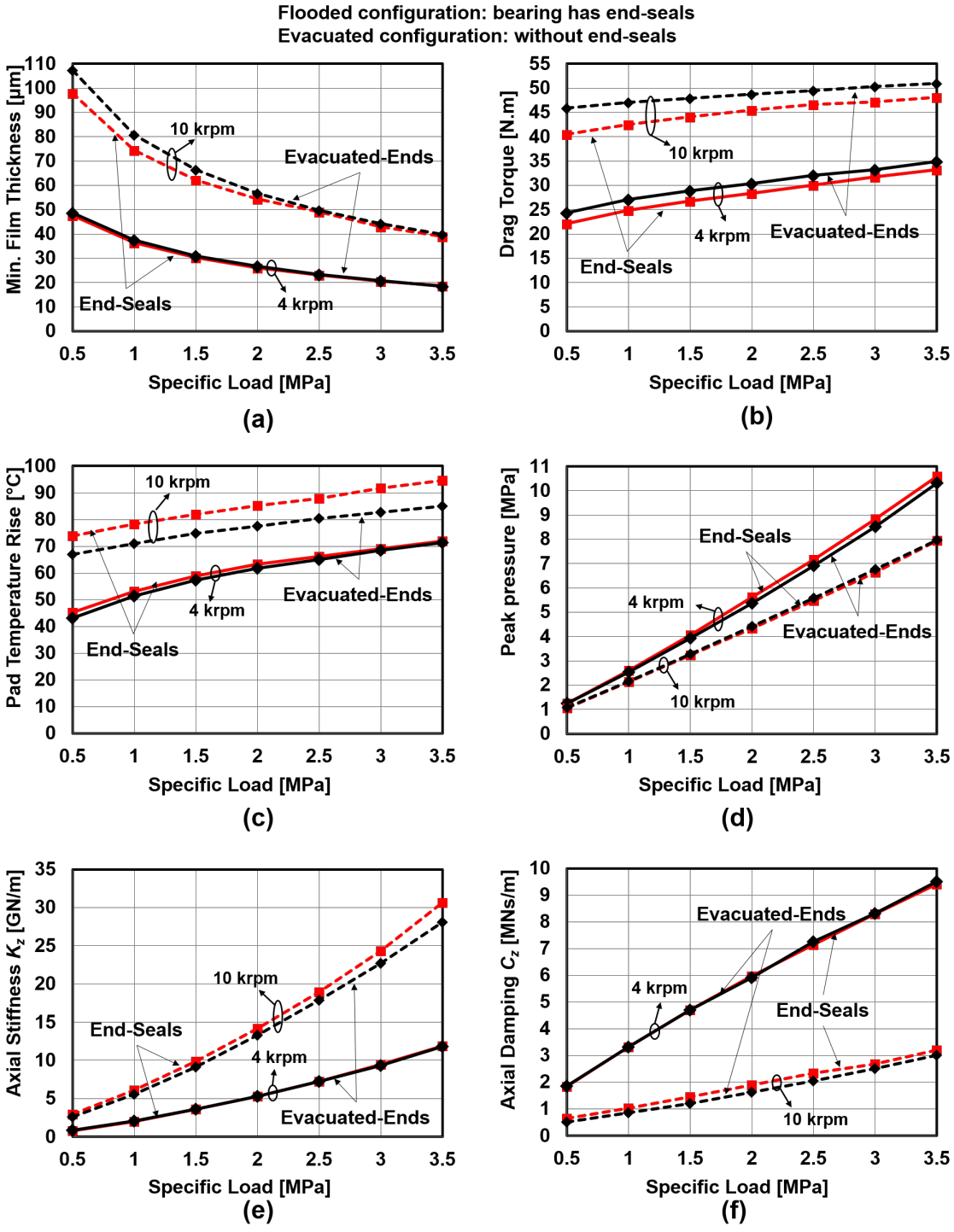

Fig. 39: Predicted (a) minimum film thickness, (b) bearing drag torque, (c) pad maximum temperature, (d) peak hydrodynamic pressure, (e) axial stiffness coefficient, and (f) axial damping coefficient for TPTBs with end-seals and evacuated-ends vs. specific load per pad. Supply temperature = 46°C and shaft speed = 4 krpm and 10 krpm. Nominal Flow rate.

5.4 Load Performance Predictions for a TPTB with Evacuated-Ends Operating under Starved Flow Conditions

For the example TPTB in Table 6, Figure 40 showcases on the left and right graphs of the predicted fluid film thickness and hydrodynamic pressure fields, respectively, for oil flow supply conditions with a nominal rate = 29 LPM (top graphs), 60% nominal flow (middle graphs), and 30% nominal flow (bottom graphs). The rotor speed is 4 krpm and the specific load per pad is 1 MPa. The nominal flow rate is 70% of the recommended flow in the past section. Note the bearing is evacuated (no end seals) meaning the oil that exits the pad, at its OD and ID, also leaves the bearing. Note for a flooded lubrication method with end seals, the oil leaving the pad at its ID remains in the groove oil bath and would be considered as carrying energy for the groove thermal energy balance, Eqn. (45).

In Figure 40 (a) for a fully flooded flow condition, the minimum film thickness varies from a maximum of 73 μm at the corner of the pad leading edge and OD to a minimum of 33 μm at the pad trailing edge and ID. The hydrodynamic pressure has a peak of 2.5 MPa near the pad center and gradually drops toward ambient at the pad edges. In Figure 40 (b) for a 60% nominal flow, the minimum film thickness field decreases roughly by 19 μm (42% lesser than that for flooded condition) while the maximum thickness equals 58 μm. The peak hydrodynamic pressure, however, increases by 36% to 3.4 MPa. In Figure 40 (c) for a lesser flow at 30% nominal, the smallest film thickness is 11 μm (1/3 of gap for flooded) while the peak pressure nearly doubles to reach 4.7 MPa. Note the labels in the pressure graphs indicating portions of the pad region that are denuded (starved) of

lubricant, i.e., these regions contain air.

For the same operating conditions as those in Fig. 40, Figure 41 shows the pressure profile (top graph) and film thickness at the pad mid radius arc. The differences in pressure profile are marked as the flow rate decreases. In short, when the pad starves of lubricant, the film thickness decreases and the hydrodynamic pressure region narrows and bulges toward the middle of the pad. The pad wetted arc extent lessens, as expected. Note the pad minimum film thickness moves toward the pad center as the supplied flow decreases to make a diverging gap at the pad trailing edge.

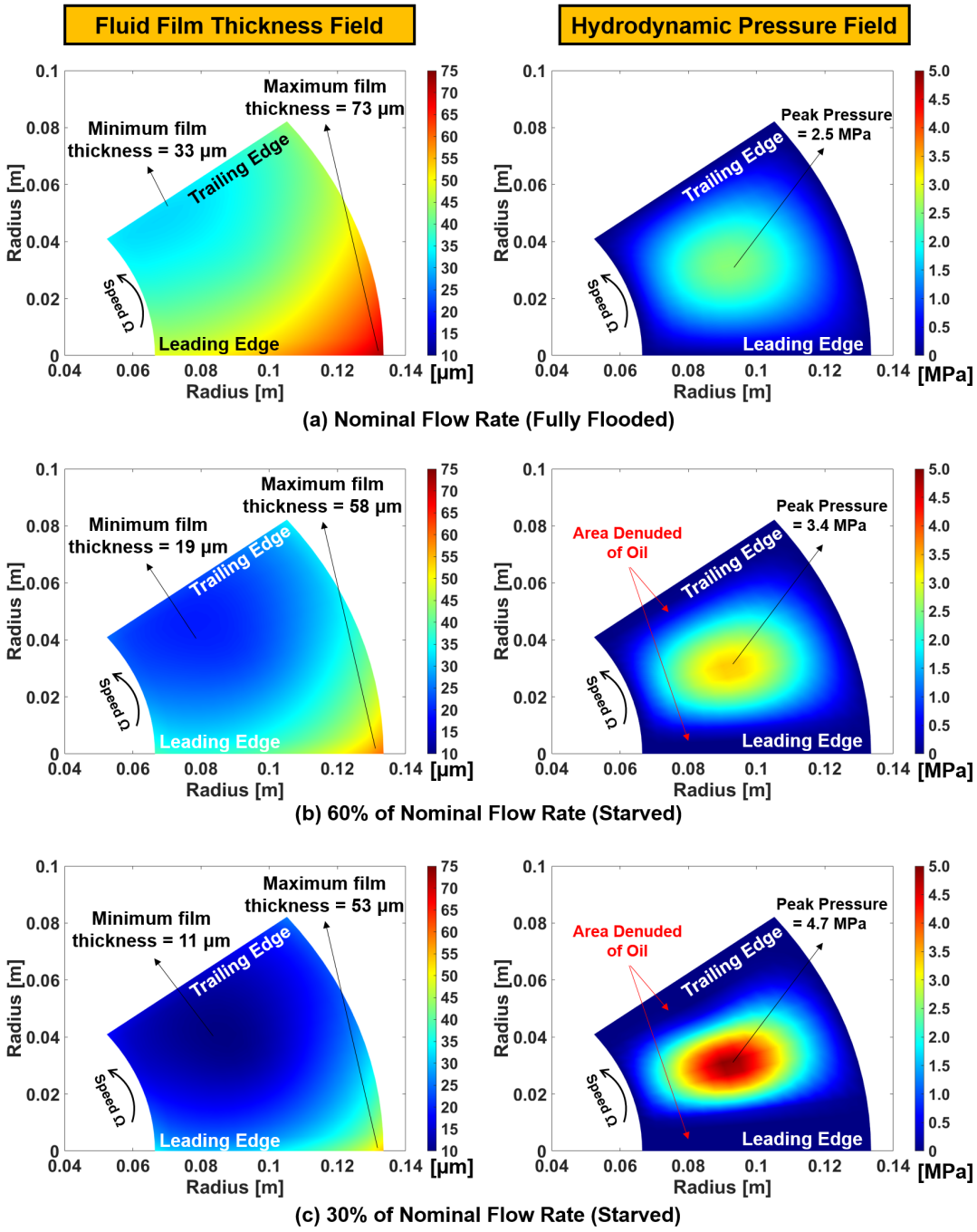

Fig. 40: Predicted film thickness field (left) and hydrodynamic pressure filed (right) for a TPTB operating with (a) nominal flow and with a starved flow at (b) 60% and (c) 30% of nominal rate. Supply temperature = 46℃, specific load = 1 MPa/pad, rotor speed = 4 krpm.

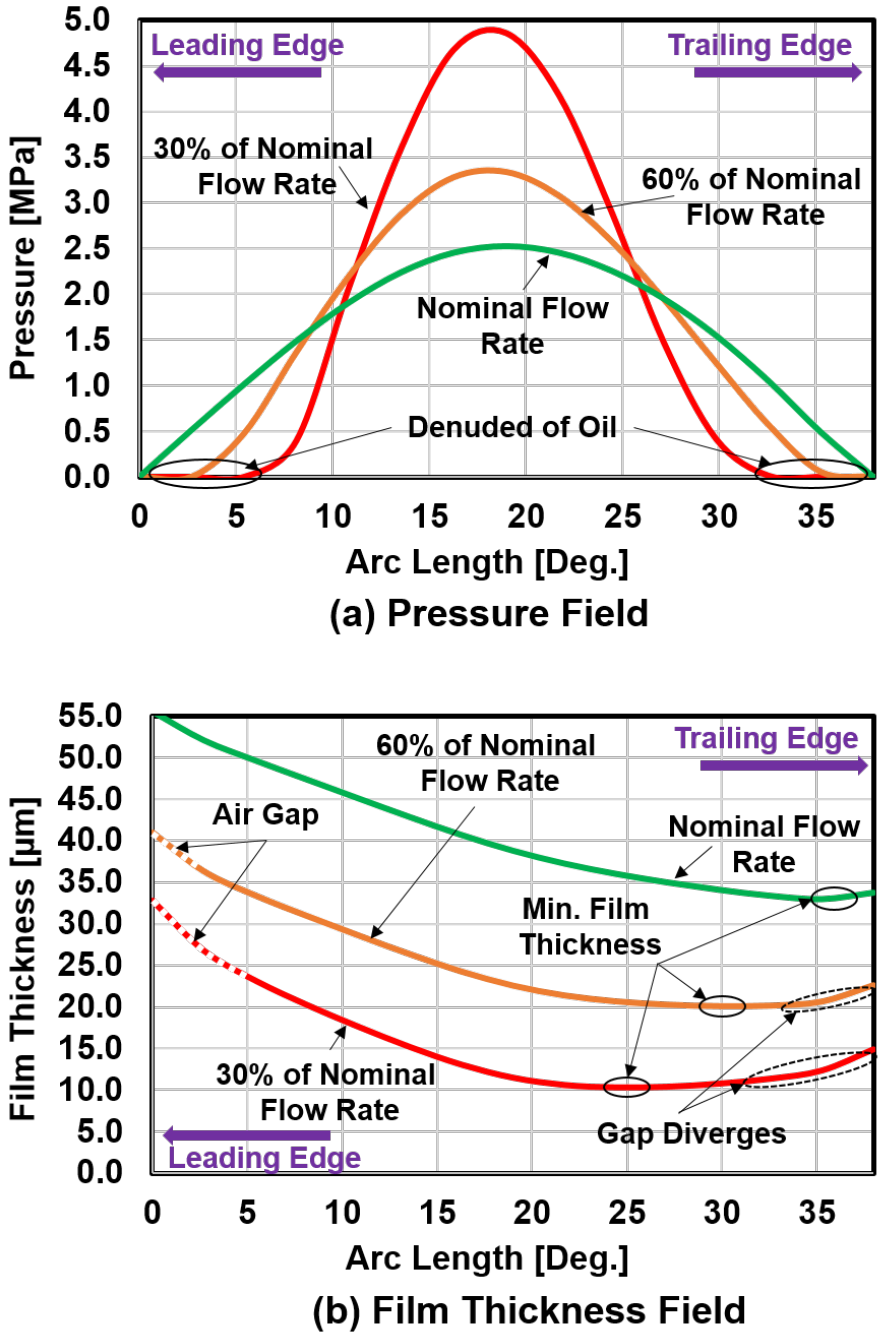

Fig. 41: Predicted (a) pressure field and (b) film thickness field at pad mid radius vs. angle θ. TPTB operating with nominal flow rate and under starvation with 60% and 30% of nominal flow rate. Supply temperature = 46℃, specific load = 1 MPa/pad, rotor speed = 4 krpm.

Figure 42 portrays the pad temperature field (left graphs) and the pad thermal deformation field (right graphs) as the supply flow rate decreases (top to bottom). Recall the oil supply temperature is 46 °C. Under a nominal flow condition see Fig. 42 (a), the pad temperature field increases from 62 °C at the bottom surface of the pad leading edge to a maximum of 109 °C at the Babbitt top surface near the pad trailing edge. Accordingly, the pad thermal deformation shows crowning with a peak of 16 μm at its center. A reduction in supply flow to 60% of nominal, see Fig. 42 (b), produces a 22 °C (20%) increase in the pad peak temperature followed by a 44% increase in thermal deformation to a peak of 23 μm. As the supply flow rate further decreases to just 30% of nominal, see Fig. 42(c), the pad peak temperature reaches 156 °C, a 43% increase compared to that obtained with a nominal flow rate, and well above the Babbitt material critical temperature of 130 °C. The pad peak thermal deformation also almost doubles to 30 μm.

Note the predicted pad mechanical deformations (not shown here) are relatively insignificant (maximum of 1 μm) whereas thermal deformations dominate the pads overall deformation. Nonetheless, the predicted pad mechanical deformation decreases under a starved flow condition as the pressure field concentrates more over the pad center area supported by the pivot.

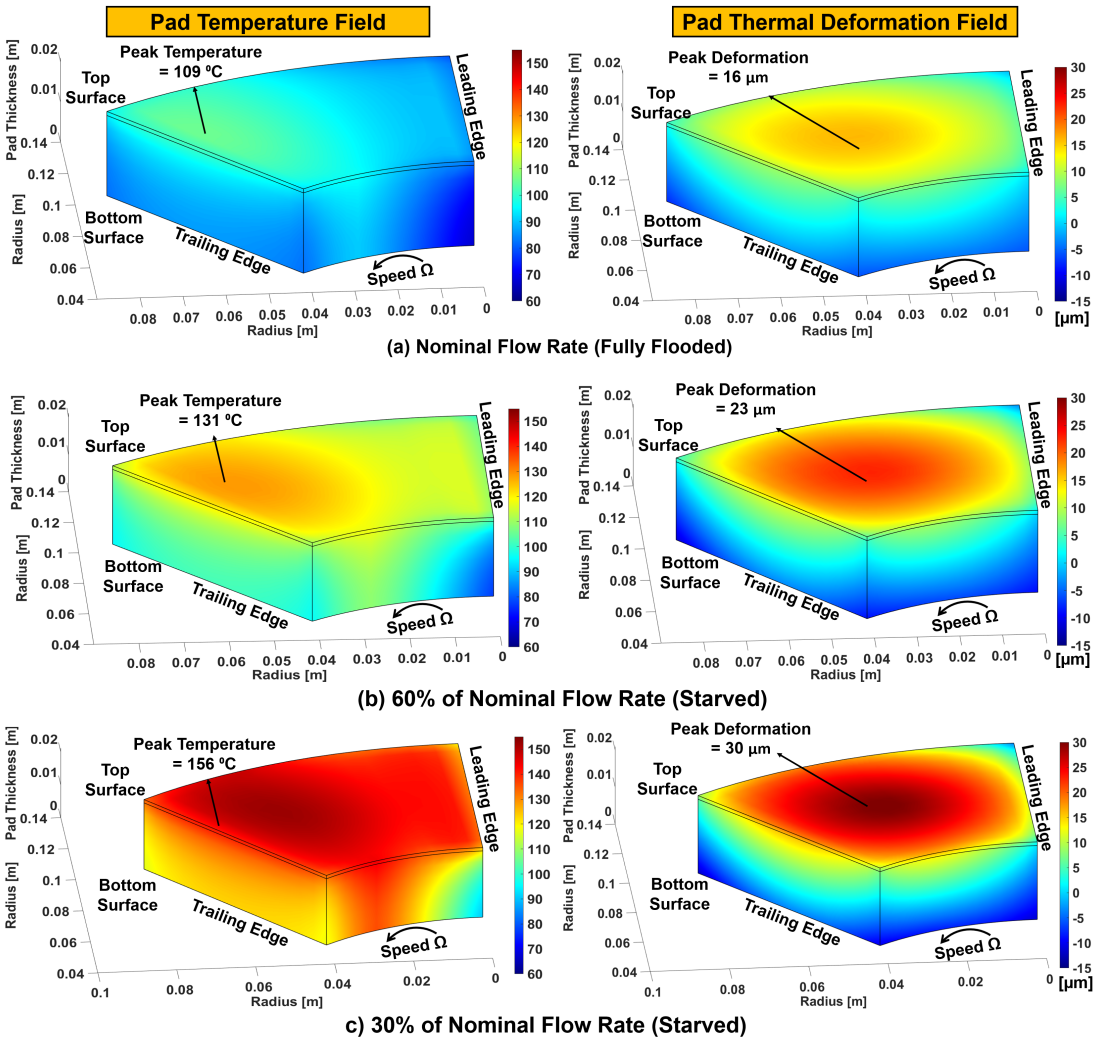

Fig. 42: Predicted pad temperature field (left) and thermally induced pad deformation field (right). TPTB operating with nominal flow rate and under starvation with 60% and 30% of nominal flow rate. Supply temperature = 46℃, specific load = 1 MPa/pad, rotor speed = 4 krpm.

The following figures depict various TPTB performance parameters versus supply flow rate varying over a wide range, 25% to 150% nominal, for operation with shaft speed at 4 krpm and under three specific loads/pad, 1 to 3 MPa. The bearing load performance with the manufacturer recommended flow rate is also marked on the right end of the graphs

with a circle symbol for comparison. Note from Figure 36, the predicted nominal flow rate decreases from 29 LPM to 13 LPM as the specific load increases from 1 MPa/pad to 3 MPa/pad. The recommended flow rate, however, is substantially larger than the predicted nominal rate and increases from 41 LPM to 55 LPM with load, i.e. 170% to 420% nominal rate, respectively.

Figure 43 shows the predicted pad effective arc length and effective pivot offset vs. supply flow rate ranging from 25% to 150% nominal flow. As expected, a reduction in the pad effective arc length begins only when the supply flow rate falls below the nominal rate. The rate of reduction in the pad arc length does not vary with load. With a 25% nominal flow, the pad effective arc length reduces by 8° to 30°, i.e. a 25% reduction in the pad arc length. Similarly, the effective pivot offset reduces from the original 50% to $\sim$ 39%. Recall from Figures 40 and 41, an area denuded of oil at the pad leading edge is followed by an area denuded of oil at the pad trailing edge of roughly the same size. Thus, the pivot location remains at the center of pressure field, i.e. with 50% offset, and the moment induced by the pressure field balances around the pivot.

Figure 44 shows the predicted (a) minimum film thickness, (b) peak hydrodynamic pressure, and (c) bearing drag torque vs. flow rate. Each graph shows on its right edge the predictions using a recommended flow rate as per prior section. Note that operation with an over flow (> 100%) affects little the peak pressure and the minimum film thickness but does increase the drag torque (and power). Similarly, operation with the recommended

flow rate shows insignificant improvement in minimum film thickness or peak pressure. Nonetheless, the bearing drag power loss significantly increases when using the recommended flow rate, up to 70% larger than that obtained for the nominal rate. Under starved flow conditions, the minimum film thickness drops linearly with a reduction in flow to reach a too low (critical) magnitude, 8 μm [9] or lesser for the largest load applied.

Similarly, the peak pressure increases up to 2.5 times as the supply flow rate decreases. Measurements in Ref. [72] show the ultimate strength of white-metal (Babbitt) significantly lowers as its temperature increases and could be as low as 18 MPa for temperatures $>$ 160 °C. The predicted pad peak pressure remains mostly below the Babbitt ultimate strength except for operation with a 3 MPa/pad and a supply flow rate lesser than 30% nominal. In Figure 44(c), the predicted drag torque decreases almost linearly as the supplied flow rate decreases. For instance, the drag torque for operation under a 3 MPa specific load per pad drops roughly by half from 38 N.m to 20 N.m as the supply flow rate decreases from 150% to 25% nominal rate.

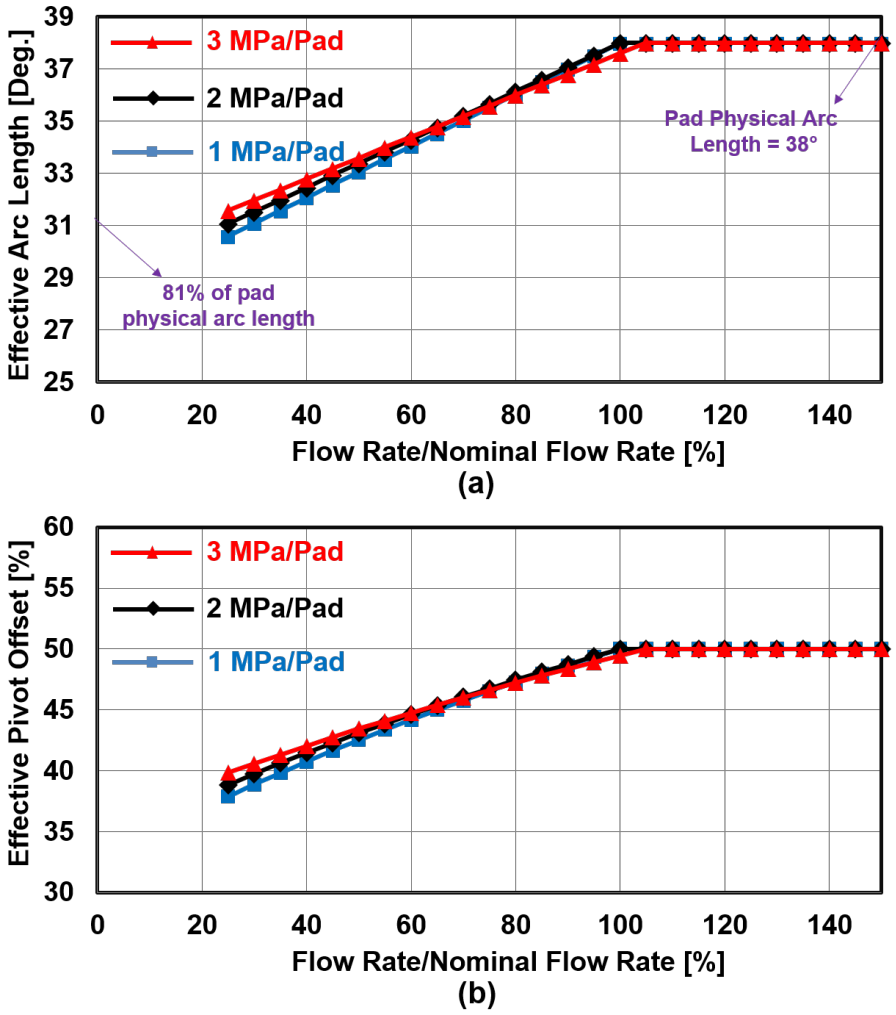

Fig. 43: Predicted (a) pad effective arc length and (b) effective pivot offset vs. nominal flow rate and specific load/pad: 1 MPa, 2 MPa, and 3 MPa. Supply temperature = 46℃, rotor speed = 4 krpm.

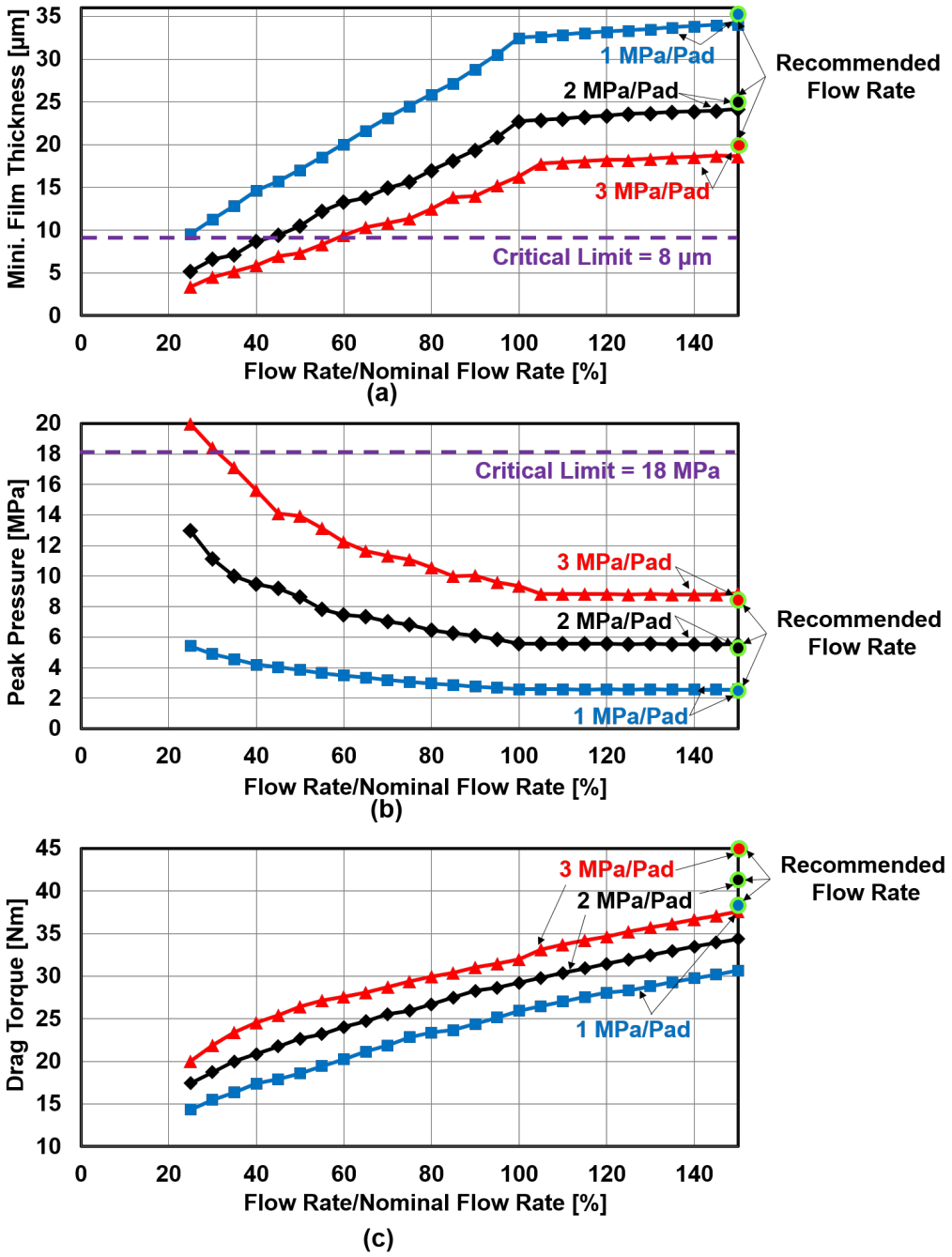

Fig. 44: Predicted (a) minimum film thickness, (b) peak pressure, and (c) bearing drag torque vs. nominal flow rate and specific load/pad: 1 MPa, 2 MPa, and 3 MPa. Graphs also show predictions for recommended flow rate (170% to 420% nominal). Supply temperature = 46℃, rotor speed = 4 krpm.

Figure 45 depicts the peak temperature rise and thermal deformation in a pad vs. supply flow and three applied loads, 1 to 3 MPa/pad. (From Fig. 42) Note the peak temperature occurs at the Babbitt top surface - trailing edge and OD, whereas the peak material deformation happens at the center of the pad. The predicted pad temperature rise is insignificant with an increase in supply flow rate above nominal, whereas a flow reduction below the nominal rate produces a substantial temperature rise. The predicted pad peak deformation also linearly increase as the supplied flow decreases below nominal. Recall that the Babbitt critical temperature = 130 °C. With a 3 MPa/pad, the peak temperature nearly doubles from 76 °C to 133 °C as the supply flow rate reduces from nominal to just 25% flow. Note the fluid film peak temperature rise (not shown here) is slightly larger than the pad peak temperature and close to 180 °C, near the oil flash point of 196 °C for ISO VG32 oil. Note under 3MPa/pad, the pad peak temperature rise is up to 10 °C lesser with the recommended flow rate than that with the nominal flow rate. The pad peak deformation is also up to 4 μm lesser with the recommended flow compared to that with nominal flow.

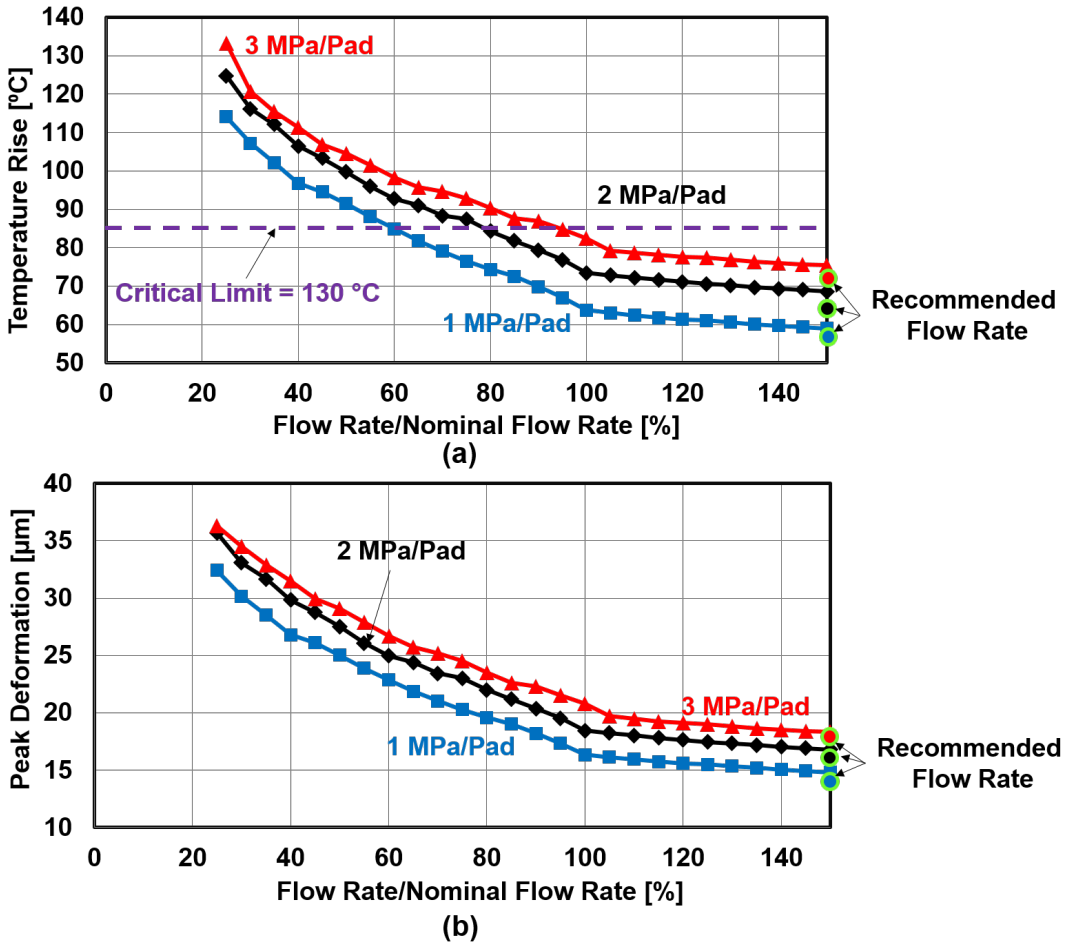

Fig. 45: Predicted (a) peak temperature rise and (b) peak thermal deformation in a pad vs. nominal flow rate and specific load/pad: 1 MPa, 2 MPa, and 3 MPa. Graphs also show predictions for recommended flow rate (170% to 420% nominal). Supply temperature = 46°C, rotor speed = 4 krpm.

Figure 46 shows the predicted bearing (synchronous speed) axial stiffness coefficient (K_z), damping coefficient (C_z), and ratio ($\Omega C_z/K_z$) vs. supply flow. An over flooded flow condition has no effect on the force coefficients. As the bearing starves of flow, the bearing axial stiffness coefficient increases while the axial damping coefficient drops. For operating under a heavy load of 3 MPa/pad, K_z triples, from 9 GN/m to 28 GN/m, as the supply flow rate decreases from nominal to 25%, whereas C_z decreases by 30% =, from 8.1 MN.s/m to 5.6 MN.s/m. Note as the supply flow rate decreases, the ratio ($\Omega C_z/K_z$) linearly drops, in particular under a light load, to reveal the absence of (axial) damping at too low flows. In this case, the axial natural frequency of the test system would increase while its damping ratio decreases to eventually produce an unstable operating condition.

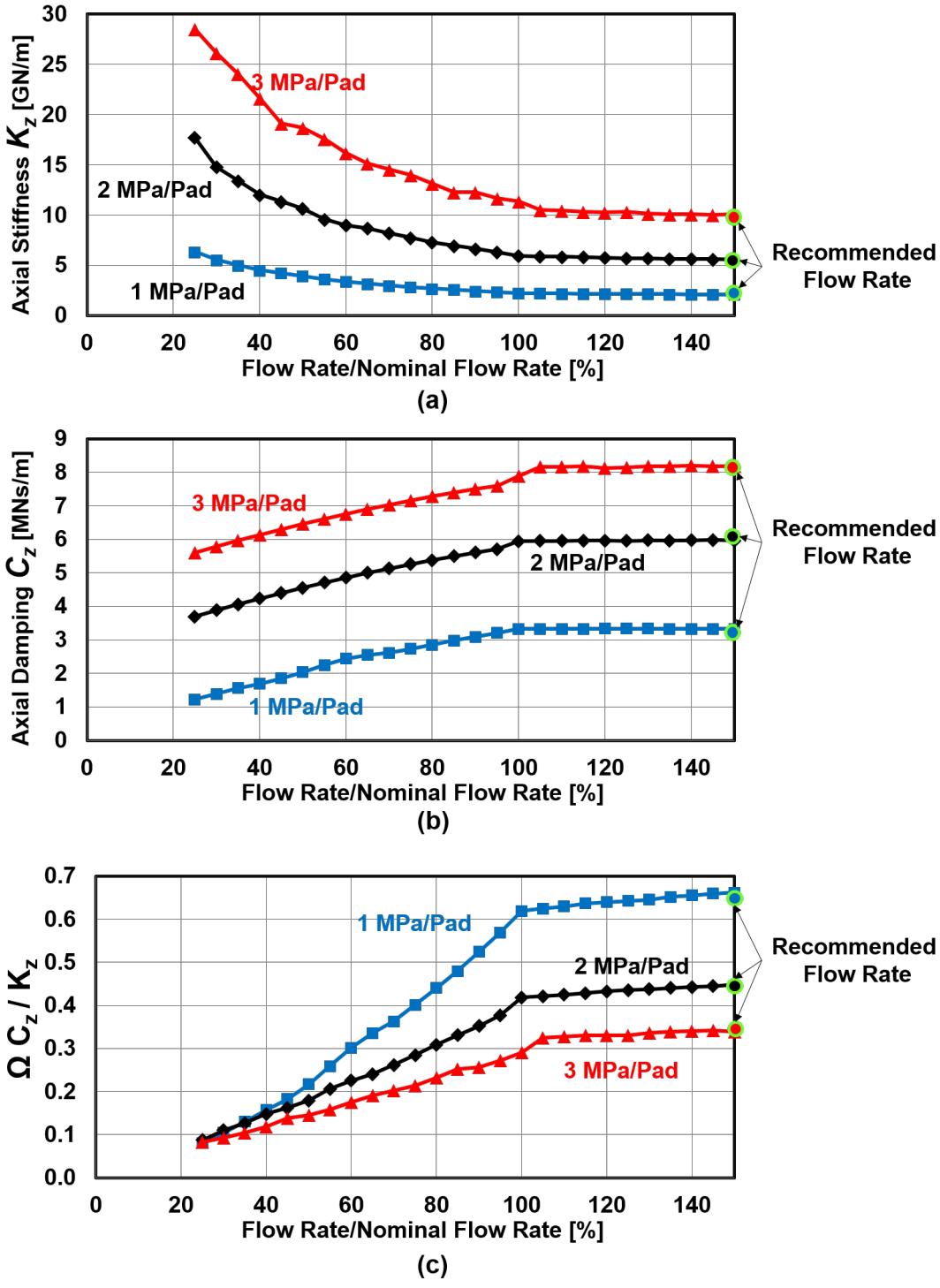

Fig. 46: Predicted TPTB (a) axial stiffness coefficient, (b) axial damping coefficient, (c) ratio ($\Omega C_z/K_z$) vs. nominal flow rate and specific load/pad: 1 MPa, 2 MPa, and 3 MPa. Graphs also show predictions for recommended flow rate (170% to 420% nominal). Supply temperature = 46℃, rotor speed = 4 krpm.

6 CONCLUSION

Widely used in rotating machinery, tilting pad thrust bearings (TPTBs) control rotor axial position to eliminate contact and wear of material surfaces and produce minimal drag power losses. Self-Equalizing TPTBs, an advanced design, further adjusts pad's position to accommodate for thrust collar misalignment and improves operation reliability. It is critical for turbomachinery industry to accurately evaluate the load performance of self-equalizing TPTBs.

The dissertation introduces a model for the analysis of a pad leveling mechanism coupled to a thermo-elasto-hydrodynamic (TEHD) tool to deliver load performance predictions for self-equalizing TPTB. The analysis also includes the friction forces acting at the contact points of the leveling plates. Further a Hertz contact model determines the peak pressure over the contact area of the leveling plates as a function of the applied load on the bearing pads as well as the leveling plates geometry. Note the wear rate at the leveling plates contact area is proportional to the applied pressure, and optimizing the design of the leveling plates to minimizing the peak contact pressure reduces wear.

The dissertation details performance predictions model for an example self-equalizing TPTB operating under light to heavy loads, i.e., specific load per pad = 1 MPa to 3 MPa. The main findings are:

- For operation with thrust collar static misalignment, an ideal self-equalizing TPTB

(without friction at the contacts) operates with up to 50% larger minimum fluid film thickness and with a 60% lesser peak film pressure compared to those obtained in a non-equalizing bearing.

- Friction forces acting at the contact points of the leveling plates significantly affect the performance of the pad leveling system as they reduce the minimum film thickness and increase the pad peak pressure. Eventually, the leveling plates could lock up as the contact friction increases, thus making the system ineffective.

- Variations of the pads peak temperature are insignificant (max of 9 °C) for both the regular and self-equalizing TPTBs.

- Predictions from the Hertz contact analysis agree with those from a commercial finite element analysis tool and show a significantly large peak pressure at the contact points of the leveling plates.

Note the actual magnitude of the friction coefficient on the contact area between the leveling plates is uncertain and varies from one contact point to the next. Future work is recommended to account for the variations in the friction coefficient, often determined by the operating conditions and wear of the parts.

Furthermore, this dissertation integrates a flow starvation model into the TEHD analysis tool to deliver load performance predictions for TPTBs operating with a reduced flow rate. The fluid inlet flow temperature at a pad leading edge follows from a groove thermal

mixing model (adopted from [26]) in the groove, and that accounts for the actual supply flow rate as well as the the hot oil entering the groove from the upstream pad trailing edge. The analysis also accounts for the churning flow in the bearing housing to differentiate operation between bearings with end-seals and those with evacuated-ends.

Under flow starvation, the work implements a model in San Andrés et al. [15] to itratively reduce the fluid film effective arc length until the supply flow rate is enough to fully fill the film gap. The oil discharge temperature and pad subsurface temperature from the current model match measurements for an eight-pad TPTB [40, 57] operating under a specific load/pad ranging from 0.7 MPa to 3.4 MPa and at rotor speeds of 4 krpm and 10 krpm ($R_o\Omega$= 54 m/s and 135m/s), spanning both laminar flow and fully turbulent flow regimes, respectively. The supply flow rate ranges from 150% to 50% of a manufacturer recommended rate ($\sim$ 170% to 420% of the nominal flow rate).

The work details characteristic load performance predictions vs. supply flow rate ranging from 150% to only 25% of the nominal rate for a TPTB with evacuated-ends operating under 1MPa to 3 MPa specific load per pad and at 4 krpm of rotor speed ($R_o\Omega$= 54). The major findings are:

- A supply flow rate exceeding the nominal one (fully wetting the whole pad) produces minimal improvements in pad minimum film thickness or peak temperature rise, whereas the drag power loss constantly increases with the supply flow rate.

- A flow reduction below the nominal rate produces areas denuded of oil at both the

pad leading edge and trailing edge, and thus produces an increase in the peak hydrodynamic pressure while reducing the minimum film thickness. For instance, under a light load, the peak pressure almost doubles and the minimum film thickness decreases by 2/3 as the supply flow rate decreases to 30% of the nominal rate.

- Under a heavy load of 3 MPa/pad, the pad peak temperature rise exceeds the Babbitt critical temperature = 130°C when the supply flow is below 80% of the nominal rate.

- Compared to a fully flooded operating condition, flow starvation produces a bearing with a larger axial stiffness coefficient but a much lesser axial damping coefficient. In this case, the axial natural frequency of the test system would increase while it's damping ratio quickly decreases to eventually produce an unstable operating condition.

- Predictions agrees with measurements in Ref.[40, 57] to show operation with the recommended flow rate substantially increases the bearing power loss but the pad maximum temperature does not notably reduce.

- At a high rotor speed of 10 krpm, compared to that in a bearing with flooded flow configuration (with end-seals), a bearing with evacuated configuration (without end-seals) requires a 30% larger supply flow rate and operates with up to 11 μm larger fluid film thickness, a 10 °C lesser pad temperature rise, and 11% larger axial stiffness coefficient. At a low rotor speed of 4 krpm, the bearing end configuration has a

marginal influence on the TPTB load performance.

Note the fluid film thickness field varies from one pad to another when a bearing operates with a misaligned thrust collar. Thus, pads with a larger fluid film thickness may starve of lubricant while other pads could become over-flooded. Future work should investigate the performance of a starved flow thrust bearing operating under thrust collar misalignment.

In sum, the dissertation relied upon simple but effective techniques to build thermo-elasto-hydrodynamic (TEHD) analyses for self-equalizing TPTBs and starved flow TPTBs. The analysis tool provides the designers of TPTBs with a state-of-the-art computational analysis model for self-equalizing TPTBs and starved flow TPTBs to produce unique knowledge on their load performance characteristics.

NOMENCLATURE

A_P	Pad surface Area [m^2].
c_P	Lubricant specific heat [J/kg °C].
e_c	Thrust collar axial location [m].
e_p	Pivot tip axial location [m].
E	Elasticity modulus [Pa].
h	Fluid film thickness [m].
h_u	Axial location of upper plates [m].
H_r, H_θ, G	Turbulent flow functions for Reynolds Equation.(2).
N	Shaft rotational speed [rpm], $N = \Omega\pi/30$.
N_P	Number of pads in a bearing.
P	Pressure [N/m^2].
Pr	Prandtl number.
Pr^*	Turbulent flow Prandtl number.
q	Heat Flow [W].
Q	Flow rate [LPM].
(r, θ, z)	Cylindrical coordinate system.
Re	Reynolds number $=\frac{\rho\Omega R h_{min}}{\mu}$
Re_L, Re_U	Upper and lower magnitude of critical Reynolds number
$R_i,\ R_o$	Inner radius and outer radius of a pad [m].

$R_P,\ \theta_P$	Pivot radial and circumferential location [m, rad].
t_P	Pad thickness [m].
T	Temperature [°C].
(U, V, W)	Fluid film velocity components [m/s].
(x, y, z)	Cartesian coordinate system.
W_z	Axial load on a pad.
$\alpha,\ \beta$	Pad tilt angles [rad].
α_T	Thermal expansion coefficient [1/°C].
ϵ_H	Eddy viscosity for heat transfer [m^2/s].
ϵ_M	Eddy viscosity for moment transfer [m^2/s].
ε_{ij}	Strain tensor $i, j = r, \theta, z$ [m/m].
η	Heat convection coefficient [W/m^2°C].
λ_{mix}	Groove flow thermal energy mixing coefficient [-].
ρ	Density [kg/m^3].
$\mathcal{P}$	Drag power loss [Watt].
κ, κ_P	Fluid and pad conductivity coefficient [W/m C].
μ	Fluid dynamic viscosity [Pa.s].
μ_r, μ_s	Rolling friction coefficient, sliding friction coefficient.
ρ	Fluid Density [kg/m^3].
σ_{ij}	Stress tensor $i, j = r, \theta, z$ [Pa].

ν	Material Poisson ratio.
ϕ, ψ	Thrust collar misalignment angles around X and Y axes [rad.].
Ω	Shaft angular speed [rad/s].
Φ	Thermal energy (heat) [J].

Matrices

$\vec{\mathbf{d}}$	Distance from a force acting point to a selected point [m].
$\vec{\mathbf{F}}^n$	Normal force [N].
$\vec{\mathbf{F}}^f$	Friction force [N].
$\mathbf{K}$	Pad structure stiffness matrix.
$\mathbf{K}_\theta$	Moment/tilt stiffness matrix [N.m/rad.].
$\vec{\mathbf{M}}$	Moment acting on leveling plates [N.m].
$\vec{\mathbf{n}}$	Surface normal vector [-].
$\vec{\mathbf{v}}$	Direction vector for the total force at a contact point [-].
$\vec{\mathbf{u}}$	Displacement vector [m].
$\vec{\sigma}$	Stress tensor [MPa].
$\vec{\varepsilon}$	Strain tensor [m/m].

Subscripts and Superscripts

BF	Back Flow.

DC	Discharge Flow.
e	Element.
G	Global.
i	Inner Radius.
ID	Inner Diameter.
LE	Leading edge.
lp	Lower plates.
L	Lubricant surrounding pad at the back and sides surfaces.
Nm	Nominal.
o	Outer radius.
OD	Outer Diameter.
P	Pad.
TE	Trailing edge.
SL	Side leakage flow.
Su	Supply flow.
up	Upper plates.
*	Turbulent flow.

Abbreviations

FE	Finite Element.

FDM	Finite Difference Method.
LP	Lower plates.
TEHD	Thermo-elasto-hydrodynamic
THD	Thermo-hydrodynamic.
TPTB	Tilting Pad Thrust Bearing.
UP	Upper plates.
1,2, or 3D	One, two, or three dimensional.

REFERENCES

[1] Gokaltun, S., and DeCamillo, S. "Computational Analysis of the Equalization Behavior of Thrust Bearings With Regular and Modified Leveling Plates," *ASME Turbo Expo: Paper No. GT2019-90504*.

[2] Koosha, R., and San Andrés, L., 2019, "Effect of pad and liner material properties on the static load performance of a tilting pad thrust bearing," *J. Eng. Gas Turb. Power,* **141**(12).

[3] Koosha, R., and San Andrés, L., 2020, "A Computational Model for the Analysis of the Static Forced Performance of Self-Equalizing Tilting Pad Thrust Bearings," *ASME Turbo Expo: Paper No. GT2020-16060*.

[4] Khonsari, M., 1987, "A Review of Thermal Effects in Hydrodynamic Bearings Part I: Slider and Thrust Bearings," *J. Tribol.,* **30**(1), pp. 19–25.

[5] Heshmat, H., and Pinkus, O., 1987, "Misalignment in Thrust Bearings Including Thermal and Cavitation Effects," *J. Tribol.,* **109**(1), pp. 108–114.

[6] Dadouche, A., DeCamillo, S. M., and Fillon, M., 2013, "Hydrodynamic Tilting-Pad Thrust Bearings," *Encyclopedia of Tribology*, pp. 1757–1765.

[7] Iliev, H., 1999, "Failure Analysis of Hydro-Generator Thrust Bearing," *J. Wear,* **225**(1), pp. 913–917.

[8] Branagan, L. A., 2015, "Survey of Damage Investigation of Babbitted Industrial Bearings," *J. Lub.,* **3**(2), pp. 91–112.

[9] He, M., Bryne, J. M., and Armentrout, R. W., 2018, "Fundamentals of Fluid Film Thrust Bearing Operation and Modeling," Asia Turbomachinery & Pump Symposium, Suntec, Singapore, 13-15 March. http://hdl.handle.net/1969.1/172449.

[10] Glavatskih, S. B., 2000, "Transient Thermal Effects in a Pivoted Pad Thrust Bearing," *Proc. Thinning Films and Tribological Interfaces Conference, The 26th Leeds-Lyon Symposium,* **38**(1), p. 229.

[11] Bavassano, F., Mantero, M., Traverso, R., Livermore-Hardy, R., and Blair, B., 2017, "A System Integration Approach for Heavy-Duty Gas Turbine Upgrades Using Improved Rotor Thrust Predictions and Application of Advanced Thrust Bearing Designs," *ASME Turbo Expo., Paper No. 63647, Charlotte, North Carolina, USA, June 26-30.*

[12] Glavatskih, S., and Fillon, M., 2004, "TEHD Analysis of Thrust Bearings with PTFE-Faced Pads," *ASME Int. J. Tribol. Con., Paper No. 64178*, pp. 603–613.

[13] Heinrichson, N., and Santos, I., 2006, *"On the Design of Tilting-Pad Thrust Bearings,"* Technical University of Denmark, Department of Mechanical EngineeringInstitut for Mekanisk Teknologi., Copenhagen, Denmark.

[14] Wodtke, M., Schubert, A., Fillon, M., Wasilczuk, M., and Pajaczkowski, P., 2014, "Large Hydrodynamic Thrust Bearing: Comparison of the Calculations and Measurements," *J. Eng. Tribol.,* **228**(9), pp. 974–983.

[15] San Andrés, L., Koo, B., and Hemmi, M., 2018, "A Flow Starvation Model for Tilting Pad Journal Bearings and Evaluation of Frequency Response Functions: A Contribution Toward Understanding the Onset of Low Frequency Shaft Motions," *J. Eng. Gas Turb. Power,* **140**(5), p. 052506.

[16] Gregory, R., 1979, "Factors Influencing Power Loss of Tilting-Pad Thrust Bearings," *J. Lub. Tech.,* **101**(2), pp. 154–160.

[17] Simmons, J., and Advani, S., 1987, "Paper II (III) Michell and the Development of Tilting Pad Bearings," *Tribology Series,* **11**, pp. 49–56.

[18] Kingsbury, A., 1951, "Development of the Kingsbury Thrust Bearing," *J. The American Society for Naval Engineers,* **63**(2), pp. 433–443.

[19] Brockett, t. S., 1995, "Thermoelastohydrodynamic Lubrication in Thrust Bearings," PhD Dissertation, University of Virginia, Charlottesville, VA, USA.

[20] Fogg, A., 1946, "Fluid Film Lubrication of Parallel Thrust Surfaces," *Proceedings of the Institution of Mechanical Engineers,* **155**(1), pp. 49–67.

[21] Jeng, M., Zhou, G., and Szeri, A., 1986, "A Thermohydrodynamic Solution of Pivoted Thrust Pads: Part I Theory," *J. Tribol.,* **108**(2), pp. 195–207.

[22] Jeng, M., Zhou, G., and Szeri, A., 1986, "A Thermohydrodynamic Solution of Pivoted Thrust Pads: Part II Static Loading," *J. Tribol.,* **108**(2), pp. 208–213.

[23] Jeng, M., and Szeri, A., 1986, "A Thermohydrodynamic Solution of Pivoted Thrust Pads: Part III Linearized Force Coefficients," *J. Tribol.,* **108**(2), pp. 214–218.

[24] Ng, C. W., and Pan, C., 1965, "A Linearized Turbulent Lubrication Theory," *J.Basic Engr.,* **87**(3), pp. 675–682.

[25] Almqvist, T., Glavatskikh, S., and Larsson, R., 1999, "THD Analysis of Tilting Pad Thrust Bearings-Comparison Between Theory and Experiments," *J. Tribol.,* **122**(2), pp. 412–417.

[26] Glavatskih, S. B., Fillon, M., and Larsson, R., 2002, "The Significance of Oil Thermal Properties On the Performance of a Tilting-Pad Thrust Bearing," *Transactions Tribology,* **124**(2), pp. 377–385.

[27] Brockett, T. S., Barrett, L. E., and Allaire, P. E., 1996, "Thermoelastohydrodynamic Analysis of Fixed Geometry Thrust Bearings Including Runner Deformation," *J. Tribol.,* **39**(3), pp. 555–562.

[28] Glavatskih, S., and Fillon, M., 2001, "TEHD Analysis of Tilting-Pad Thrust Bearings-Comparison with Experimental Data," *Int. Tribol. Con., Japan Society of Tribologists*, pp. 1579–1584.

[29] Radeş, M., 1972, "Dynamic Analysis of an Inertial Foundation Model," *Int. J. Solids Struc.,* **8**(12), pp. 1353–1372.

[30] Ettles, C., Knox, R., Ferguson, J., and Horner, D., 2003, "Test Results for PTFE-Faced Thrust Pads with Direct Comparison Against Babbitt-Faced Pads and Correlation with Analysis," *J. Tribol.,* **125**(4), pp. 814–823.

[31] Wasilczuk, M., and Rotta, G., 2008, "Modeling Lubricant Flow Between Thrust-Bearing Pads," *Tribology International,* **41**(9), pp. 908–913.

[32] Rotta, G., 2004, "Modeling of the Gap Between Thrust Bearing Pads," *J. Tribol.,* **35**(4), p. 196.

[33] Bielec, M., and Leopard, A., 1970, "Tilting Pad Thrust Bearings: Factors Affecting Performance and Improvements with Directed Lubrication," *Inst. Mech. Eng.,* **184**(12), pp. 93–102.

[34] Ahmed, S., Fillon, M., and Maspeyrot, P., 2010, "Influence of Pad and Runner Mechanical Deformations on the Performance of a Hydrodynamic Fixed Geometry Thrust Bearing," *J. Eng. Tribol. Part J,* **224**(4), pp. 305–315.

[35] Glavatskih, S., and Fillon, M., 2006, "TEHD Analysis of Thrust Bearings With PTFE-Faced Pads," *J. Tribol.,* **128**(1), pp. 49–58.

[36] Glavatskih, S., 2002, "Laboratory Research Facility for Testing Hydrodynamic Thrust Bearings," *J. Eng. Tribol.,* **216**(2), pp. 105–116.

[37] Souchet, D., 1991, "Comportement Thermohydrodynamique des Butées à Patins Oscillants en Régime Laminaire et Turbulent," PhD Dissertation, University of Poitiers, Poitiers, France.

[38] Pajaczkowski, P., Schubert, A., Wasilczuk, M., and Wodtke, M., 2014, "Simulation of Large Thrust-Bearing Performance at Transient States, Warm and Cold Start-up," *J. Eng. Tribol.,* **228**(1), pp. 96–103.

[39] San Andrés, L., Hardik, J., Kaizar, H., and Thorat, M., 2020, "On the Effect of Supplied Flow Rate to the Performance of a Tilting-Pad Journal Bearing - Static Load and Dynamic Force Measurements," *ASME Paper GT2020-16215*.

[40] Capitao, J., Gregory, R., and Whitford, R., 1976, "Effects of High-Operating Speeds on Tilting Pad Thrust Bearing Performance," *J. Lub. Tech.,* **98**(1), pp. 73–79.

[41] Artiles, A., and Heshmat, H., 1987, "Analysis of Starved Thrust Bearings Including Temperature Effects," *J. Tribol.,* **109**(3), pp. 395–401.

[42] DeCamillo, S., 2014, Axial Subsynchronous Vibration 43rd Turbomachinery & 30th Pump Users Symposia (Pump & Turbo 2014), Texas A&M University., September 23-25.

[43] DeCamillo, S. M., He, M., and Cloud, C. H., 2008, Journal Bearing Vibration and SSV Hash 37th Turbomachinery & 25th Pump Users Symposia (Pump & Turbo 2008), Texas A&M University., September 23-25.

[44] He, M., Allaire, P., Barrett, L., and Nicholas, J., 2005, "Thermohydrodynamic modeling of leading-edge groove bearings under starvation condition," *Tribology Transactions,* **48**(3), pp. 362–369.

[45] Heshmat, H., and Pinkus, O., 1985, "Performance of starved journal bearings with oil ring lubrication," *J. Tribol.,* **107**(1), pp. 23–31.

[46] Abdollahi, B., and San Andrés, L., 2019, "Improved Estimation of Bearing Pads' Inlet Temperature: A Model for Lubricant Mixing at Oil Feed Ports and Validation against Test Data," *J.Tribol.,* **141**(3).

[47] Ettles, C., 1970, "Hot Oil Carry-Over in Thrust Bearings," *Proc. Instn Mech Engrs, Industrial Lubrication and Tribology,* **22**(8), p. 209.

[48] Sternlicht, B., Carter, G., and Arwas, E., 1961, "Adiabatic Analysis of Elastic, Centrally Pivoted, Sector, Thrust-Bearing Pads," *J. App. Mech.,* **28**(2), pp. 179–187.

[49] Vohr, J., 1981, "Prediction of the Operating Temperature of Thrust Bearings," *J. Lub. Tech.,* **103**(1), pp. 97–106.

[50] Glavatskih, S., McCarthy, D., and Sherrington, I., 2005, "Hydrodynamic performance of a thrust bearing with micropatterned pads," *Tribol. Trans.,* **48**(4), pp. 492–498.

[51] Hashimoto, H., 1990, "Performance Characteristic Analysis of Sector-Shaped Pad Thrust Bearings in Turbulent Inertial Flow Regime Under Three Types of Lubrication Conditions," *Journal of Tribology,* **112**(3), pp. 477–484.

[52] San Andrés, L., and Koosha, R., 2018, "A Thermo-Elasto-Hydrodynamic (TEHD) Computational Analysis of Tilting Pad Thrust Bearings: Analytical and Fe Pad Structure Models" Annual Report to TRC Meeting, TRC-B&C-01-18, Texas A&M University, College Station, TX., May 15-17.

[53] Abramovitz, S., 1955, "Turbulence in a Tilting-Pad Thrust Bearing," *J. Franklin Ins.,* **259**(1), pp. 61–64.

[54] Gregory, R., 1974, "Performance of Thrust Bearings at High Operating Speeds," *J. Lub. Tech.,* **96**(1), pp. 7–13.

[55] San Andrés, L., and Koosha, R., 2017, "Thermo Hydrodynamic (THD) Computational Analysis for Tilting Pad Thrust Bearings (TPTBs)," Annual Report to TRC Meeting, TRC-B&C-05-17, Texas A&M University, College Station, TX.

[56] Guo, A., Wang, X., Jin, J., Hua, D. Y., and Hua, Z., 2015, "Experimental Test of Static and Dynamic Characteristics of Tilting Pad Thrust Bearings," *Adv. Mech. Eng.,* **7**(7), pp. 1–8.

[57] Mikula, A. M., 1986, "Evaluating Tilting Pad Thrust Bearing Operating Temperatures," *J. Tribol.,* **29**(2), pp. 173–178.

[58] Glavatskikh, S. B., 2001, "Steady State Performance Characteristics of a Tilting Pad Thrust Bearing," *J. Tribol.,* **123**(3), pp. 608–615.

[59] San Andrés, L., and Koosha, R., 2019, "A Computational Model for the Forced Performance Analysis of Self-Equalizing Tilting Pad Thrust Bearings" Annual Report to TRC Meeting, TRC-B&C-01-19, Texas A&M University, College Station, TX., May 21-23.

[60] Wygant, K. D., Flack, R. D., and Barrett, L. E., 1999, "Influence of Pad Pivot Friction on Tilting-Pad Journal Bearing Measurements—Part I: Steady Operating Position," *J. Tribol. trans.,* **42**(1), pp. 210–215.

[61] Popov, V. L., 2010, *Contact Mechanics and Friction*, 2 ed. Springer, New York, NY, USA.

[62] Cross, R., 2015, "Effects of Surface Roughness on Rolling Friction," *European J. Physics,* **36**(6), p. 065029.

[63] Myant, C., Spikes, H., and Stokes, J., 2010, "Influence of Load and Elastic Properties on the Rolling and Sliding Friction of Lubricated Compliant Contacts," *J. Tribol. Intern.,* **43**(2), pp. 55–63.

[64] Shigley, J. E., 2011, *Shigley's Mechanical Engineering Design,*, 4 ed. Tata McGraw-Hill Education, New York, NY, US.

[65] San Andrés, L., and Koosha, R., 2020, "A Model for The Analysis of Flow Starved Tilting Pad Thrust Bearings" Annual Report to TRC Meeting, TRC-B&C-05-20, Texas A&M University, College Station, USA., June 10-13.

[66] Dmochowski, W., and Blair, B., 2006, "Effect of oil Evacuation on the Static and Dynamic Properties of Tilting Pad Journal Bearings," *Tribol. Trans.,* **49**(4), pp. 536–544.

[67] Capitao, J. W., 1976, "Performance Characteristics of Tilting Pad Thrust Bearings at High Operating Speeds," *J. Lub. Tech.,* **98**(1), 01, pp. 81–88.

[68] Nicholas, J. C., Elliott, G., Shoup, T. P., Martin, E., et al., 2008, Tilting Pad Journal Bearing Starvation Effects 37th Turbomachinery Symposia (Pump & Turbo 2008), Texas A&M University., September 23-25.

[69] Heshmat, H., and Gorski, P., 1987, "Mixing Inlet Temperatures in Starved Journal Bearings," *Tribology Series,* **11**, pp. 73 – 79.

[70] El-Saie, Y. A., and Fenner, R., 1988, "Three-Dimensional Thermoelastohydrodynamic Analysis of Pivoted Pad Thrust Bearings Part 1: Treatment of Bearing Deflections and Fluid Film Flow and Heat Transfer," *Proceedings of the Institution of Mechanical Engineers, Part C: Journal of Mechanical Engineering Science,* **202**(1), pp. 39–50.

[71] Ettles, C. M., and Anderson, H. G., 1991, "Three-Dimensional Thermoelastic Solutions of Thrust Bearings Using Code Marmac1," *Journal of Tribology,* **113**(2), 04, pp. 405–412.

[72] Freeman, J. R., and Woodward, R. W., 1921, *Some Properties of White Metal Bearing Alloys at Elevated Temperatures* No. 188 US Government Printing Office.

[73] Ng, C. W., 1964, "Fluid Dynamic Foundation of Turbulent Lubrication Theory," *J. Tribol.,* **7**(4), pp. 311–321.

[74] Taniguchi, S., Makino, T., Takeshita, K., and Ichimura, T., 1990, "A Thermohydrodynamic Analysis of Large Tilting Pad Journal Bearing in Laminar and Turbulent Flow Regimes with Mixing," *J. Tribol,* **112**(3), pp. 542–548.

APPENDIX A TURBULENT FLOW MODEL

The Ng and Pan linearized model of turbulent flow [24, 73] assumes the local shear stress τ is a superposition of the Couette shear τ_c and the linear terms of the pressure induced flow shear (τ_r,τ_θ) and represents τ as a small perturbation of τ_c. Thus, the eddy viscosity for momentum transfer is [21],

$$\begin{aligned}\frac{\epsilon_m}{\upsilon}(z,|\tau|) \approx & \frac{\epsilon_m}{\upsilon}(z,|\tau_c|) + \delta\tau_\theta \frac{\partial\left(\frac{\epsilon_m}{\upsilon}\right)}{\partial\tau}\bigg|_{\tau=\tau_c} \\ & = f(z) - 1 + g(z)\frac{\delta\tau_\theta}{\tau_c}\end{aligned} \tag{A.1}$$

where turbulent flow functions $f(z)$ and $g(z)$ are calculated using Reichardt's "wall formula",

$$f(z) = 1 + \frac{\epsilon_m}{\upsilon}(z,|\tau_c|) = 1 + \kappa_f\left[z_c^+ - \delta_l^+ \tanh\left(\frac{z_c^+}{\delta_l^+}\right)\right] \tag{A.2a}$$

$$g(z) = \tau_c \frac{\partial\left(\frac{\epsilon_m}{\upsilon}\right)}{\partial\tau}\bigg|_{\tau=\tau_c} = \frac{1}{2}\kappa_f z_c^+ \tanh^2\left(\frac{z_c^+}{\delta_l^+}\right) \tag{A.2b}$$

here κ_f and δ_l^+ are Reichardt's formula coefficients with typical values of 0.4 and 10.7 [24], respectively, and

$$z_c^+ = \frac{z}{\upsilon}\sqrt{\frac{\tau_c}{\rho}} \tag{A.3}$$

here the Couette shear stress τ_c is itself a function of turbulent flow function f,

$$\tau_c = \frac{r\Omega}{\int_0^h \frac{dz}{\mu_{(z)} f(z)}} \tag{A.4}$$

and necessitates an iterative solution between Eqns. (A.2) and (A.4).

In the generalized Reynolds equation (2), H_r, H_θ, and G are also functions of flow

turbulent, defined as, [21]

$$H_{r_{(r,\theta)}} = \int_0^h \int_0^z \zeta_3(\bar{z})\, d\bar{z}\, dz - \frac{\int_0^h \zeta_3(z)dz}{\int_0^h \zeta_4(z)dz} \int_0^h \int_0^z \zeta_4(\bar{z})\, d\bar{z}\, dz \tag{A.5a}$$

$$H_{\theta_{(r,\theta)}} = \int_0^h \left(\int_0^z \zeta_1(\bar{z}) d\bar{z} \right) dz - \frac{\int_0^h \zeta_1(z)dz}{\int_0^h \zeta_2(z)dz} \int_0^h \left(\int_0^z \zeta_2(\bar{z}) d\bar{z} \right) dz \tag{A.5b}$$

$$G_{(r,\theta)} = h - \frac{1}{\int_0^h \zeta_4(z)dz} \int_0^h \left(\int_0^z \zeta_4(\bar{z}) d\bar{z} \right) dz \tag{A.5c}$$

Above, ζ_i , $i = 1 : 4$ are functions of the local viscosity (μ) and turbulent flow functions $f(z)$ and $g(z)$, hereby given as [21]

$$\zeta_1(z) = \frac{\frac{h}{2} - z}{\mu_{(z)} f(z)} \left(1 - \frac{g(z)}{f(z)} \right) \tag{A.6a}$$

$$\zeta_2(z) = \frac{1}{\mu_{(z)} f(z)} \left(1 - \frac{g(z)}{f(z)} \right) \tag{A.6b}$$

$$\zeta_3(z) = \frac{\frac{h}{2} - z}{\mu_{(z)} f(z)} \tag{A.6c}$$

$$\zeta_4(z) = \frac{1}{\mu_{(z)} f(z)} \tag{A.6d}$$

Hence, the eddy viscosity for momentum transfer is calculated based on Eqns. (A.6) and (A.1) as,

$$\frac{\epsilon_m}{\upsilon}(z) = f(z) - 1 + g(z) \frac{\zeta_4(h)}{r\Omega} \frac{\partial P}{\partial \theta} \left(z - \frac{h}{2} + \frac{\zeta_1(h)}{\zeta_2(h)} \right) \tag{A.7}$$

When using Riechardt's formula, Eqn. (A.7), to evaluate eddy viscosity, the transition between laminar flow and turbulent flow occurs smooth and gradually and which is not consistent with experimental observations [21]. Thus, it is a common practice to introduce

a scalar factor $\vartheta 5$ into eddy viscosity [19, 21, 74], i.e.

$$\vartheta(Re) = \begin{cases} 0.0 & Re \leq Re_L \\ 1.0 - \left(\frac{Re_U - Re_h}{Re_U - Re_L}\right)^{\frac{1}{8}} & Re_L < Re \leq Re_U \\ 1.0 & Re_U < Re \end{cases} \tag{A.8}$$

where Re is a characteristic Reynolds number and Re_U and Re_L are upper and lower band for critical Reynolds number. Accordingly, the equivalent turbulent flow viscosity μ^* and heat conductivity κ^* are

$$\mu^*(r, \theta, z) = \mu\left(1 + \vartheta_{(Re)}\frac{\epsilon_m}{\upsilon}\right) \tag{A.9a}$$

$$\kappa^*(r, \theta, z) = \kappa\left(1 + \vartheta_{(Re)} Pr \frac{\epsilon_H}{\upsilon}\right) = \kappa\left(1 + \vartheta_{(Re)}\frac{Pr}{Pr^*}\frac{\epsilon_m}{\upsilon}\right) \tag{A.9b}$$

where the lubricant conductivity κ is constant over the entire film domain and lubricant viscosity (μ) is a function of local temperature (T),

$$\mu = \mu_{Su}\, e^{-\alpha_{VT}(T - T_{Su})} \tag{A.10}$$

where μ_{Su} and T_{Su} are fluid viscosity and temperature at supply condition and α_{VT} is a fluid temperature-viscosity coefficient.

The Prandtl number Pr and the turbulent Prandtl number Pr^* are,

$$Pr = \frac{\mu c_P}{k} \tag{A.11a}$$

$$Pr^* = \frac{\epsilon_m}{\epsilon_H} \approx 1 \tag{A.11b}$$

and ϵ_H is the eddy viscosity for heat transfer.

APPENDIX B FINITE ELEMENT MODEL FOR PADS

B.1 THE PRINCIPAL OF THE MINIMUM ENERGY

The deformations in a pad is governed by a series of equations known as elasticity equations, namely equilibrium equation, strain-displacements equation, and material law. Let σ represents the stress components in a cylindrical coordinates system, [19]

$$\sigma = \begin{Bmatrix} \sigma_{rr} \\ \sigma_{\theta\theta} \\ \sigma_{zz} \\ \tau_{r\theta} \\ \tau_{rz} \\ \tau_{\theta z} \end{Bmatrix} \tag{B.1}$$

then, a solid subjected to body force $\overline{\mathbf{F}}$ ($\{\overline{F}_r, \overline{F}_\theta, \overline{F}_z\}^T$) is only in equilibrium if,

$$\mathbf{D}_\sigma^T \sigma + \overline{\mathbf{F}} = 0 \tag{B.2}$$

where the differential operator $\mathbf{D}_\sigma$ is

$$\mathbf{D}_\sigma = \begin{bmatrix} \left(\frac{\partial}{\partial r} + \frac{1}{r}\right) & 0 & 0 \\ -\frac{1}{r} & \frac{\partial}{r\partial\theta} & 0 \\ 0 & 0 & \frac{\partial}{\partial z} \\ \frac{\partial}{r\partial\theta} & \left(\frac{\partial}{\partial r} + \frac{2}{r}\right) & 0 \\ \frac{\partial}{\partial z} & 0 & \left(\frac{\partial}{\partial r} + \frac{1}{r}\right) \\ 0 & \frac{\partial}{\partial z} & \frac{\partial}{r\partial\theta} \end{bmatrix} \tag{B.3}$$

The thermoelastic law correlates the stress components (Eqn. B.1) to any initial, thermal or mechanical strain tensors,

$$\varepsilon_{ij} = \frac{1+\nu}{E}\sigma_{ij} - \frac{\nu}{E}\sigma kk + \alpha_T \Delta T_P \delta_{ij} \tag{B.4}$$

where $\varepsilon_{ij}, i, j = r, \theta, z$ is the strain tensor tensor for a material with ν and E as the Poisson ratio and elasticity module and ΔT_P represents the temperature variation at each point, relative to a reference temperature. The inverse of Eqn. (B.4) in the matrix form is written as,

$$\begin{Bmatrix} \sigma_{rr} \\ \sigma_{\theta\theta} \\ \sigma_{zz} \\ \tau_{r\theta} \\ \tau_{rz} \\ \tau_{\theta z} \end{Bmatrix} = \frac{E}{(1+\nu)(1-2\nu)} \begin{bmatrix} 1-\nu & \nu & \nu & 0 & 0 & 0 \\ \nu & 1-\nu & \nu & 0 & 0 & 0 \\ \nu & \nu & 1-\nu & 0 & 0 & 0 \\ 0 & 0 & 0 & \frac{1-2\nu}{2} & 0 & 0 \\ 0 & 0 & 0 & 0 & \frac{1-2\nu}{2} & 0 \\ 0 & 0 & 0 & 0 & 0 & \frac{1-2\nu}{2} \end{bmatrix} \begin{Bmatrix} \varepsilon_{rr} \\ \varepsilon_{\theta\theta} \\ \varepsilon_{zz} \\ 2\varepsilon_{r\theta} \\ 2\varepsilon_{rz} \\ 2\varepsilon_{\theta z} \end{Bmatrix} + \frac{E\alpha_T \Delta T_P}{1-2\nu} \begin{Bmatrix} 1 \\ 1 \\ 1 \\ 0 \\ 0 \\ 0 \end{Bmatrix} \tag{B.5}$$

Finally, the total displacements of a point is interpreted through a strain-displacement

equation

$$\begin{Bmatrix} \varepsilon_{rr} \\ \varepsilon_{\theta\theta} \\ \varepsilon_{zz} \\ 2\varepsilon_{r\theta} \\ 2\varepsilon_{rz} \\ 2\varepsilon_{\theta z} \end{Bmatrix} = \begin{bmatrix} \frac{\partial}{\partial r} & 0 & 0 \\ \frac{1}{r} & \frac{\partial}{r\partial\theta} & 0 \\ 0 & 0 & \frac{\partial}{\partial z} \\ \frac{\partial}{r\partial\theta} & \left(\frac{\partial}{\partial r} - \frac{1}{r}\right) & 0 \\ \frac{\partial}{\partial z} & 0 & \frac{\partial}{\partial r} \\ 0 & \frac{\partial}{\partial z} & \frac{\partial}{r\partial\theta} \end{bmatrix} \begin{Bmatrix} u_{rr} \\ u_{\theta\theta} \\ u_{zz} \end{Bmatrix} \tag{B.6}$$

or

$$\varepsilon = \mathbf{D}_u \mathbf{u} \tag{B.7}$$

The principal of virtual works combines the elasticity equations (Eqns. B.2-B.7) along with the boundary conditions to be solved through a FE model. The displacement form of virtual work is, [19]

$$\iiint_V \delta\mathbf{u}^T \left[\mathbf{D}_u^T \, \mathbf{E} \, \mathbf{D}_u \mathbf{u} - \mathbf{D}_u^T \, \mathbf{E} \, \Delta T_P \alpha_T - \mathbf{F}\right] dV - \iint_S \delta\mathbf{u}^T P \, dS = 0 \tag{B.8}$$

where P is the hydrodynamic pressure field acting on the pad top surface.

B.2 Hexahedral (Brick) Element Equations

Figure 47 depicts a Brick (Hexahedral) elements in (a) the global cylindrical coordinate (r, θ, z) and the local neutral curvilinear coordinate system (s, q, t). A Brick element has is has six side with eight nodes and three DOFs at each node. with eight node and three degrees of freedom per each node.

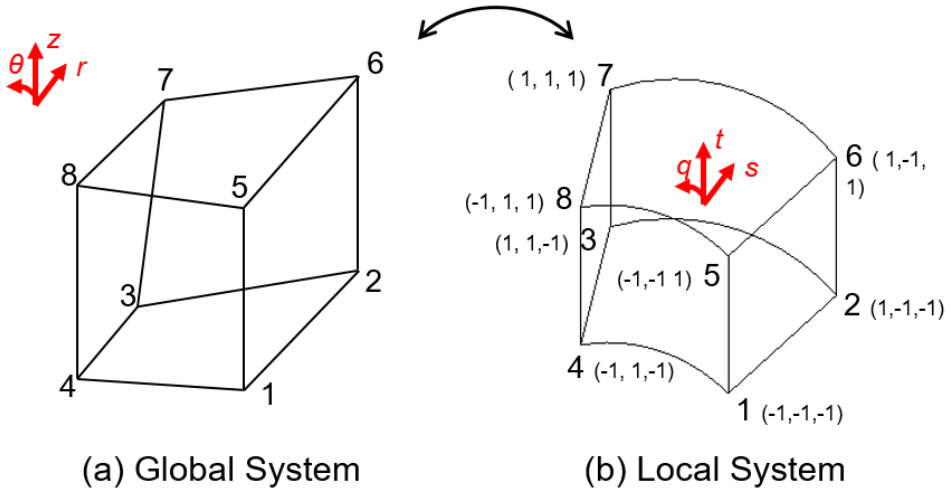

Fig. 47: A Brick element in (a) the global and (b) the local cylindrical coordinate systems with eight nodes and three DOFs per node.

Hence, assuming elastic deformations to vary linearly inside an element, a local deformation vector is,

$$\begin{Bmatrix} u_{rr}(s,q,t) \\ u_{\theta\theta}(s,q,t) \\ u_{zz}(s,q,t) \end{Bmatrix} = \begin{bmatrix} N_1 & 0 & 0 & N_2 & 0 & 0 & \dots & N_8 & 0 & 0 \\ 0 & N_1 & 0 & 0 & N_2 & 0 & \dots & 0 & N_8 & 0 \\ 0 & 0 & N_1 & 0 & 0 & N_2 & \dots & 0 & 0 & N_8 \end{bmatrix} \begin{Bmatrix} u^1_{rr} \\ u^1_{\theta\theta} \\ u^1_{zz} \\ \vdots \\ u^8_{rr} \\ u^8_{\theta\theta} \\ u^8_{zz} \end{Bmatrix} \tag{B.9}$$

or

$$\mathbf{u} = \mathbf{N}\mathbf{u}_N \tag{B.10}$$

where $(u^i_{rr}, u^i_{\theta\theta}, u^i_{zz})$ is the deformations of node$^{\textcircled{i}}$ and N_i are the shape functions, i.e.,

$$N_i(s,q,t) = \frac{1}{8}(1+s_i s)(1+q_i q)(1+t_i t), i = 1,\ldots,8 \tag{B.11}$$

and (s_i, q_i, t_i) is node$^{\textcircled{i}}$ location in the local coordinate. The same linear interpolation is used for transition between the global coordinate system (r, θ, z) and the local cylindrical system (s, q, t),

$$\begin{Bmatrix} r(s,q,t) \\ \theta(s,q,t) \\ z(s,q,t) \end{Bmatrix} = \begin{bmatrix} N_1 & 0 & 0 & N_2 & 0 & 0 & \ldots & N_8 & 0 & 0 \\ 0 & N_1 & 0 & 0 & N_2 & 0 & \ldots & 0 & N_8 & 0 \\ 0 & 0 & N_1 & 0 & 0 & N_2 & \ldots & 0 & 0 & N_8 \end{bmatrix} \begin{Bmatrix} r^1 \\ \theta^1 \\ z^1 \\ \vdots \\ r^8 \\ \theta^8 \\ z^8 \end{Bmatrix} \tag{B.12}$$

The FE solution requires to calculate the derivations of shape functions (N_i) with respect to global coordinate system variables. The rule of chain states that,

$$\frac{\partial N_i}{\partial s} = \frac{\partial N_i}{\partial r}\frac{\partial r}{\partial s} + \frac{\partial N_i}{\partial \theta}\frac{\partial \theta}{\partial s} + \frac{\partial N_i}{\partial z}\frac{\partial z}{\partial s} \tag{B.13a}$$

$$\frac{\partial N_i}{\partial q} = \frac{\partial N_i}{\partial r}\frac{\partial r}{\partial q} + \frac{\partial N_i}{\partial \theta}\frac{\partial \theta}{\partial q} + \frac{\partial N_i}{\partial z}\frac{\partial z}{\partial q} \tag{B.13b}$$

$$\frac{\partial N_i}{\partial t} = \frac{\partial N_i}{\partial r}\frac{\partial r}{\partial t} + \frac{\partial N_i}{\partial \theta}\frac{\partial \theta}{\partial t} + \frac{\partial N_i}{\partial z}\frac{\partial z}{\partial t} \tag{B.13c}$$

and in matrix form is,

$$\begin{Bmatrix} \frac{\partial N_i}{\partial s} \\ \frac{\partial N_i}{\partial q} \\ \frac{\partial N_i}{\partial t} \end{Bmatrix} = \begin{bmatrix} \frac{\partial r}{\partial s} & \frac{\partial \theta}{\partial s} & \frac{\partial z}{\partial s} \\ \frac{\partial r}{\partial q} & \frac{\partial \theta}{\partial q} & \frac{\partial z}{\partial q} \\ \frac{\partial r}{\partial t} & \frac{\partial \theta}{\partial t} & \frac{\partial z}{\partial t} \end{bmatrix} \begin{Bmatrix} \frac{\partial N_i}{\partial r} \\ \frac{\partial N_i}{\partial \theta} \\ \frac{\partial N_i}{\partial z} \end{Bmatrix} = \mathbf{J} \begin{Bmatrix} \frac{\partial N_i}{\partial r} \\ \frac{\partial N_i}{\partial \theta} \\ \frac{\partial N_i}{\partial z} \end{Bmatrix} \tag{B.14}$$

where **J** is the Jacobin matrix and is calculated based on Eqn.(B.12) as,

$$\mathbf{J} = \begin{bmatrix} \sum_{i=1}^{8} \frac{\partial N_i}{\partial s} r_i & \sum_{i=1}^{8} \frac{\partial N_i}{\partial s} \theta_i & \sum_{i=1}^{8} \frac{\partial N_i}{\partial s} z_i \\ \sum_{i=1}^{8} \frac{\partial N_i}{\partial q} r_i & \sum_{i=1}^{8} \frac{\partial N_i}{\partial q} \theta_i & \sum_{i=1}^{8} \frac{\partial N_i}{\partial q} z_i \\ \sum_{i=1}^{8} \frac{\partial N_i}{\partial t} r_i & \sum_{i=1}^{8} \frac{\partial N_i}{\partial t} \theta_i & \sum_{i=1}^{8} \frac{\partial N_i}{\partial t} z_i \end{bmatrix} \tag{B.15}$$

Then, the inverse of the Jacobin helps to obtain the derivations of the shape functions,

$$\begin{Bmatrix} \frac{\partial N_i}{\partial r} \\ \frac{\partial N_i}{\partial \theta} \\ \frac{\partial N_i}{\partial z} \end{Bmatrix} = \mathbf{J}^{-1} \begin{Bmatrix} \frac{\partial N_i}{\partial s} \\ \frac{\partial N_i}{\partial q} \\ \frac{\partial N_i}{\partial t} \end{Bmatrix} \tag{B.16}$$

B.3 Element Stiffness Matrix and Load Vector

Using the shape functions associated with Brick Elements, the virtual displacement is derived based on Eqn. (B.10) as,

$$\delta \mathbf{u} = \mathbf{N} \delta \mathbf{v} \tag{B.17}$$

where δv is the vector of nodal virtual displacements. Hence, substituting Eqn. (B.17) into the displacement form of the principle of virtual works (Eqn. (**??**)) gives,

$$\iiint_V \delta \mathbf{v}^T \left[\mathbf{N}^T \mathbf{D}_u^T \, \mathbf{E} \, \mathbf{D}_u \mathbf{N} \mathbf{v} - \mathbf{N}^T \mathbf{D}_u^T \, \mathbf{E} \, \Delta T_P \boldsymbol{\alpha}_T - \mathbf{N}^T \mathbf{F} \right] dV - \iint_S \delta \mathbf{v}^T \mathbf{N}^T P \, dS = 0 \tag{B.18}$$

where,

$$\Delta T_P = \sum_{i=1}^{8} N_i \Delta T_{P_i} \tag{B.19}$$

and,

$$\boldsymbol{\alpha}_T = \alpha \begin{Bmatrix} 1 \\ 1 \\ 1 \\ 0 \\ 0 \\ 0 \end{Bmatrix} \tag{B.20}$$

Therefore, the stiffness matrix is,

$$K_e^j = \iiint_V \delta \mathbf{v}^T \left[\mathbf{N}^T \mathbf{D}_u^T \, \mathbf{E} \, \mathbf{D}_u \mathbf{N} \right] dV, j = 1, \ldots, N_E : number of elements. \tag{B.21}$$

and load vector is

$$\mathbf{f}_j = \iiint_V \mathbf{N}^T \mathbf{D}_u^T \, \mathbf{E} \, \Delta T_P \boldsymbol{\alpha}_T dV + \iiint_V \mathbf{N}^T \mathbf{F} \, dV + \iint_S \mathbf{N}^T \mathbf{P} \, dS \tag{B.22}$$

Thus, the local stiffness matrices and load vectors are stored in a global stiffness matrix $\mathbf{K}^{\mathrm{G}}$ and a global load vector $\mathbf{F}^{\mathrm{G}}$, respectively. After enforcing proper boundary condition for the pivot-pad surface traction, a Cholesky decomposition technique is used to solve for the global displacement vector $\mathbf{u}^{\mathrm{G}}$.